NOTICE

The quality of this microform is heavily dependent upon the quality of the original thesis submitted for microfilming. Every effort has been made to ensure the highest quality of reproduction possible.

If pages are missing, contact the university which granted the degree.

Some pages may have indistinct print especially if the original pages were typed with a poor typewriter ribbon or if the university sent us an inferior photocopy.

Reproduction in full or in part of this microform is governed by the Canadian Copyright Act, R.S.C. 1970, c. C-30, and subsequent amendments.

AVIS

La qualité de cette microforme dépend grandement de la qualité de la thèse soumise au microfilmage. Nous avons tout fait pour assurer une qualité supérieure de reproduction.

S'il manque des pages, veuillez communiquer avec l'université qui a conféré le grade.

La qualité d'impression de certaines pages peut laisser à désirer, surtout si les pages originales ont été dactylographiées à l'aide d'un ruban usé ou si l'université nous a fait parvenir une photocopie de qualité inférieure.

La reproduction, même partielle, de cette microforme est soumise à la Loi canadienne sur le droit d'auteur, SRC 1970, c. C-30, et ses amendements subséquents.

Canada

Sensitivity of Flexible Manipulators to Payload Mass: A Parametric Study

Glen Bilodeau

A Thesis

in

The Department

of

Mechanical Engineering

Presented in Partial Fulfillment of the Requirements
for the Degree of
Master of Applied Science at
Concordia University
Montreal, Québec, Canada

September 1994

ISBN 0-315-97654-3

ABSTRACT

Sensitivity of Flexible Manipulators to Payload Mass: A Parametric Study

Glen Bilodeau

The effects of a payload on a flexible manipulator are studied and results of the study are presented in this thesis. The manipulators are inherently non-rigid mechanisms with multiple degrees of freedom and effects of flexibility of their components have been the researchers' ongoing interest. This work investigates the effects of typical payloads on kinematics and dynamics of a manipulator. For simplicity, a two-link planar manipulator is selected but work can be extended to an n-link planar manipulator. The objective of the study is primarily to estimate the significance of the payload effects and test sensitivity of the mathematical model to the changes in the payload. The purpose is to provide better information to the design and controls engineers in their tasks to achieve safe and precise manipulator operation.

A model of a two-link manipulator with actuators provided at joints for each link is formulated. The model is based on the finite element formulation. The assumptions include: distributed mass, small deflections and so called Timoshenko's beam model for links which takes into account the rotary inertia and the shear. A further assumption is that the end point of the flexible link will follow the same path as the end point of the respective rigid link. By applying the inverse kinematics the resulting deflections with respect to rigid link are determined. The driving torques are determined such that the links follow the required trajectory. The numerical time integration is carried out using a scheme similar to Newmark's algorithm. The boundary conditions imposed are clamped-end on the driven side and free-end, for both links.

The model provides the dynamics of the manipulator's links due to two typical payloads. The links' material and cross-section sizes are selected for convenience. The results are obtained for all quantities necessary for design and control purposes: driving torques, transverse and axial deflections, shear and axial forces and presented graphically for both the rigid links and flexible links. The comparison of the results for the two cases is carried out. Verification of the model is done and results found justifiable.

ACKNOWLEDGEMENTS

The author is grateful to the National Sciences and Engineering Research Council for their financial support through their Postgraduate Scholarship at the Master's level (PGS A).

Special thanks go to Dr. V. Latinovic for his invaluable contribution and time under very special circumstances. The author thanks Dr. T.S. Sankar for opening some opportunities over the course of this project and Dr. R. Ganesan for some constructive discussions. The author thanks his colleagues of B-204 especially Mr. M. El-Karmalawy and Mr. S. Zhang for their discussions, support and encouragement through some challenging times. Thanks to Mr. F. Chan for his encouragement.

L'auteur remercie sa compagne, Mme. M-C. Duguay, pour son incessable support, encouragement et compréhension.

Finally, and most importantly, the author is grateful to his parents for all aspects of their support throughout the author's life. This thesis is dedicated to them.

TABLE OF CONTENTS

LIST OF TABLES AND FIGURES

TABLE:

FIGURE:

NOMENCLATURE

Latin Symbols

a	Acceleration (subscript G indicates centroid of element)
A	Cross sectional area of link
b,h	Cross sectional dimensions of links (rectangular)
$[C]$	Damping matrix
E	Young's modulus
E_{est}	Error estimate
f	Force per unit length
F	Force vector
G	Shear modulus
I	Area moment of inertia of link
I_G	Mass moment of inertia about G (centroid of element)
$[K]$	Stiffness matrix
k	Shear coefficient
L_n	Length of nth link
$[M]$	Mass matrix
M_z	Moment
m	Mass
m_p	Mass of payload
$N(x)$	Shape function
$[N]$	Matrix of shape functions
P_V	Shear force due to axial force
P	Axial force due to payload
P_x	Total axial force

$\{q\}$	Vector of nodal displacements
R	Rotation matrix
R_{xn}, R_{yn}	Reactions in x and y directions of nth endpoint of link
r	Radial position
r_p	Arm of payload
T	Vector of reactions
u_x	x-deformation variable
u_y	y-deformation variable
$\{u\}$	Vector of deflections within a finite element
V_y	Shear force
v	Velocity

Greek Symbols

α	Angular acceleration
ω	Angular velocity (subscript b indicates of base)
ρ	Density of material
τ_n	Torque at nth endpoint of link
θ_n	Relative joint rotation of nth link
$\dot{\theta}_n$	Relative angular joint velocity of nth link
$\ddot{\theta}_n$	Relative angular joint acceleration of nth link
θ_z	Rotational deformation variable
Θ_1, Θ_2	"Newmark-like" parameters

Chapter 1

INTRODUCTION

Every structure has an inherent flexibility including robotic manipulators. They should be regarded as deformable bodies [1]. This is especially true of industrial robots with lightweight and flexible links. Special purpose robots such as medical and manufacturing robots (typical tasks include surgery, welding and materials handling) require high precision, repeatability and accuracy [2] [3]. Furthermore, manipulators in space must be light to conform to launch requirements and must be capable of manipulating a large load mass [4].

Robot arms have been considered as having rigid links in many studies, but there are drawbacks to this assumption. For example, if one models the manufacturing robot as rigid links they must be designed and constructed as undeformable as possible, which means heavy arms and large motors. By allowing the links to elastically deform, that is, by reducing the requirement for rigidity, one is able to increase working speeds, reduce energy consumption, and increase the payload of the manipulator. Deformations are estimated and then compensated for by designing a suitable control scheme. Therefore, in modelling, simulation and design, structural flexibility of robot links should be included into the study [1] [5].

In this thesis, emphasis is placed on the effect of payload on a manipulator

assuming that the links of the robot are inherently elastic (non-rigid). One may know the maximum payload the manipulator is able to safely carry but one may not know how this payload affects the manipulator in terms of driving torques, deformations and internal forces. Another aspect of the payload that is important is the modelling of the mass at the end effector or gripper. Also, in the presence of gravity, as a payload is lifted, the links will be loaded axially. As a consequence, it is proposed to model the links as beam-columns rather than simply as beams. Hence, determining the effects of a payload on dynamics would give a better idea of modelling a manipulator with payload taken into account.

The structure of the thesis is as follows: in chapter 2, some previous studies are reviewed and the scope of this thesis is outlined. The model of a two-link manipulator, through finite elements, is formulated in Chapter 3. The contribution of payload mass to the model is stated. Throughout Chapter 4, the results (driving torques, deformations and internal forces) are presented graphically and discussed. In Chapter 5, conclusions are drawn and some recommendations for future work are given.

Chapter 2

LITERATURE SURVEY

In order to formulate the scope of the present work, a review of the previous studies will illustrate the evolution of the research on flexible manipulators. At the same time, the objectives of the present work are presented.

2.1. Previous studies

Much of the early work dedicated to flexibility in links involved the study of mechanisms defined as a combination of rigid or resistant bodies formed and connected such that they move relative to each other [6]. Some of these early works include Benedict and Tesar [7], Dubowsky and Gardner [8], Book [9], and Huston [10]. Essentially, the same methods apply to robots since robots are a subset of mechanisms. A robot is defined as an automatic, reprogrammable, multifunctional manipulator designed to handle material, tools, or specialized devices through variable programmed motions for the performance of a variety of tasks [3].

Methods to obtain the equations of motion and methods for analysis of

flexible manipulators are varied. Kelly and Huston [11] model the flexibility effects in robot arms using d'Alembert-Lagrange principle. Book [12] uses a Lagrangian formulation of the dynamics reduced to a form similar to that of the rigid-link case. Others like Sunada and Dubowsky [13] represent the elastic links as discrete systems possessing finite elastic degrees of freedom and using a finite element method, analyze the behaviour of robot manipulators with complex-shape flexible links. Other papers dealing with finite element method applied to analyzing robot structures include Usoro et al [14], Naganathan and Soni [15], Bayo [16], Bayo et al [17] [18], Bricout et al [19], Kalra and Sharan [20], Beres et al [21]. Usoro et al [14] and Bricout et al [19] use Lagrange equations to formulate their model. Simulations are done, yet the model neglects effects like shear and rotary inertia. Kalra and Sharan [20] developed software to automatically generate the dynamic equations for a flexible manipulator. Some advantages of the finite element method include easy adaptability to changing boundary conditions, to different mass properties and to varying tip loads [16]. The finite element method provides a straightforward formulation of the manipulator equations of motion. As such, the finite element method is used in this thesis to model the system.

Furthermore, studies dealing with control issues of flexible manipulators require a model of the system. Cetinkunt and Book [22], Siciliano and Book [23], and Hastings and Book [24] use a Lagrangian-assumed mode approach to develop

the model of their manipulator. Hamilton's principle provides the basis for the formulation of the flexible manipulator in Cannon and Schmitz [25] and Matsuno et al [26] studies. In the case of Cannon and Schmitz [25], experimental work was carried out on the control of a one-link device which was constrained to deflect in a plane. Sakawa et al [27] use, essentially, Newton's Second Law to derive manipulator dynamic equations. As it can be seen, several methods are available to determine the governing equations of the systems.

In the above studies, the effect of payload mass is not extensively investigated, but in some papers it is nevertheless modelled as a point mass or a rigid body with a concentrated mass as its centre of gravity. Several questions have been posed in a report by Whitney et al [28] concerning the design and control of industrial and space manipulators. Among other issues, consideration of payload mass is essential in the design and control processes. Continuing, the payload and the distance the weights are moved constitute the major variables to be considered. Furthermore, a criterion by which the performance of a manipulator is judged is the payload-speed relation. It is indicated that as a robot arm handles a mass, the torques applied at the joints must overcome the inertia forces as well as the weight of the links, hence, speed is limited. This report suggests that a payload would have a very complex effect on multi-degree of freedom manipulators. As a consequence, research of payload effects on manipulators is an imperative.

Parks and Pak [4] investigate the effect of payload on a single-link manipulator. Their model is based on the Euler-Bernoulli beam theory in which rotary motion, longitudinal motion, shear strain, and structural damping are neglected. Conclusions state that payload mass has a profound effect on the manipulator dynamics and that there are changes in the fundamental frequency and in the mode shapes. Furthermore, sensitivity to payload inertia is much greater than to payload mass. Experimental work on a horizontal, planar, one-link manipulator was done, yet the link was constrained to satisfy the Euler-Bernoulli beam theory assumptions.

Jen and Johnson [29] used the CMS (Component Mode Synthesis) method to study the effects of varying configuration, payload and several physical parameters on the natural frequencies of the manipulator. Their model neglects the effect of shear on the links. It was found that increased payload mass yields lower natural frequencies. Furthermore, the rate of decrease is larger for lower frequencies than for higher frequencies since the vibrations of the payload at lower modes are stronger than at higher modes. In general, it can be seen that the manipulator is very sensitive to payload.

With the addition of a payload at the manipulator end point, the manipulator's vibratory motions are affected. Wang and Wei [30] study the vibrations of the end point of a manipulator with a moving slender prismatic beam. They concluded that the contracting and extending global motions have both

stabilizing and destabilizing effects on the manipulator.

2.2. Scope of Thesis

A parametric study is carried out to determine the influence of payload on a manipulator with link flexibility. The objective of this work is primarily to estimate the significance of the payload effects and test the sensitivity of the mathematical model to the changes in the payload. This is accomplished through the investigation of a two-link planar manipulator, although the work may be applied to an n-link planar robot arm. Payloads, as part of robot arms, have recieved some attention, but the model of the manipulator should be able to account for shear forces and axial compression. Since the manipulator in this study is in the vertical plane, gravitational force contributes to an axial force along the manipulator links. A finite element model of the arm [15] is used to which a model of the payload is incorporated. Timoshenko theory is used to model the links to include the effects of rotary inertia and of shear. To improve the model, the links are treated as beam-columns rather than simple beams as in previous studies which did not include such a formulation. As such, the contribution of own-weight (linearly varying) and payload weight are taken into account. Also, the model incorporates two payload orientations in the dynamics of the manipulator's links.

Chapter 3

FORMULATION OF THE MODEL

In this chapter, the formulation of the model of a flexible manipulator with payload is given. The methodology and the time function solutions are presented.

3.1 Description of Problem

The objective of this section is to model the dynamics of a two-link flexible (non-rigid) manipulator with the effect of payload. Finite element formulation is used to describe the links' dynamic model. Timoshenko beam theory, which takes into account the rotary inertia and shear deformation, is the underlying theory in the modelling of the links. This beam theory offers an improved model since most manipulators may be modeled much simpler with the assumption of non-slender links. The Bernoulli-Euler theory assumes slender links. When the ratio of thickness to length of the link is increased the Bernoulli-Euler model becomes less accurate [32]. In the present model, the links are assumed to be deformable axially, transversely, and angularly. The three directions of deformation will be described by independent shape functions.

In order to simplify the procedure, some assumptions are made. First, the total motion of the links includes the rigid body motion and the superposed elastic motion due to deformations. The end points of each link of the flexible arms will follow the same path as the end points of the respective rigid link manipulator. As such, the kinematics of the end point of each link is known since they are constrained to follow the same trajectory as the corresponding rigid link (inverse kinematics is readily obtained from the rigid body motion). Next, the links have a distributed mass and structural damping is ignored. Joint friction and actuator inertia are neglected in this study. In addition, these joints are assumed to be rigid. Finally, for simplicity, a two-link manipulator is studied but the formulation may be extended to an *n*-link robot arm. Also, only planar motion is studied.

3.2 Method of Solution

The solution involves a systematic procedure beginning with the determination of the kinematics of the flexible manipulator and ending with the time solution for deformations and torques. Once the model of the manipulator is established, the payload model is added. The step by step procedure follows:

- Determination of kinematics of a typical element on a link.
- Dynamic equilibrium of an element to determine governing equations.
- Application of principle of virtual work.
- Assuming shape functions for finite element formulation of one link.

- Determining element equations of motion, assembly of element matrices.
- Imposing boundary conditions.
- Inclusion of payload model and axial force effects
- Solution for deformations and torques.

3.3. Kinematics of Manipulator

Figure 3.1 illustrates a two-link manipulator. The manipulator's links have respectively lengths L_1 and L_2, mass density ρ, cross sectional dimensions b and h giving an area $A=bh$ and area moment of inertia $I = bh^3/12$. Other cross sectional shapes can be introduced by calculating the area and moment of inertia for that cross section. Material strength properties include Young's modulus E and shear modulus G. Furthermore, Timoshenko beam theory requires a shear coefficient which depends on the cross section of the beam and is given by k [33]. This shear coefficient allows for the approximation of the stress distribution over the cross section. Furthermore, the value of k is dependent on Poisson's ratio or on the cross sectional dimensions of the link. For a solid rectangular cross section, it can be taken as $k=5/6$ [34] [35].

The torques are applied at the base joint of the first link and at the base joint of the second link. Consequently, the links undergo rotations of θ_1 and θ_2 with respect to the preceding link (Figure 3.1). If this manipulator is rigid, then the kinematics of every point on the rigid links is known through a simple kinematic analysis. Recall that the motion of a flexible manipulator may be

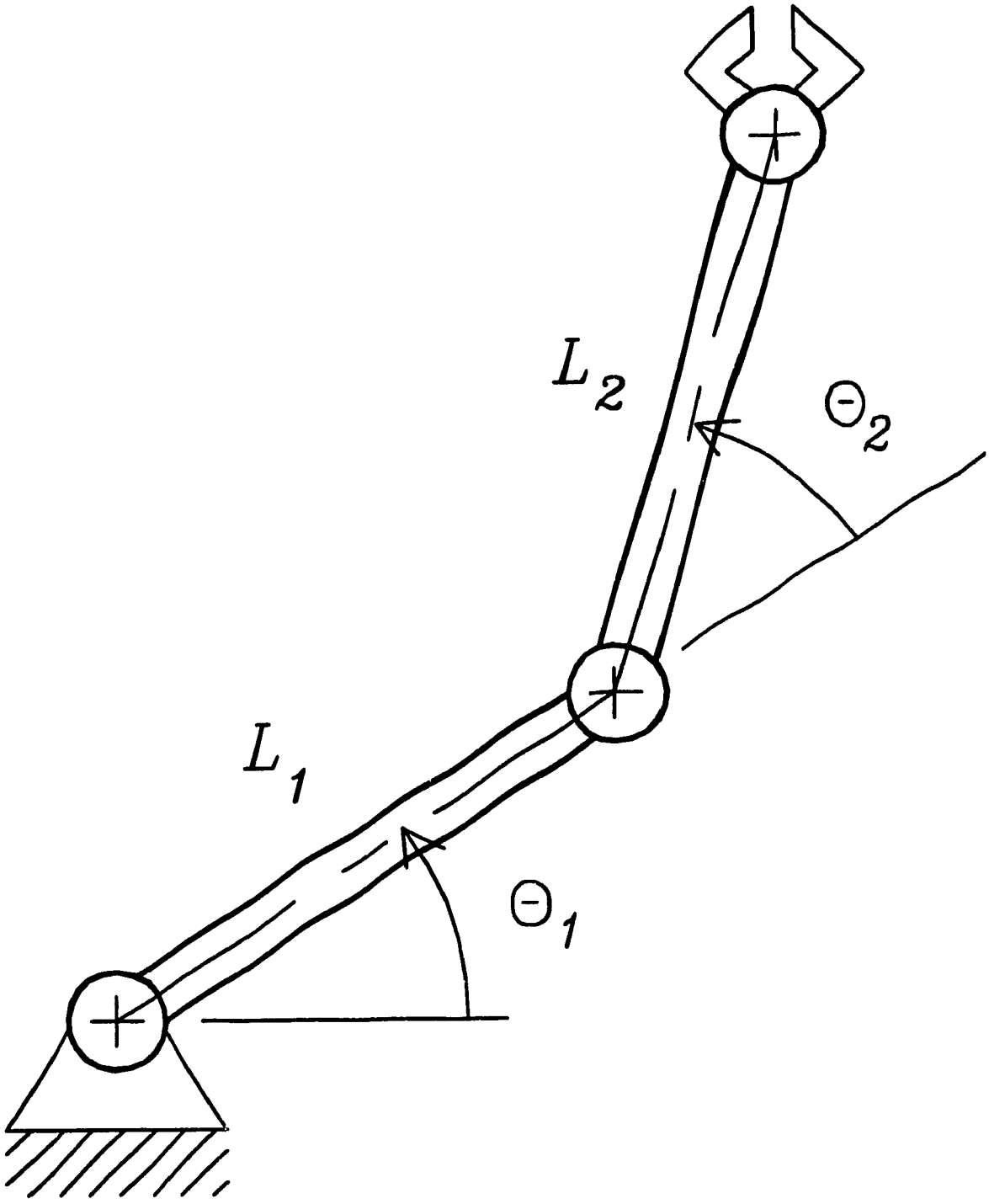

Figure 3.1. Two-link manipulator.

described by a rigid body motion and an elastic displacement due to deflections. The rigid body motion consists of angular displacements, velocities and accelerations of the links, that is, θ_1, θ_2, $\dot{\theta}_1$, $\dot{\theta}_2$, $\ddot{\theta}_1$, $\ddot{\theta}_2$, for a two link planar manipulator. By inverse kinematics, the Cartesian positions, velocities and accelerations may be found for any point on the manipulator. The points of interest are the end points since the flexible manipulator will be required to follow the same trajectory as that of the rigid manipulator.

The procedure of Naganathan and Soni [15] is followed. By combining the rigid body and elastic kinematics, it is possible to determine the kinematics of a flexible manipulator. Figure 3.2 describes a typical element on a link. The objective is to determine the acceleration of the centroid of the element, point *G*. From rigid body kinematics one obtains the acceleration vector

$$a_G = a_b + \omega_b \times (\omega_b \times r) + \alpha_b \times r + 2\omega_b \times v_{rel} + a_{rel} \tag{3.1}$$

where

$$\begin{aligned} r &= (x+u_x)\hat{i}_b + u_y \hat{j}_b \\ v_{rel} &= \dot{u}_x \hat{i}_b + \dot{u}_y \hat{j}_b \\ a_{rel} &= \ddot{u}_x \hat{i}_b + \ddot{u}_y \hat{j}_b \\ a_b &= a_{bx} \hat{i}_b + a_{by} \hat{j}_b \end{aligned} \tag{3.2}$$

Here vectors r, v_{rel}, and a_{rel} represent the kinematics of the deformation, and are relative to the rigid link motion. The angular accelerations and angular velocities of the base (subscript b) are equal to the sum of the joint accelerations and joint

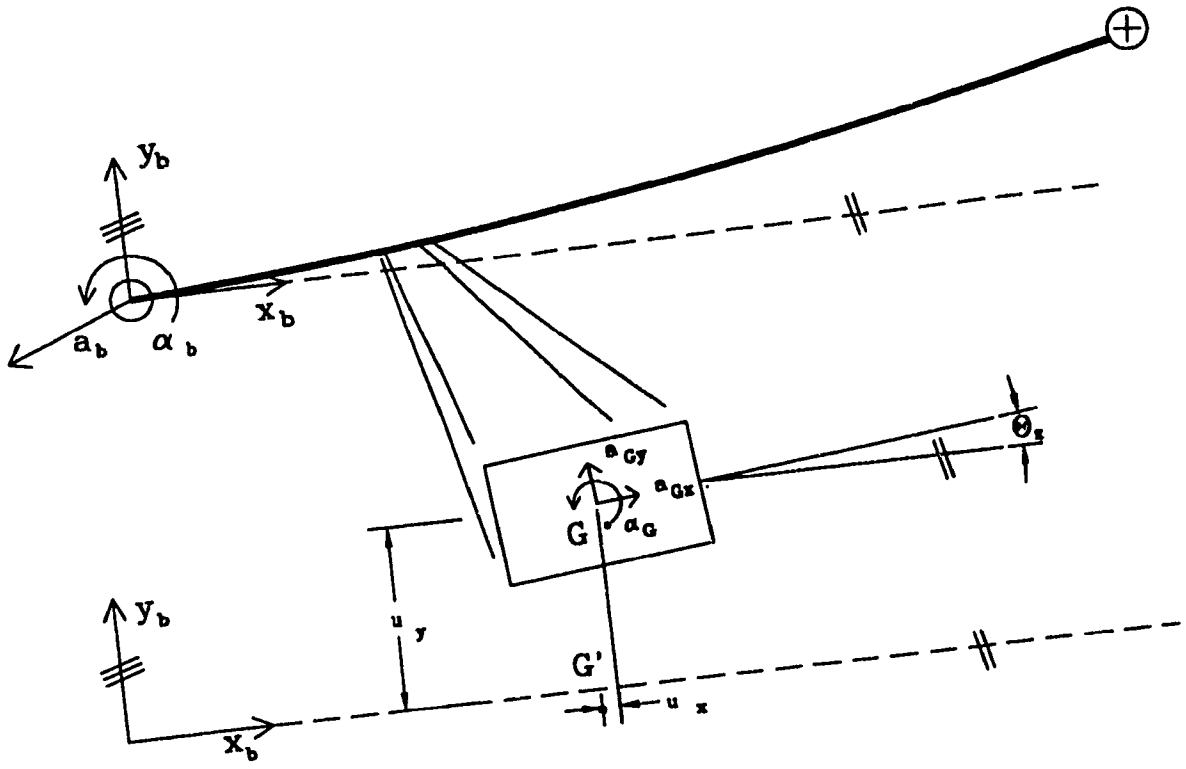

Figure 3.2. Typical element on a link.

velocities of all the joints of preceding links and including the link under study. For example, for the second link,

$$\begin{aligned} \omega_b &= \dot{\theta}_1 + \dot{\theta}_2 \\ \alpha_b &= \ddot{\theta}_1 + \ddot{\theta}_2 \end{aligned} \tag{3.3}$$

From equation (3.2) and Figure 3.2 it is evident that the relative positions, velocities and accelerations are composed of the elastic deflections and their respective rates relative to the rigid link. The base acceleration, a_b is determined from the rigid body motion, that is, the inverse kinematics of the manipulator as if the robot arm were rigid. The angular velocity and angular acceleration of the centroid of the element are given by,

$$\begin{aligned} \omega_G &= (\omega_b + \dot{\theta}_z)\hat{k}_b \\ \alpha_G &= (\alpha_b + \ddot{\theta}_z)\hat{k}_b \end{aligned} \tag{3.4}$$

Here, θ_z and its time derivatives represent the rotational deformations and the rates of deformation of the element. Now that all the kinematics of a typical element on a link are found, the dynamic equations may be determined.

3.4. Dynamic Equilibrium

Consider Figure 3.3, which shows the forces acting on an element within a link. A standard procedure is followed by drawing a free body diagram for the element as shown in Figure 3.3. Applying Newton's Second Law, the inertia forces

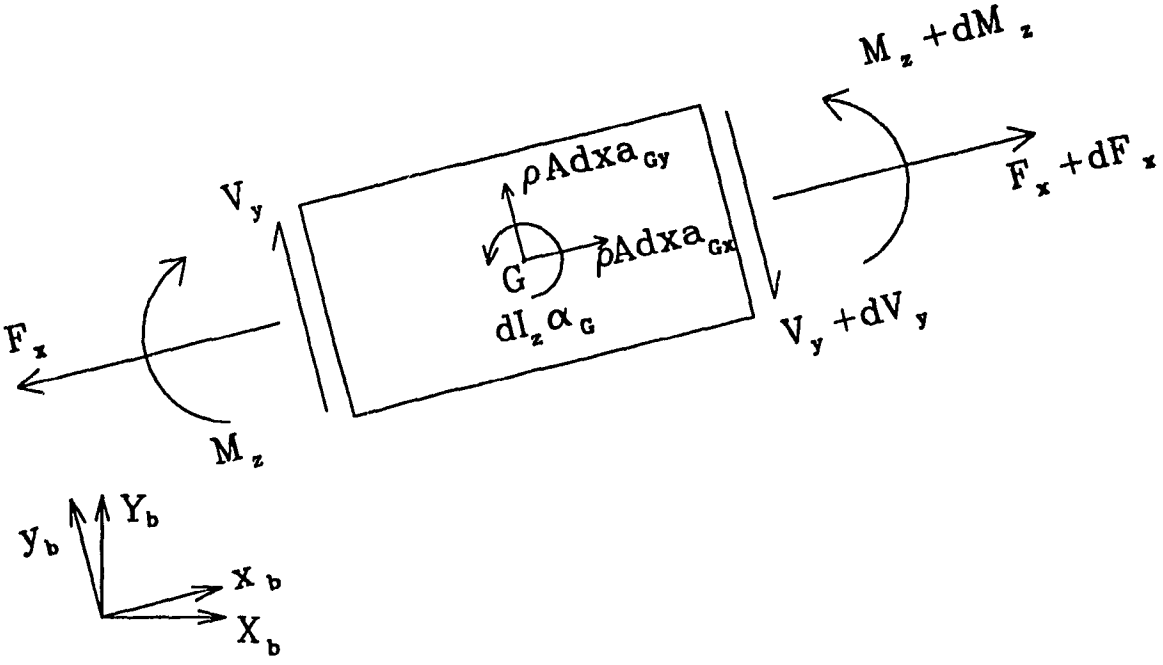

Figure 3.3. Element force diagram.

and moments are summed,

$$\begin{aligned} \Sigma F &= dma_G \\ \Sigma M_G &= dI_G \alpha_G \end{aligned} \tag{3.5}$$

For the time being, the effect of an axial force (due to payload and self-weight) is neglected; this will be included in Section 3.7. Several relations can be obtained from elastic theory and Timoshenko beam theory that relate the axial and shear stresses and bending moments to the deformations. By Timoshenko theory, the shear force can be expressed as,

$$V_y = k\,AG(\theta_z - \frac{\partial u_y}{\partial x}) \tag{3.6}$$

The term within the brackets represents the loss of slope, equal to the shear angle. θ_z describes the slope due to bending while the partial derivative denotes the slope of the center line of the beam [36]. Further, the bending moment is simply,

$$M_z = E\,I\frac{\partial \theta_z}{\partial x} \tag{3.7}$$

Finally, the forces in the axial direction due to deformation are considered,

$$F_x = A\,E\frac{\partial u_x}{\partial x} \tag{3.8}$$

By summing up the forces and moments in the x, y and θ_z directions, dynamic

equilibrium expressions per unit length are obtained,

$$\begin{aligned} A\,E\frac{\partial^2 u_x}{\partial x^2}+f_x&=\rho A a_{Gx} \\ -\frac{\partial V_y}{\partial x}+f_y&=\rho A a_{Gy} \\ \frac{\partial M_z}{\partial x}-V_y&=I_G\alpha_G \end{aligned} \tag{3.9}$$

If external forces (including gravitational forces) are present, they would be included in the terms (per unit length) f_x and f_y. The dynamic equilibrium has been established. The principle of virtual work on virtual displacements is applied to set up these equations into a form suitable for use in finite elements.

3.5. Finite Element Equations of Motion

The finite element equations of motion for a two-link flexible manipulator are derived from the principle of virtual work and applied to the kinematics and dynamics obtained earlier.

3.5.1. Principle of Virtual Work

Application of the principle of virtual work directly to the equations representing

dynamic equilibrium allows one to set up the equations of motion. This results in,

$$\int_{x_1}^{x_2}([\rho A a_{Gy}+\frac{\partial V_y}{\partial x}-f_y]\delta u_y+[\rho A a_{Gx}-AE\frac{\partial^2 u_x}{\partial x^2}-f_x]\delta u_x+[I_G\alpha_G-\frac{\partial M_z}{\partial x}+V_y]\delta\theta_z)dx=0 \qquad (3.10)$$

Here, x_1 and x_2 locate the finite element, along the length of the link, with respect to the link's base-attached frame. Knowing the elastic relations between the shear forces, bending moments and the transverse and rotational deformations given in the previous section, they are substituted into equation (3.10). Carrying out the differentiation and integration leads to

$$\int_{x_1}^{x_2}[\rho A a_{Gy}\delta u_y+\rho A a_{Gx}\delta u_x-f_y\delta u_y-f_x\delta u_x+I_G\alpha_G\delta\theta_z+V_y\delta(\theta_z-\frac{\partial u_y}{\partial x})+M_z\delta(\frac{\partial\theta_z}{\partial x})+AE\frac{\partial u_x}{\partial x}\delta(\frac{\partial u_x}{\partial x})]dx= \qquad (3.11)$$
$$[-\delta u_y V_y+\delta\theta_z M_z+AE\frac{\partial u_x}{\partial x}\delta u_x\ ]_{x_1}^{x_2}$$

This equation represents the work done by the inertial forces including rotary inertia, by the shear and axial forces, and by the bending moment within the interval $[x_1, x_2]$. In order to approximate the deflections, shape functions for the deformation must be chosen as a step in the finite element formulation. This is discussed in the next section.

3.5.2 Finite Element Formulation

In the finite element method, an assumption of the shape of the deflections within the element in terms of the nodal deflections is made. [37] For simplicity the

deflections are taken as linear within the element. Therefore, deflections within the element may be expressed as a product of linear shape functions and nodal displacements, in matrix form,

$$\{u\}_{ne}=[N]_e\{q\}_{ne} \tag{3.12}$$

where $\{u\}_{ne}$ is the vector of deflections at the centroid of the element, $\{q\}_{ne}$ is the vector of nodal displacements, and $[N]_e$ is the shape function; n in the subscript refers to the nth link. Expand equation (3.12) so that

$$\begin{bmatrix} u_x \\ u_y \\ \theta_z \end{bmatrix} = \begin{bmatrix} N_1(x) & 0 & 0 & N_2(x) & 0 & 0 \\ 0 & N_1(x) & 0 & 0 & N_2(x) & 0 \\ 0 & 0 & N_1(x) & 0 & 0 & N_2(x) \end{bmatrix} \begin{bmatrix} (U_x)_1 \\ (U_y)_1 \\ (\theta_z)_1 \\ (U_x)_2 \\ (U_y)_2 \\ (\theta_z)_2 \end{bmatrix} \tag{3.13}$$

where

$$N_1(x)=\frac{(x_2-x)}{(x_2-x_1)}\ ,\ N_2(x)=\frac{(x-x_1)}{(x_2-x_1)} \tag{3.14}$$

As one can see, this approximation has separated the space and time dependency of the displacements. Also, the generalized vector is the vector of nodal deflections,

$$\{q\}^T_{ne}=[(U_x)_1\ (U_y)_1\ (\theta_z)_1\ (U_x)_2\ (U_y)_2\ (\theta_z)_2]_n \tag{3.15}$$

If equation (3.15) and its variations are substituted into equation (3.11) and the

differentiation is carried out, the equations of motion for an element are obtained, [18]

$$[M]_{ne}\ddot{q}_{ne}+[C]_{ne}\dot{q}_{ne}+[K]_{ne}q_{ne}=F_{ne} \tag{3.16}$$

$[M]_{ne}$ = Element inertia matrix of the nth link.

$[C]_{ne}$ = Element damping matrix consisting of Coriolis terms [18]. Structural damping is ignored.

$[K]_{ne}$ = Element stiffness matrix of the nth link made up of structural stiffness $[K]_s$, and stiffness matrix due to relative tangential and normal accelerations of the element, $[K]_m$ [18].

F_{ne} = Element force vector of the nth link due to external forces, accelerations, etc [18].

Equation (3.16) represents the equation of motion in terms of the rotating reference frame which is attached to the rigid link.

By using independent shape functions for u_y and θ_z, a phenomenon known as shear lock occurs when the model is used to approximate slender beams. Here, too much emphasis is placed on the shear strain term in the Timoshenko expression for shear stress. With the model as it is now, when the beam has an increased slenderness, the model structural stiffness increases, just the opposite of what should happen in reality. In order to correct this problem, reduced integration (one point instead of the exact two point integration) is used on the shear strain term to obtain a better model which is valid for both slender beams and beams of large

depth [37]. Both the conventional and reduced order stiffness matrices are given in the Appendix I in addition to the contents of the mass and damping matrices.

It can be observed that the matrices are functions of time as justified by the dependence of the element stiffness and damping matrices on the global motion of the reference frame attached at the base of each link. In order to obtain a model of the whole system, the matrices must be assembled. Once assembled, two equations of motion will emerge; one for the first link and one for the second link. Of course, this would correspond to n equations for n links.

To be consistent, the matrices of each link must be expressed in a common reference frame. When one comes to numerically integrating the rates of change of the deflections to obtain the deflections, the vectors will be expressed in the same frame to ensure compatibility between displacement, velocity and acceleration for the degrees of freedom. The deformations and rates of deformations are then expressed in a common frame. All deformations of a link are measured with respect to the corresponding rigid link or the frame parallel to the rigid link (Figure 3.2). R_g designates the rotation matrix transforming the element vectors from the link attached frame $x_{nb}y_{nb}$ to a frame (also attached to the link) $X_{nb}Y_{nb}$, which is parallel to the fixed base frame. This is illustrated in Figure 3.4. It is understood, for the planar case, that the z-axis remains unchanged after the transformation.

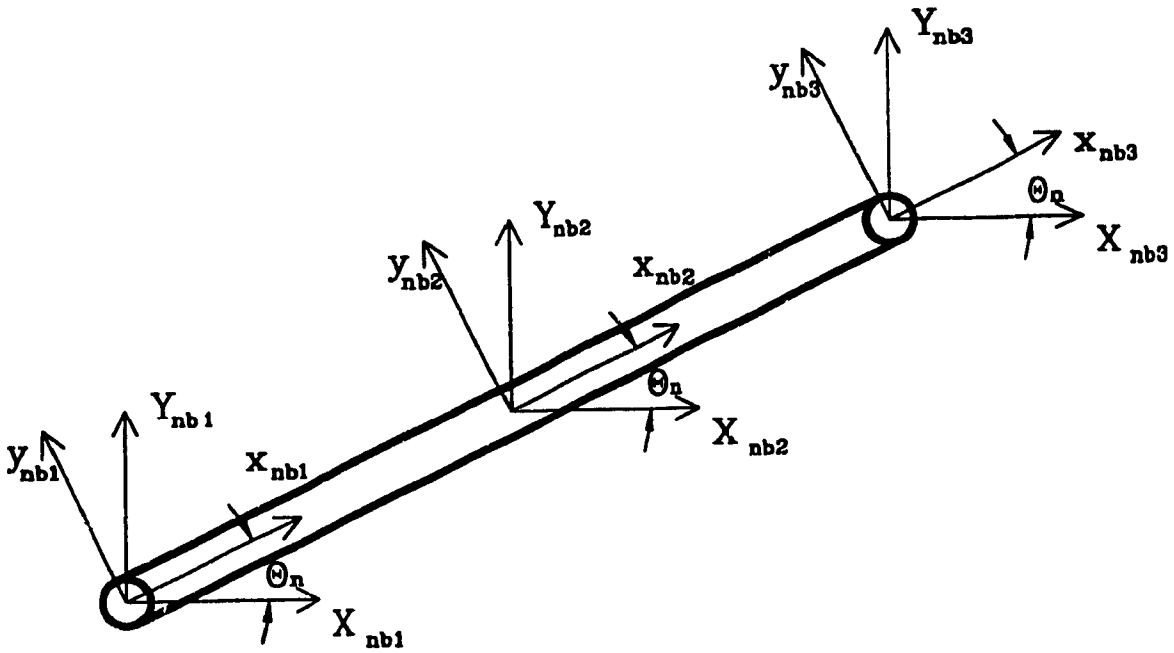

Figure 3.4. Local and global frames attached to link (for two elements).

The rotation matrices for each link (as indicated by the numerical subscript) can be written as,

$$R_{1g}=\begin{bmatrix}\cos\theta_1 & \sin\theta_1 & 0\\ -\sin\theta_1 & \cos\theta_1 & 0\\ 0 & 0 & 1\end{bmatrix}$$
$$R_{2g}=\begin{bmatrix}\cos(\theta_1+\theta_2) & \sin(\theta_1+\theta_2) & 0\\ -\sin(\theta_1+\theta_2) & \cos(\theta_1+\theta_2) & 0\\ 0 & 0 & 1\end{bmatrix} \tag{3.17}$$

In order to transform the element deformation vectors, the rotation matrices must be augmented to 6x6 matrices, which consist of diagonal matrices in terms of the rotation matrices given in equation (3.17). The element deformation vectors expressed in a common frame (parallel to the base frame) are given as,

$$\begin{aligned} q_{ne}&=R_{ng}^T q_{ng}\\ \dot{q}_{ne}&=\dot{R}_{ng}^T q_{ng}+R_{ng}^T \dot{q}_{ng}\\ \ddot{q}_{ne}&=\ddot{R}_{ng}^T q_{ng}+2\dot{R}_{ng}^T \dot{q}_{ng}+R_{ng}^T \ddot{q}_{ng}\end{aligned} \tag{3.18}$$

Upon substitution of equations (3.18) into equation (3.16), the equations of motion become

$$[M]_{ng}\ddot{q}_{ng}+[C]_{ng}\dot{q}_{ng}+[K]_{ng}q_{ng}=F_{ng} \tag{3.19}$$

where,

$$
\begin{aligned}
[M]_{ng} &= R_{ng}[M]_{ne}R_{ng}^{T} \\
[C]_{ng} &= R_{ng}(2[M]_{ne}\dot{R}_{ng}^{T}+[C]_{ne}R_{ng}^{T}) \\
[K]_{ng} &= R_{ng}([M]_{ne}\ddot{R}_{ng}^{T}+[C]_{ne}\dot{R}_{ng}^{T}+[K]_{ne}R_{ng}^{T}) \\
F_{ng} &= R_{ng}F_{ne}
\end{aligned}
\tag{3.20}
$$

The element matrices expressed in the common global frame can be assembled by the standard finite element technique. Note that the inertia matrix (for planar elements) is invariant after a rotation, therefore, some computation is saved [38]. The boundary conditions will be imposed by illustrating the two element case for the sake of simplicity. Figure 3.5 shows the type of boundary conditions that will be used. It is assumed that the link is clamped at one joint, that is, the angular deformation at this joint is zero. Recall that the deflections of a flexible link are measured with respect to the rigid link. In order that the manipulator follows the same trajectory as the corresponding rigid manipulator, it is assumed that the end points of the flexible links have the same kinematics as the corresponding rigid links [18]. For example, if the end point of the first link has an acceleration, a_1 for the rigid case, then it is assumed that the same end point will have acceleration a_1 for the flexible case. Also, since the motion of the links are taken as a superposition of a rigid body motion and elastic deflections, the imposed boundary conditions can be taken as cantilever beam with respect to the rigid link, the clamped end being the driven end of the link. For example, in terms

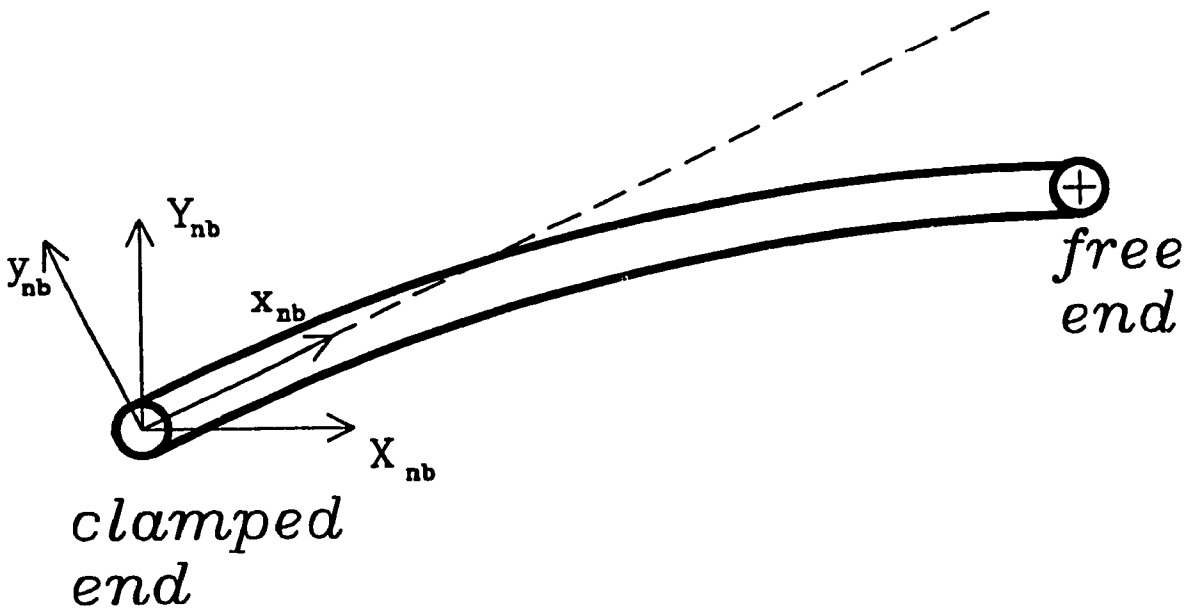

Figure 3.5. Boundary conditions with local and global attached frames.

of the coordinate frame $x_{nb}y_{nb}$ for a two-element link,

$$q_n=[0\ 0\ 0\ (U_x)_2\ (U_y)_2\ (\theta_z)_2\ (U_x)_3\ (U_y)_3\ (\theta_z)_3]_n^T \tag{3.21}$$

It follows that the time derivatives have the same boundary conditions. As stated previously, for the solution of the deflections over time, a one-step time integration procedure (outlined in Section 3.8) will be used [39]. Therefore, all deformation variables must be expressed in the same reference frame since vector addition between previous and present time values is required in the integration procedure. In this case, the boundary conditions in the reference frame $X_{nb}Y_{nb}$ become (for the cantilever beam, it is invariant, but the deformations are measured in a different reference frame),

$$q_n'=[0\ 0\ 0\ (U_x')_2\ (U_y')_2\ (\theta_z')_2\ (U_x')_3\ (U_y')_3\ (\theta_z')_3]_n^T \tag{3.22}$$

where the prime designates measurement in the frame $X_{nb}Y_{nb}$. Recall that the displacements are written in a local coordinate system attached to the rigid link. As for reactions and torques at the boundaries, it is known that at the end effector, when the manipulator is in free space, the reactions are zero. At the joints, reaction forces and driving torques are present. These reactions must be added to the force vector F_{ng}. The vector representing the reactions is designated

as T_{ng}. For the case of a link described by two elements,

$$T_{ng}=[R_{nx}\ R_{ny}\ \tau_n\ 0\ 0\ 0\ -R_{(n+1)x}\ -R_{(n+1)y}\ -\tau_{n+1}]^T \qquad (3.23)$$

In fact, the solution consists of the deformations, q_n (equation 3.21) and the torques, τ_n. The payload and the effects of an axial load are included into the model of the manipulator.

3.6 Consideration of Payload in Manipulator Model

To include a payload of mass m_p into the manipulator model, it must be incorporated into the element mass matrix and the element stiffness matrix (due to the motion of the reference frame). In addition, the element force vector will be modified to include the payload's inertia due to the global motion. The payload is considered as a lumped mass, therefore, it can be added directly to the mass and stiffness matrices, and the force vector. In these cases, the payload is added only to the last node of the outermost link. For a two-link manipulator this corresponds to the third node of the second link. Consider the inertia forces due to the motion of the payload. This is essentially the product of the payload mass and the acceleration of the end point of the outermost link. Considering only the payload,

the inertia force of the mass in the axial and transverse directions are

$$(F_x)_m = m_p(a_{bx} - \alpha_b(U_y)_3 - \omega_b^2 L_2 - \omega_b^2(U_x)_3 - 2\omega_b(\dot{U}_y)_3 + (\ddot{U}_y)_3) \qquad (3.24)$$
$$(F_y)_m = m_p(a_{by} + \alpha_b L_2 + \alpha_b(U_x)_3 - \omega_b^2(U_y)_3 + 2\omega_b(\dot{U}_x)_3 + (\ddot{U}_x)_3)$$

In the rotational direction, the rotary inertia of the payload about the center of gravity of the last element of the outermost link is

$$(J_\theta)_m = m_p(\frac{l}{2})^2(\alpha_b + (\ddot{\theta}_z)_3) \qquad (3.25)$$

with l being the length of the element. By comparing equations (3.24) and (3.25) to the equations of motion of the manipulator in equation (3.16) one may collect the appropriate terms to determine the element matrices and force vector due to payload mass. In a similar fashion, the gravitational term is added to the element force vector. The payload arm, r_p, is now discussed.

The payload, when it is located at an offsetted length r_p from the end effector (in order to simulate the location of the centre of gravity of a mass), may be modelled in two ways describing the orientation of the payload. First, the payload remains in a horizontal orientation throughout the trajectory to simulate a payload such that it must remain upright during motion. Second, the payload taken as a simple extension of the outer link is studied for comparison purposes. The two configurations are shown in Figure 3.6. Of course, many orientations are possible and all will have their own effects on the dynamics of the arms, but here,

two orientations are investigated. It is assumed that there is a rigid massless connection between the end of the outermost link and the payload, thus the payload location follows the same deformation as the end of the second link. The element mass and stiffness matrices, and the force vector that should be added to the last element matrices and vectors of the outermost link are given in Appendix II.

3.7 Effect of External Axial Force

As the arm moves through a trajectory, lifting a payload, components of the weight will act in the axial direction of the links. Hence, the effects of axial forces due to the weight of the payload in the presence of gravity and even due to the weight of the robot links are now taken into account. First, as the robot manipulates a payload, the axial force depends on the angular position of the robot. That is, the component of the weight considered is one along the link. Second, the axial force acting on an element includes the axial component of the weights of the elements above it and its own weight which is linearly distributed within that element.

Here, an additional stiffness matrix is derived which takes into account these axial forces. In terms of a Timoshenko beam, the contribution of the axial force to the shear force is the product of the axial force and the displacement due to bending [40], which is θ_z. Therefore,

$$P_V = P_x \theta_z \tag{3.26}$$

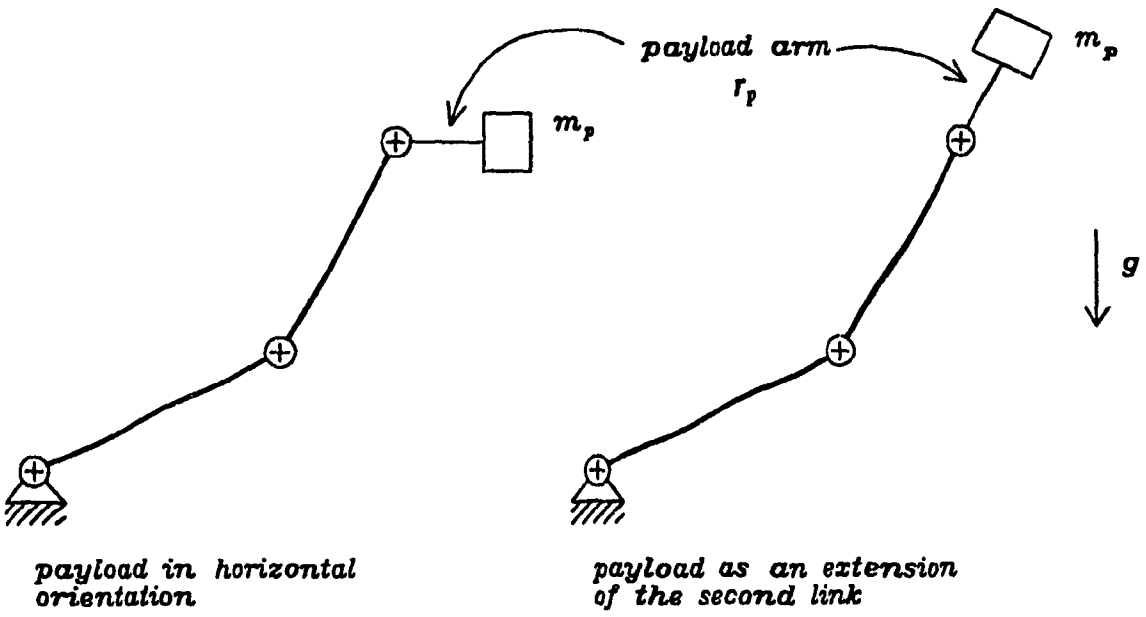

Figure 3.6. Two configurations of payload.

Here P_V is the contribution of axial force P_x to the shear force. Now, consider the potential energy of the Timoshenko beam from which the conventional stiffness matrix and the stiffness matrix due to the axial force may also be derived,

$$P.E._{shear} = \frac{kGA}{2}\int_{x_1}^{x_2}\left(\frac{\partial u_y}{\partial x} - \theta_z\right)^2 dx + \frac{1}{2}\int_{x_1}^{x_2} P_x\theta_z \frac{\partial u_y}{\partial x}dx - \frac{1}{2}\int_{x_1}^{x_2} P_x\theta_z^2 dx \qquad (3.27)$$

The first term on the right side gives the conventional stiffness matrix given in Section 3.4 while the next two terms represent the modification due to axial force P_x . In order to obtain the stiffness matrices, one needs to substitute the nodal expressions for the transverse and the bending deformations.

The axial forces that are considered include the weight of the payload and the weight of the link. First, the weight of the payload is constant throughout the link, but as the robot moves through its path, the magnitude changes. Figure 3.7 shows a typical element under the action of axial forces. The variables, x_1 and x_2 locate the nodes of the element, with respect to the link's driven joint, along the rigid link. The following may be pointed out,

1. P	Axial component of weight of payload.
2. $\rho A n_{el}\, lg \sin(\theta)$	Axial component of weight of elements above current element.
3. $\rho A g\,(x_2 - x)\sin(\theta)$	Axial component of weight of current element as a function of x, from the limits of integration x_1 to x_2 (equation 3.25).

The axial forces on a typical element consist of the weight of the elements above the element plus its own weight which varies linearly within the element. P_x consists of the sum of the three forces above. By substituting into equation (3.27), carrying out the differentation and integration, one obtains the additional stiffness matrices. These matrices which should be added to the stiffness matrices derived earlier are given in Appendix III.

3.8 Solving Over Time: One Step Integration Algorithm

In order to solve for the torques and the deflections over time, one must observe that the mass and stiffness matrices are functions of time. The method referred to as the SS22 algorithm, developed by Zienkiewicz et al. [39] combines the Newmark method, its variants and the Wilson θ method. At present, the algorithm is used to solve the second order matrix equation of the type,

$$M\ddot{q}+C\dot{q}+Kq-F=0 \tag{3.28}$$

Focus is mainly on the quadratic algorithm in which the position vector is approximated by a 2nd order polynomial in time t, that is,

$$q=q_m+\dot{q}_m t+\frac{1}{2}\alpha_m t^2 \quad 0<t<\Delta t \tag{3.29}$$

q_m and $\dot{q}_m$ are the values of the position and velocity (in this case, the deflection and rate of change of deflection) at the beginning of the time interval Δt. The

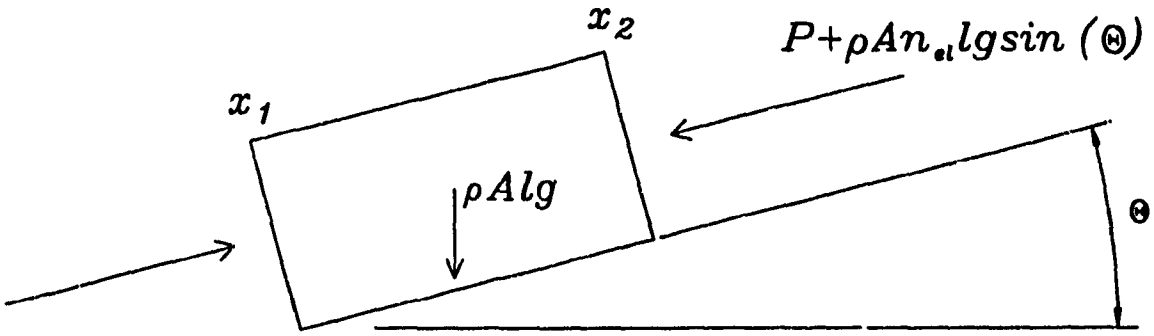

$$P+\rho An_{el}lgsin(\Theta) + \rho Ag(x_2 - x)sin(\Theta)$$

n_{el}: number elements above element

Figure 3.7. Axial forces within elements due to payload and self-weight.

unknown to solve for is α_m (acceleration) from which one can get by the numerical integration procedure, the rate of change of deformation and the elastic deformation itself. The procedure consists of predicting a value of all quantities up to the second last time derivative given starting values for q_m and $\dot{q}_m$. The steps for the quadratic algorithm are [39]

INITIAL ESTIMATE:

$$\begin{aligned} \tilde{q}_{m+1} &= q_m + \dot{q}_m \Delta t \Theta_1 \\ \tilde{\dot{q}}_{m+1} &= \dot{q}_m \end{aligned} \tag{3.30}$$

EVALUATION OF ACCELERATION:

$$\alpha_m = (M(t+\Delta t) + \Delta t \Theta_1 C(t+\Delta t) + \frac{\Delta t^2}{2} \Theta_2 K(t+\Delta t))^{-1} (F(t+\Delta t) - C(t+\Delta t)\tilde{\dot{q}} - K(t+\Delta t)\tilde{q}) \tag{3.31}$$

NUMERICAL INTEGRATION:

$$\begin{aligned} q_{m+1} &= q_m + \Delta t \dot{q}_m + \alpha_m \Delta t^2/2 \\ \dot{q}_{m+1} &= \dot{q}_m + \alpha_m \Delta t \end{aligned} \tag{3.32}$$

An estimate of the error is given as [39]

$$E_{est} = \frac{\Delta t^2}{3!} (\alpha_m - \alpha_{m-1}) \tag{3.33}$$

Therefore, the smaller this error, the more accurate the solution to the acceleration is. To continue, according to the Newmark algorithm, the parameters Θ_1 and Θ_2 can

be compared to the Newmark parameters γ and β with the following relations [39],

$$\begin{aligned} \gamma &= \Theta_1 \\ \beta &= 0.5\Theta_2 \end{aligned} \tag{3.34}$$

These parameters are related to numerical stability and allow the current algorithm to embrace others by substituting different values to the parameters [39] [41]. Some advantages of the algorithm include [39]

- only the value and first derivative of q_m is required (natural initial conditions).
- the governing equation is satisfied on average.
- time varying matrices may be included.

To illustrate the solution procedure, a case study of a two-link flexible manipulator is attempted and results are presented in Chapter 4.

3.9 Two-Element Example

As an example, in preparation for the simulation in the next chapter, consider the solution of a two-link planar manipulator with each link divided into two finite elements to save computational time. First of all, the two equations of motion are obtained (one for each link) which consist of assembled matrices expressed in a

moving frame taken parallel to the global frame,

$$\begin{aligned} M_{1g}\ddot{q}_{1g}+C_{1g}\dot{q}_{1g}+K_{1g}q_{1g}&=F_{1g}+T_{1g} \\ M_{2g}\ddot{q}_{2g}+C_{2g}\dot{q}_{2g}+K_{2g}q_{2g}&=F_{2g}+T_{2g} \end{aligned} \tag{3.35}$$

These equations are written in their respective local coordinates which are attached to their respective rigid motion position. Here, with boundary conditions in place, the deflections are given as,

$$\begin{aligned} q_{1g}&=[0\ 0\ 0\ (U_x')_2\ (U_y')_2\ (\theta_z')_2\ (U_x')_3\ (U_y')_3\ (\theta_z')_3]_1^T \\ q_{2g}&=[0\ 0\ 0\ (U_x')_2\ (U_y')_2\ (\theta_z')_2\ (U_x')_3\ (U_y')_3\ (\theta_z')_3]_2^T \end{aligned} \tag{3.36}$$

and the reaction vectors are found to be,

$$\begin{aligned} T_{1g}&=[R_{1x}\ R_{1y}\ \tau_1\ 0\ 0\ 0\ R_{2x}\ R_{2y}\ \tau_2]^T \\ T_{2g}&=[-R_{2x}\ -R_{2y}\ -\tau_2\ 0\ 0\ 0\ 0\ 0\ 0]^T \end{aligned} \tag{3.37}$$

The outer equation may be solved first (here, the equation corresponding to the second link) and then work out the solution until the base joint is reached. If proceeded in this fashion, the deflections in the second link are obtained followed by its reactions and applied torque. Substitution of the reactions and torque into the first link's equation leads to the deformations in the first link and finally to the reaction at the base of the first link and joint torque. In summary, there are 12

equations and 12 unknowns. They can be solved for the unknown displacements using the SS22 one-step integration algorithm. The reactions and torques then can be obtained by back substitution into the individual link equations, that is, equation (3.35).

Chapter 4

RESULTS AND DISCUSSION

Implementation of the derivation from the previous chapter through a computer program written in MATLAB provides some results which are presented and discussed here.

4.1. Preliminary

The manipulator described in the previous chapter consists of two non-rigid links with the material properties (Aluminum) given in Table 4.1. The gravitational

Table 4.1. Material Properties of Links [34] [35].

Density	2715 kg/m^3
Young's Modulus	7.11×10^{10} N/m^2
Shear Modulus	2.62×10^{10} N/m^2
Yield Strength	2.1×10^{8} N/m^2

acceleration used is g = 9.81 m/s^2. Joint trajectories consist both of a step input and a cycloidal input. The step input allows one to see how the system behaves to an instantaneous change in position and serves to verify the formulation. In this case, the final position of both joints (θ_1 and θ_2 from Figure 3.1) is $\pi/4$ radians.

The next trajectory consists of the cycloidal motion which represents a simple pick and place maneuver. It is given as

$$\theta_i = \theta_{if}\left(\frac{t}{t_f} - \frac{1}{2\pi}\sin\left(\frac{2\pi t}{t_f}\right)\right)$$

where θ_{if} and t_f are the final joint position and the final time respectively. With this trajectory, the final position for both joints is taken as $\pi/2$ radians. The final time is 1 s while the time step in the numerical integration is 0.004 s. The trajectory is shown in Figures 4.1, 4.2, and 4.3.

In order to save time and amount of computations, two finite elements are used to describe each of the links in the manipulator. More elements would lead to larger matrices and hence longer computation times, but yield closer approximations.

In all the simulations, the "Newmark-like" parameters, Θ_1 and Θ_2, are set at 0.7 such that they represent some intermediate value between 0.5 and 1.0. With this value, some artificial damping is provided. As a consequence, the effects of the payload can be seen more clearly [39]. The high frequency oscillations present in the results will be artificially reduced so as to clearly show the payload's effects on the results. Only in the case of minimum and maximum numerical damping they are assigned the value of 0.5 and 1.0, respectively. The case of minimum numerical damping represents the physical model. The effect of these parameters is demonstrated.

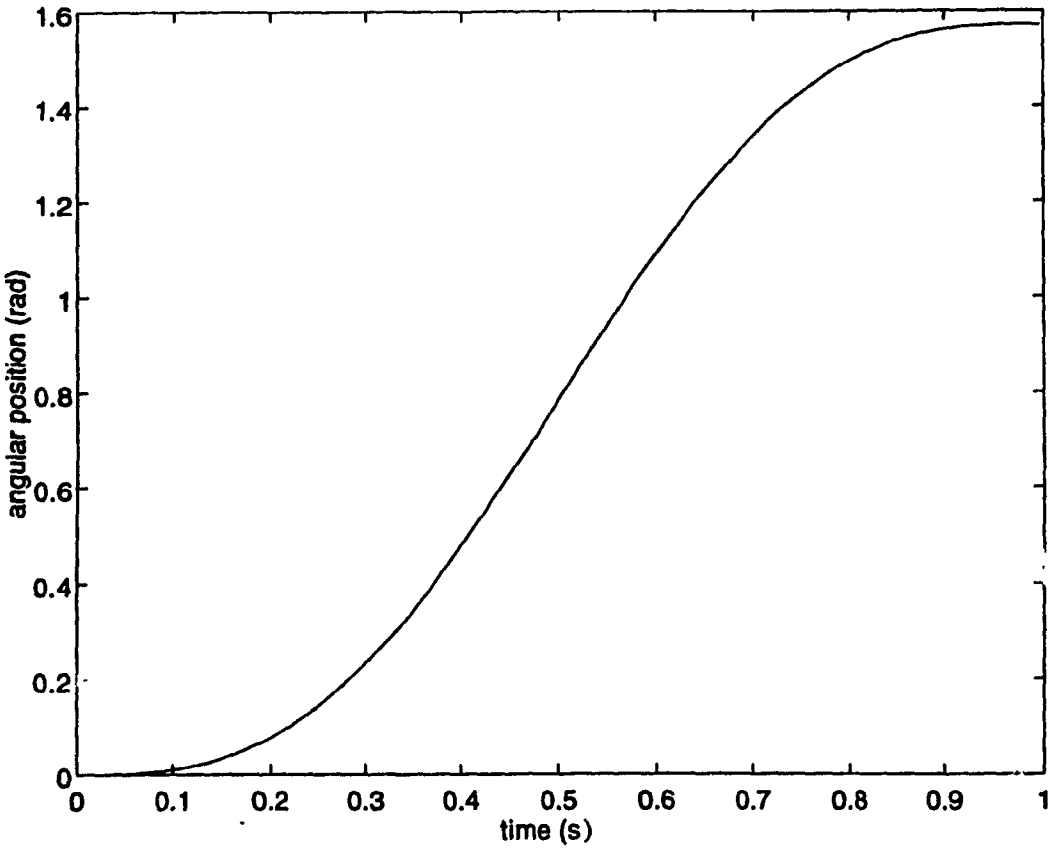

Figure 4.1. Angular position of first link.

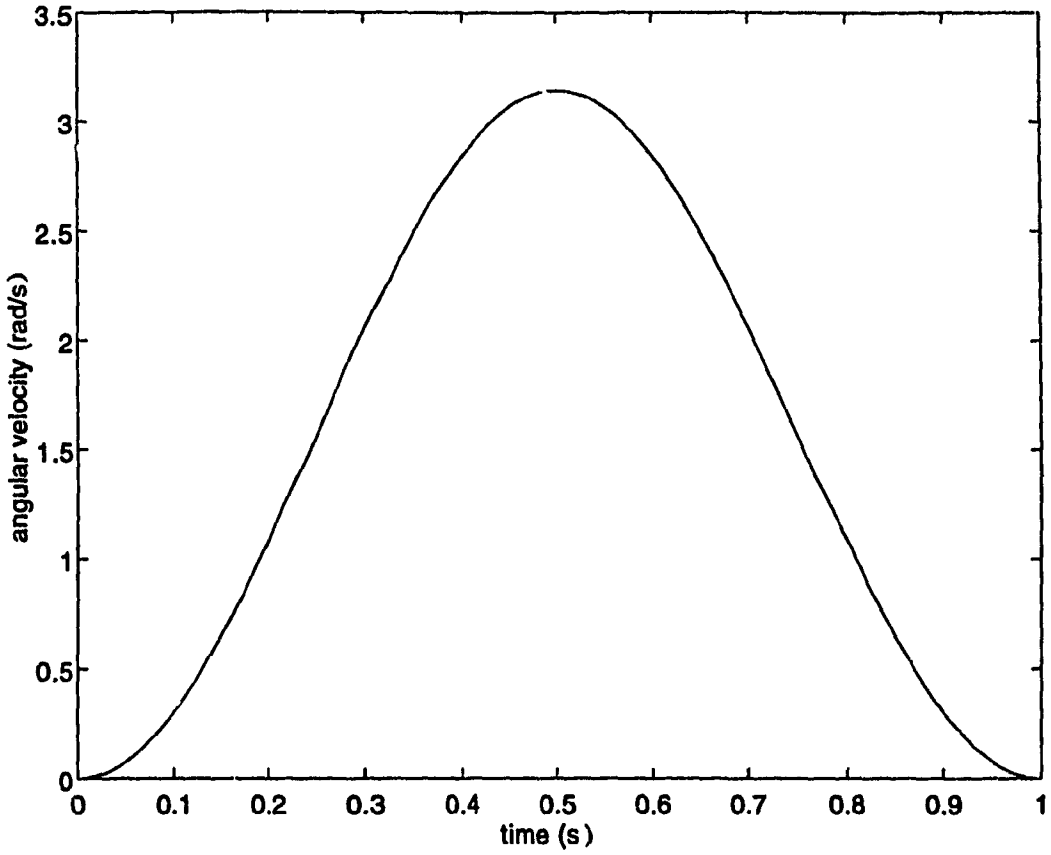

Figure 4.2. Angular velocity of first link.

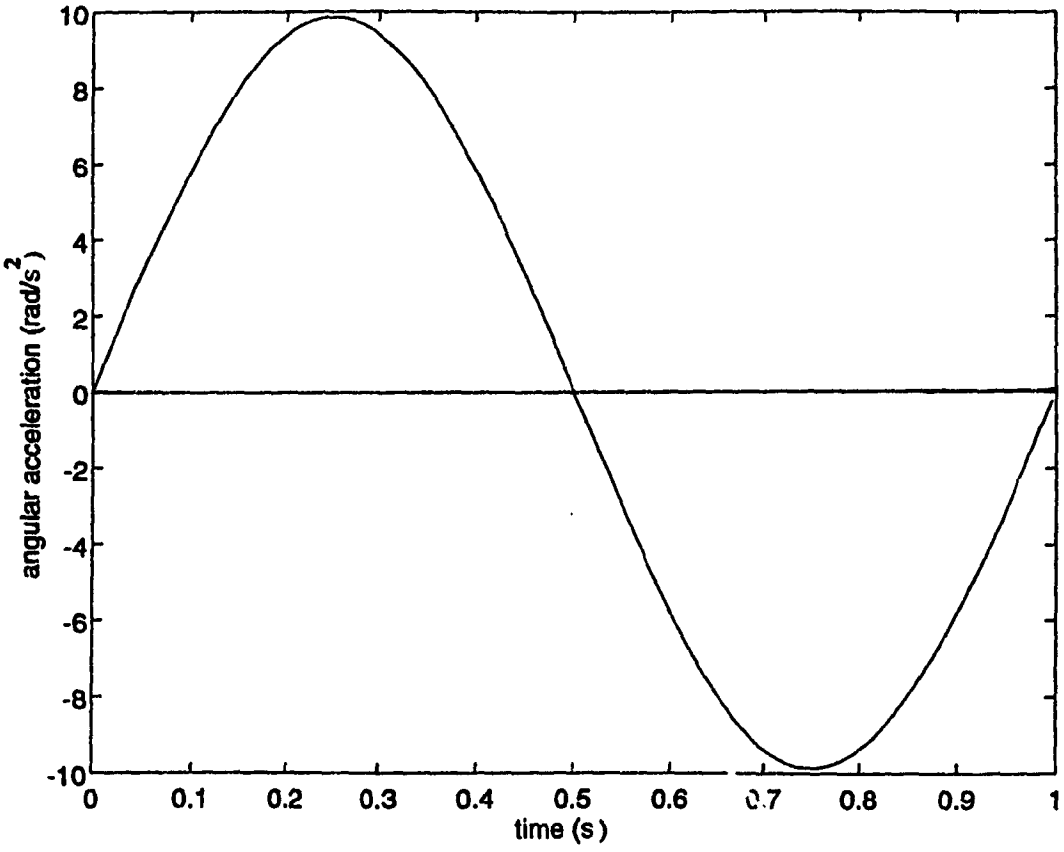

Figure 4.3. Angular acceleration of first link.

The results include torque time histories about the respective rigid links torque, the axial and transverse forces within the elements, and the respective deflections as time functions. The results reveal the effects on manipulator performance of the following:

1. Variation in payload mass and orientation.
2. Variation of link length and cross sectional size (with payload).
3. Variations in the integration parameters, Θ_1 and Θ_2.

In order to verify the model, the manipulator is made rigid by increasing Young's modulus. As Young's modulus increases, the manipulator links become more rigid. Comparisons are made in Appendix IV, and show that deflections have decreased and torques correspond very closely to the rigid links torque.

The maximum payload that a manipulator may carry (in open loop) is determined by several factors, one of which is flexibility of its links. The criteria used to determine whether the manipulator has reached its maximum payload capacity is failure by either buckling (exceeding the critical buckling load found by an eigenvalue analysis) or by yielding (for more rigid links) [32]. This is observed specially when the manipulator is to follow the cycloidal trajectory since payload capacity depends on trajectory.

4.2. Response to Step Trajectory

First, the response of a two-link flexible manipulator to a step trajectory is investigated. Variations of payload and its arm (location of payload centre of

gravity relative to the end effector), the manipulator size, and the changes in the numerical integration parameters are observed. Furthermore, this type of trajectory, as a simple case, is used to verify the model. The initial position is chosen horizontal for both links. The final position of the links is $\pi/4$ radians as shown in Figure 4.4. This trajectory is chosen with the intention to test the manipulator arm at an unstable position.

4.2.1 Effect of Payload and Payload Arm

While keeping the cross section of the links as a square, the effects of the payload at the end effector are studied. To study the effect of a payload arm, the load is located a distance r_p from the end effector. The effect of orientation of the payload is also investigated.

A two-link manipulator with cross sectional dimensions of $b = h = 0.02$ m, and link lengths of $L_1 = L_2 = 1$ m without a payload is simulated first. The torque required to drive the links to follow the step input and to maintain the manipulator in the final position is given in Figure 4.5. A plot of the torque for the rigid body case is presented for comparison. As it can be seen, the torque values for the flexible links oscillate about torque values for the rigid links; a phenomenon also observed by other researchers [14] [15] [19]. The gradual decay is due to the numerical damping and shows that the torque for flexible links indeed varies about the torque for rigid links to which it converges. The driving torque is virtually

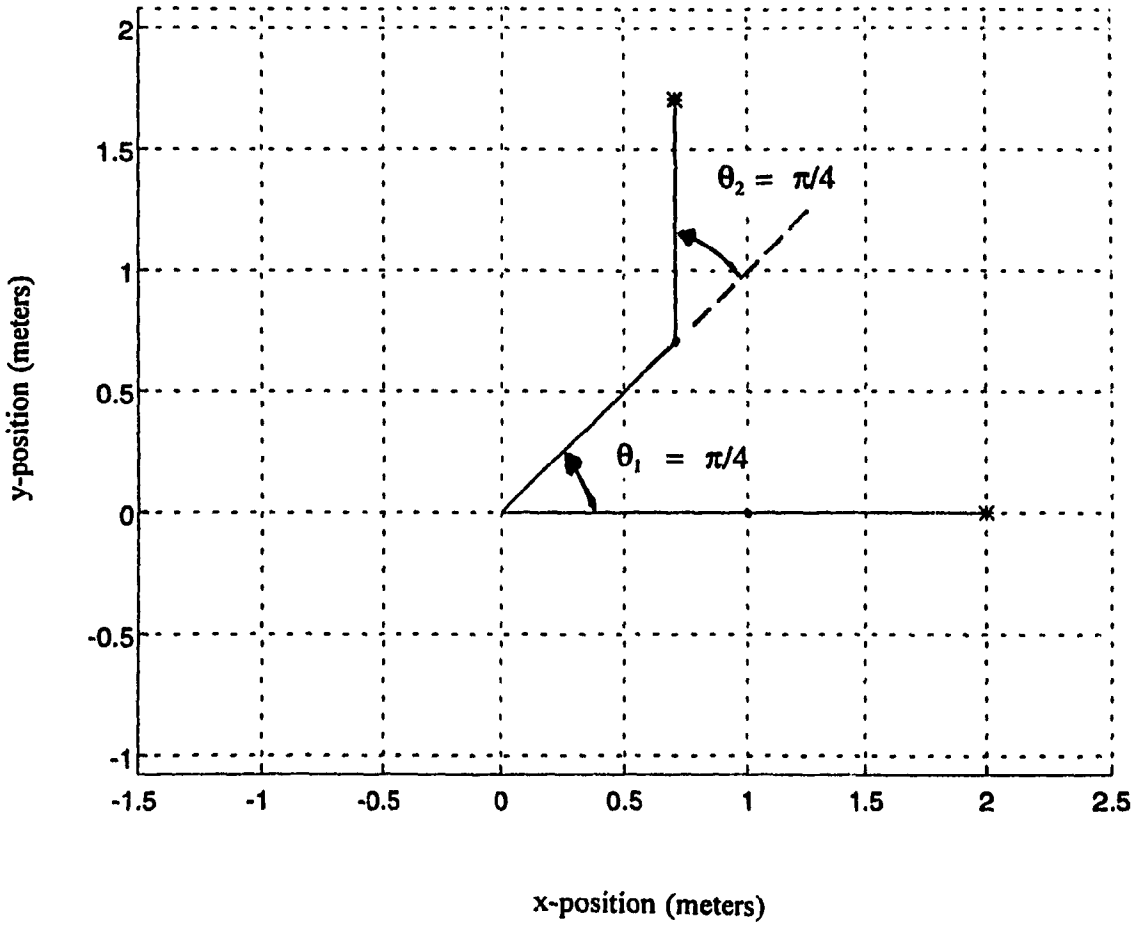

Figure 4.4. Initial and final position of manipulator for step response, $\theta_1 = \theta_2 = \pi/4$.

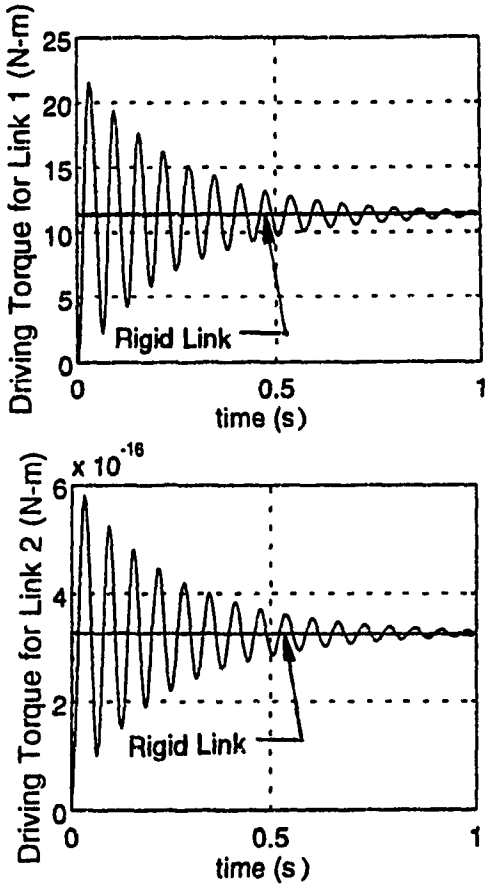

Figure 4.5. Driving torques for step response, $\theta_1 = \theta_2 = \pi/4$, $b = h = 0.02$ m, no payload.

zero for the second link since this link does not require any torque to remain in the vertical position. However, for the flexible links, since the step input acts as a shock, oscillations in torque value are prominent as the link end (being the furthest point from the corresponding base joint) of each link is constrained, by the model, to the same kinematics as the corresponding rigid links model. Since all initial conditions are set to zero including forces, a step force equal to the weight of the links is present. This acts as a constant force on the system and causes the large magnitude oscillations. As the manipulator maintains its position under the influence of gravity, the torques oscillate with a magnitude twice the rigid links torque since, first it must compensate for the weight of the manipulator to maintain the position, and second, it must compensate for the flexibility in the system which is excited by the constant gravitational force. For the rigid links case, this system is essentially static, but it is evident that periodic variations are generated as a result of the flexible links. Even when the torques are small, as for the second link, these periodic vibrations are present, yet insignificant in magnitude.

The trends observed in the driving torques are found for the transverse nodal deflections as illustrated in Figure 4.6. The nodes represent points along the links. For a two-element link with the discretization described in Chapter 3, there are three nodes: the driven joint (node 1), the midpoint of the link (node 2) and the end-point of the link (node 3). The deflections represent the position of the nodes with respect to the rigid links motion for each node. As expected, the axial

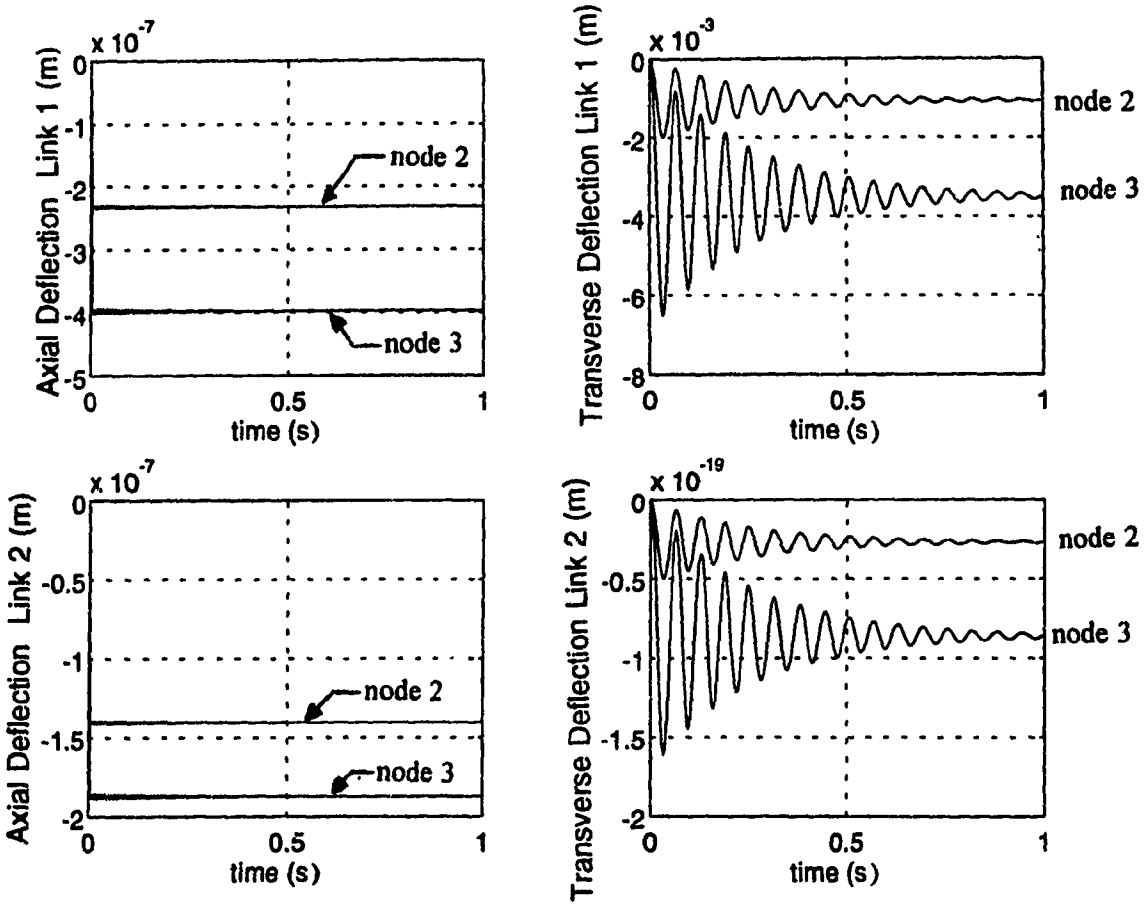

Figure 4.6. Axial and transverse deflections due to step response, $\theta_1 = \theta_2 = \pi/4$, $b = h$ = 0.02 m, no payload.

deflections are small (of the order of 10^{-7}) as are the high frequency oscillations, indicating high stiffness in the axial direction. Since the first link's end-point deflects, the second link will not be exactly vertical, therefore, when computing the transverse component of the deflection of that link, it is very close to zero. This also causes the slight deviation off the corresponding rigid links torque. However, the first link deflects transversely as it holds a payload of mass 1.09 kg, the mass of the second link, and maintains the same position. The end-point deviation is slightly over 6 mm and its nominal value is close to 4 mm.

A payload of 5 kg at the end-effector yields the results shown by the plots in Figures 4.7 and 4.8 for the torques and the deflections respectively. For the second link, the torques and deflections exhibit a decrease in frequency of oscillations, from 16 Hz to 3.5 Hz. The values are insignificant once again for the same reasons stated above, but the effect of payload is seen. It induces a lower frequency oscillation, effectively reducing the stiffness of the second link. However, in the first link, close frequency of oscillations is observed, that is 16 Hz, as in the case without payload. Evidently, the 5 kg payload does not affect the first link significantly in terms of stiffness. Increasing the mass of payload significantly would have a similar effect on the first link as the 5 kg payload has on the second link. Further, axial deflections shown in Figure 4.8 as compared to those of Figure 4.6 for the case without payload indicate that the links undergo larger compression and they exhibit larger amplitude high frequency compression-tension.

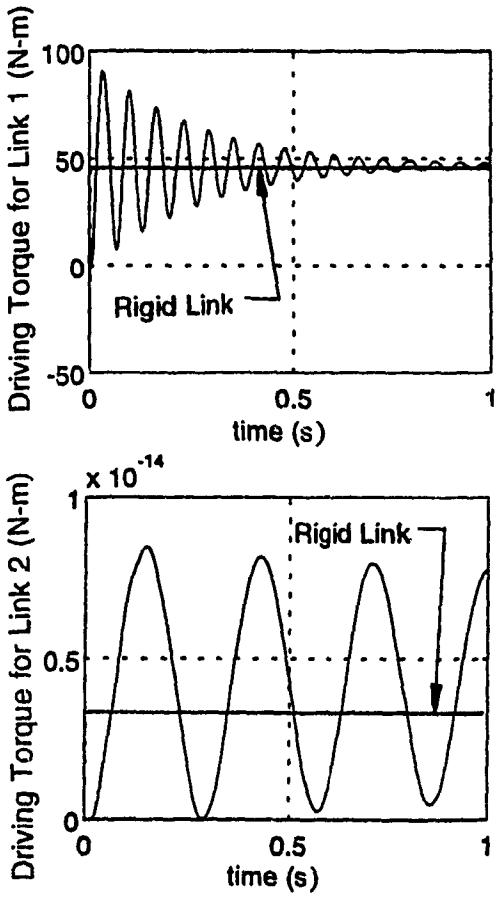

Figure 4.7. Driving torques for step response, $\theta_1 = \theta_2 = \pi/4$, $b = h = 0.02$ m, $m_p = 5$ kg.

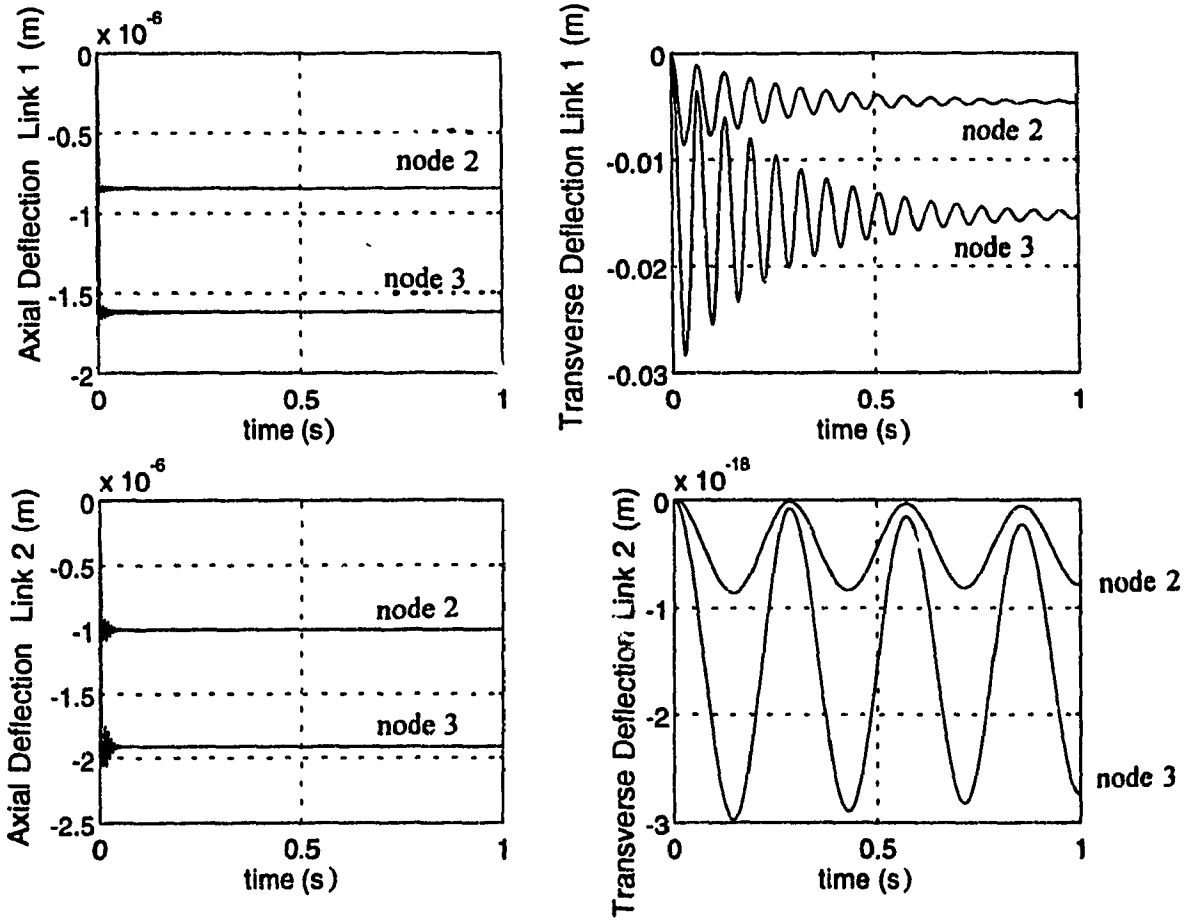

Figure 4.8. Axial and transverse deflections due to step response, $\theta_1=\theta_2=\pi/4$, $b=h=0.02$ m, $m_p = 5$ kg.

Once the mass is located a small distance away from the end-effector, several effects are evident. The results with the same load of 5 kg located 0.4 m away from the end-effector remaining in a horizontal position relative to it are shown in Figures 4.9 to 4.11. In these plots, two oscillations are revealed, a fast oscillation and a slow one. The fast oscillation at 16 Hz decays once again due to the numerical damping. The other takes much longer time to fade out. The high frequency curve is evident from previous plots (Figures 4.5 and 4.7 among others). This is mainly caused by the instantaneous nature of the trajectory and the force due to gravity. Under these conditions, the model constrains the kinematics of each link's end-point to be the same as those of the rigid links' model. The slow oscillations (approximately 3.5 Hz) are due to the payload and its offset. The first link is also affected, whereas in Figure 4.7 the effects of a small payload offset (caused by the deflection of the end-point of the first link) were insignificant. It is seen in Figures 4.10 and 4.11 that the transverse deflections and forces are mostly affected by the payload offset. The axial deflection of the second link remains unchanged as compared to that of Figure 4.8. The force acting along link 2, which remains vertical, is still 49.1 N in addition to the weight of link 2, 10.7 N. Meanwhile, the first link is rotated $\pi/4$ radians. Since the effect of payload is significant, it is transmitted in both axial and transverse directions contrary to Figure 4.8 where the effects were negligible. Comparing Figures 4.10 and 4.8, the maximum average deflection in compression is still small, just over 0.0015 mm,

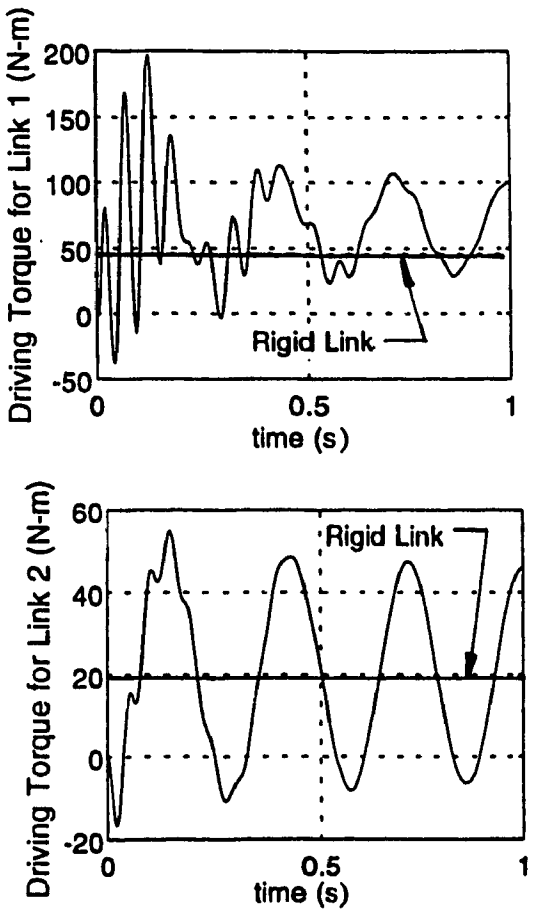

Figure 4.9. Driving torques for step response, payload in horizontal orientation.

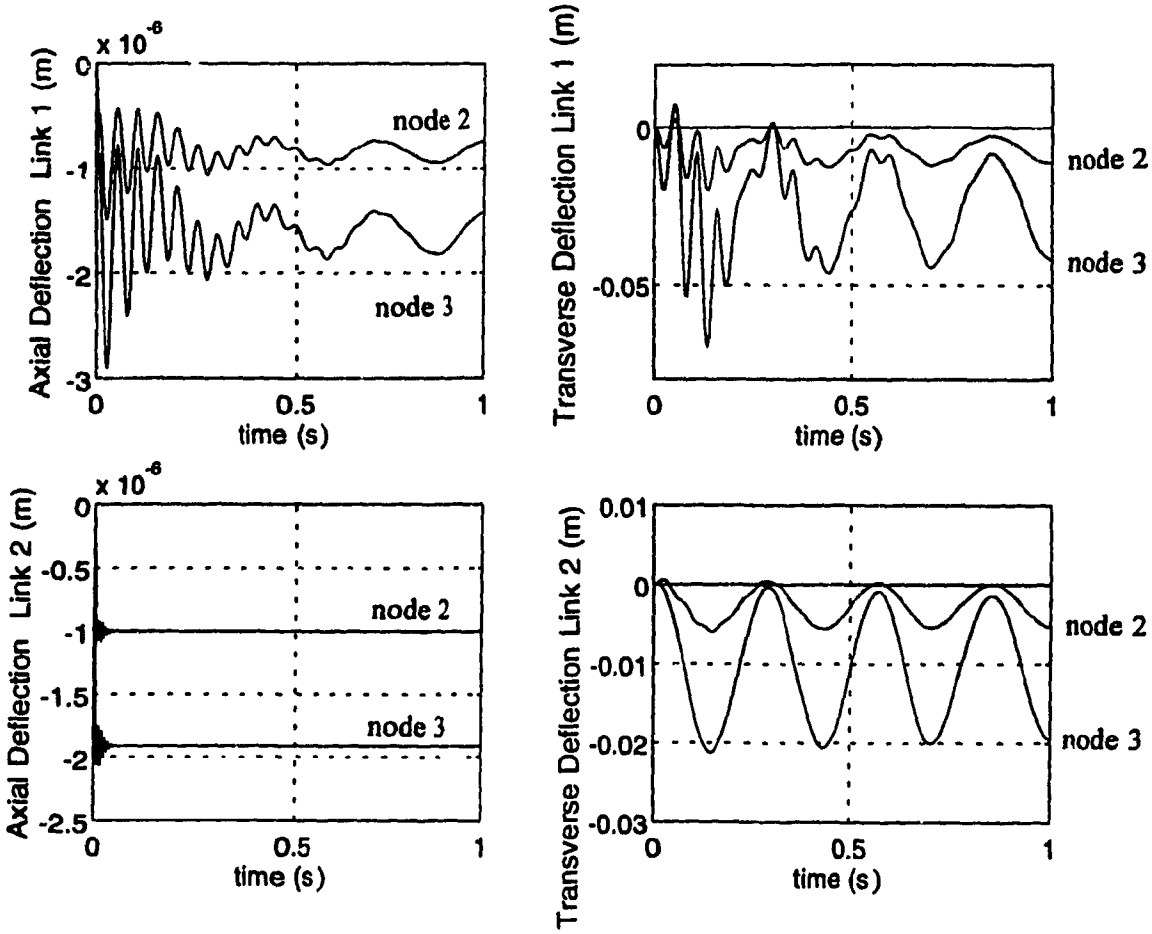

Figure 4.10. Axial and transverse deflections due to step response, payload in horizontal orientation.

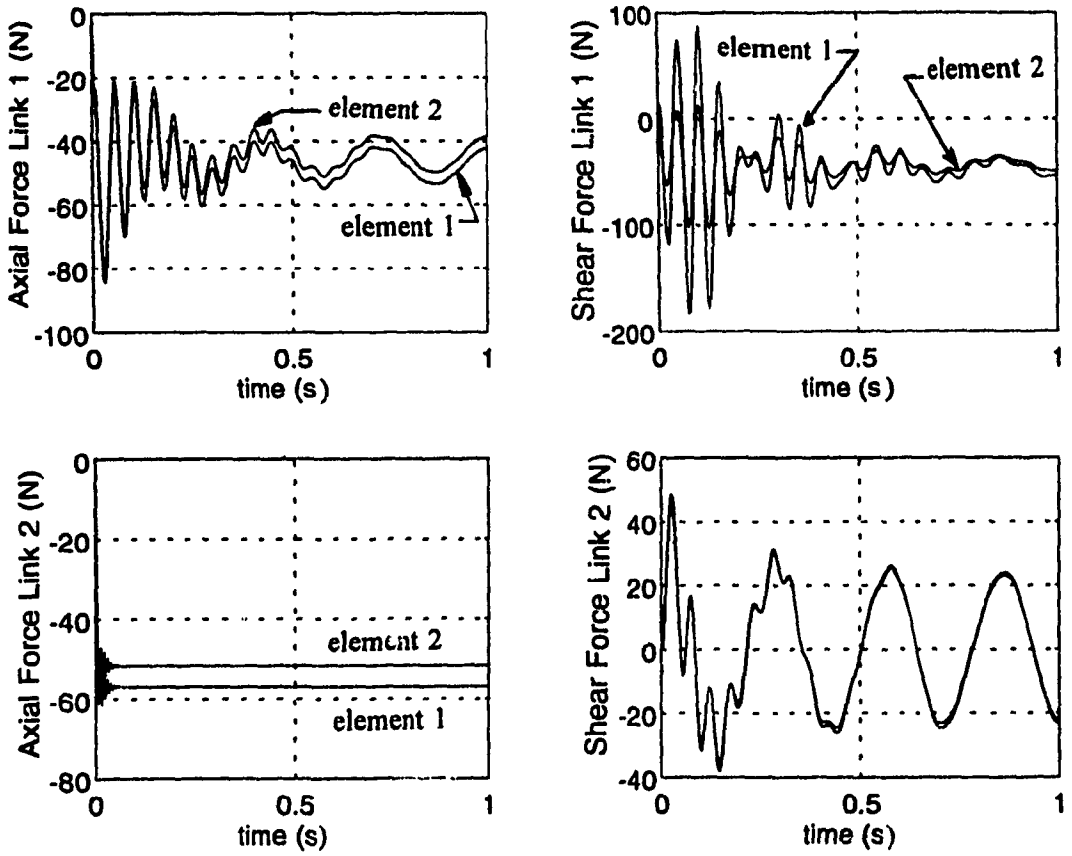

Figure 4.11. Axial and shear forces due to step response, payload in horizontal orientation.

only the period of oscillations and driving torques have changed. The maximum transverse deflection of the end-point of the first link is just over 5 cm while the second link experiences an end point deflection of 2 cm. The displaced payload essentially induced a moment generating larger transverse deflections.

In order to study how the load orientation affects the manipulator, an investigation of the payload as an extension of the second link is undertaken. Time histories of the torques, deflections and internal forces are illustrated in Figures 4.12 to 4.14. Comparing the driving torques on joint 1 in Figure 4.12 reveals that they are equal to those in Figure 4.7, the case with no payload arm. A downward force of 59.8 N (close to the magnitude of the maximum axial force in link 2, the discrepancy being due to discretization) is acting on the free end of link 1 in both plots. The major difference occurs in link 2 where the frequency of oscillations reduced from 3.5 Hz in Figure 4.7 to 2.5 Hz in Figure 4.12. As explained earlier, since the second link is oriented slightly off the vertical position, the oscillatory displacements and forces in the transverse direction are nonetheless affected. Again, the payload arm induced a decrease in the frequency of the response which was clearly shown for the payload horizontally offset from the end-effector. In fact, the payload and its offsetting from the end-effector greatly alter the system characteristics. For example, the lower frequency vibrations indicate a reduction in stiffness. Also, caution should be taken to keep the system within safe limits with respect to resonant frequency in order not to excite the natural modes of the

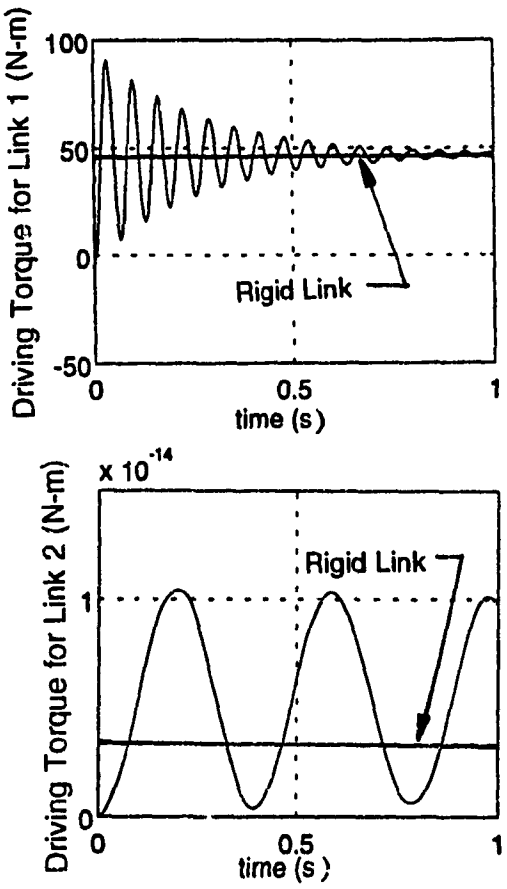

Figure 4.12. Driving torques for step response, extended payload, m_p = 5 kg.

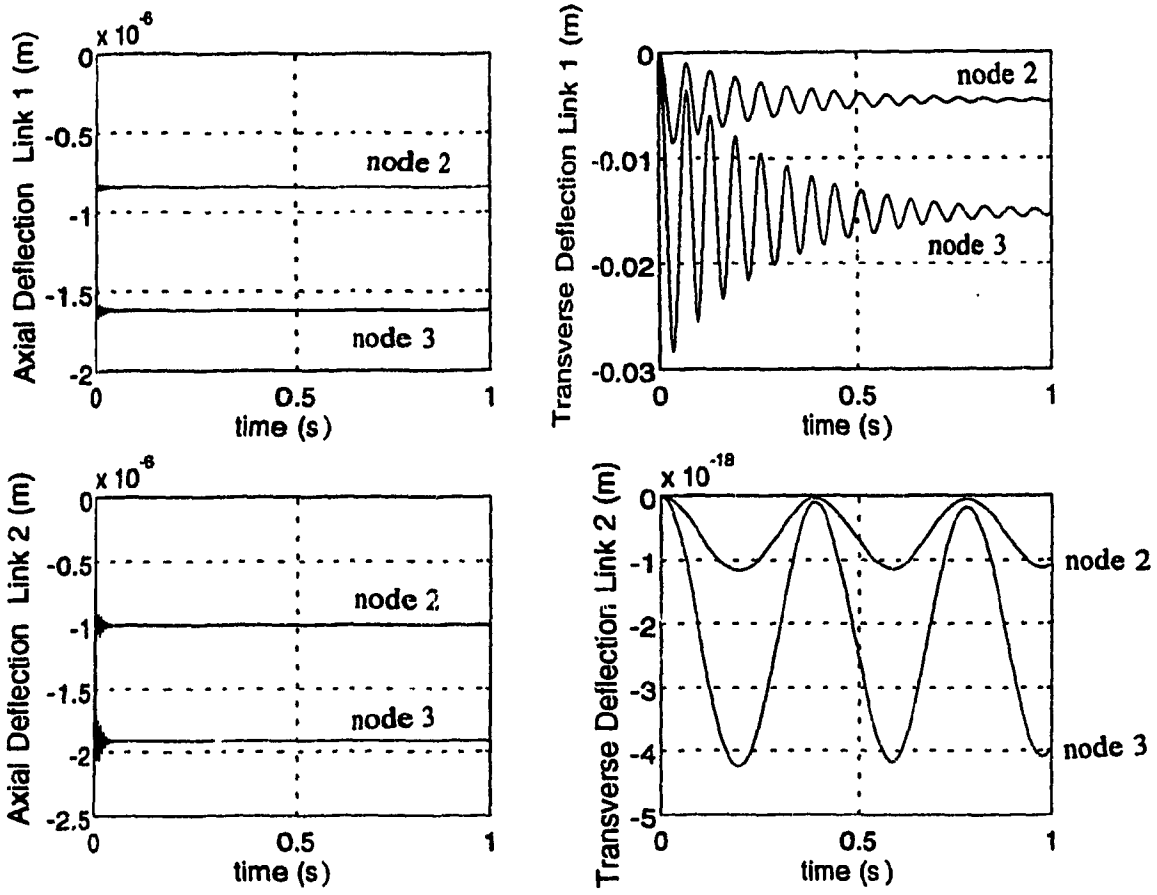

Figure 4.13. Axial and transverse deflections for step response, extended payload.

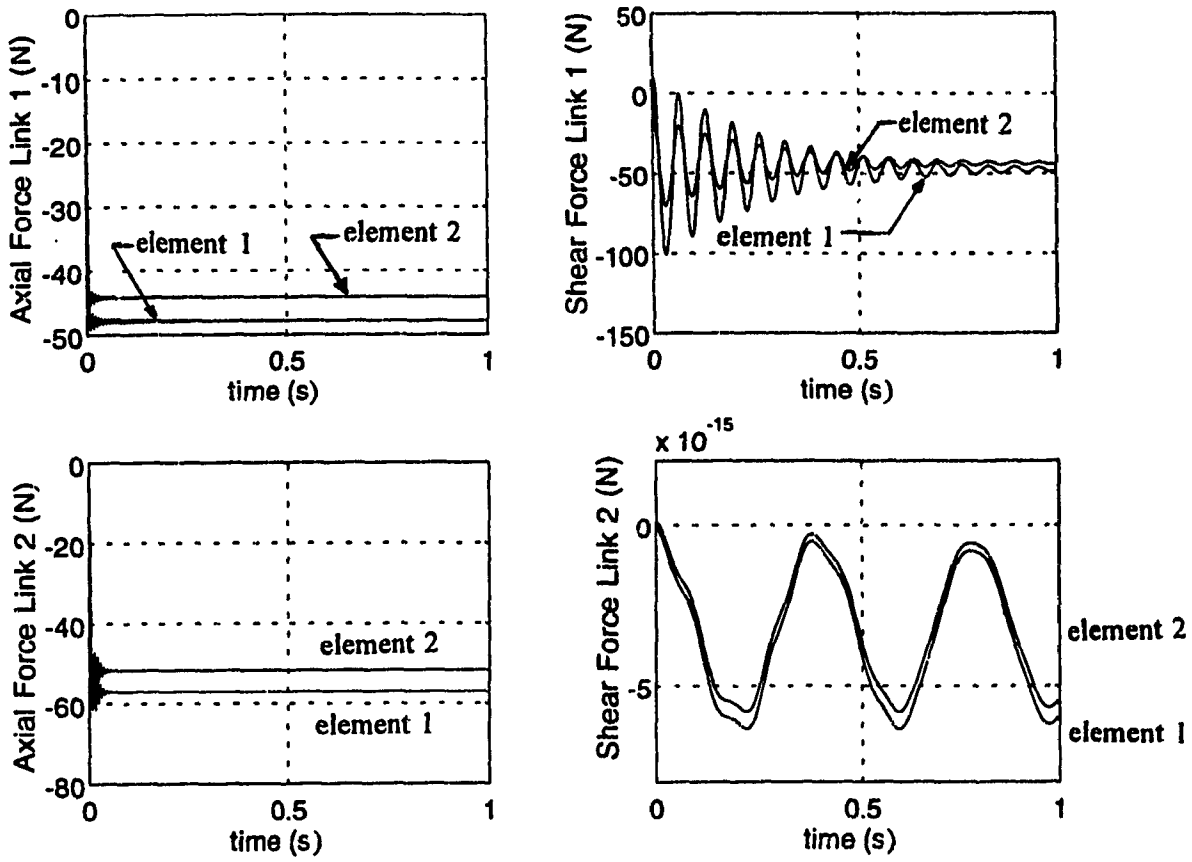

Figure 4.14. Axial and shear forces, step response, extended payload.

links since the different magnitudes and different offsets of the payload affect the oscillatory characteristics of the response.

4.2.2. Effect of Manipulator Dimensions

Several results are presented which illustrate the effects of manipulator dimensions such as length and cross section size while carrying a payload at the end effector. These parameters include a payload of 3 kg, and a payload arm r_p = 0 m. Full square cross sections as well as a hollow square cross section are studied for comparison. Figures 4.15 and 4.16 illustrate the driving torques for two manipulators with square cross sections of dimensions 0.02 m and 0.05 m, respectively. The notable difference between the two is a resulting increased rigidity. The initial disturbances decay more rapidly in the case of the larger cross section. The driving torques in Figure 4.15 resembles those in Figure 4.7. But, there is a significant increase in frequency of link's 2 applied torque as a consequence of the reduced mass. For the larger cross section, the oscillations of the link's 2 driving torque are of higher frequency, 23 Hz as compared to 4.5 Hz for the reduced cross section, indicating a lesser sensitivity to payload effects. Higher frequency of response indicates higher stiffness of the system.

A comparison of Figure 4.17 to Figure 4.18 allows assessment of the contribution of the payload to the axial and shear forces. Figure 4.17 illustrates the shear and axial forces in the two links without a payload while Figure 4.18 shows

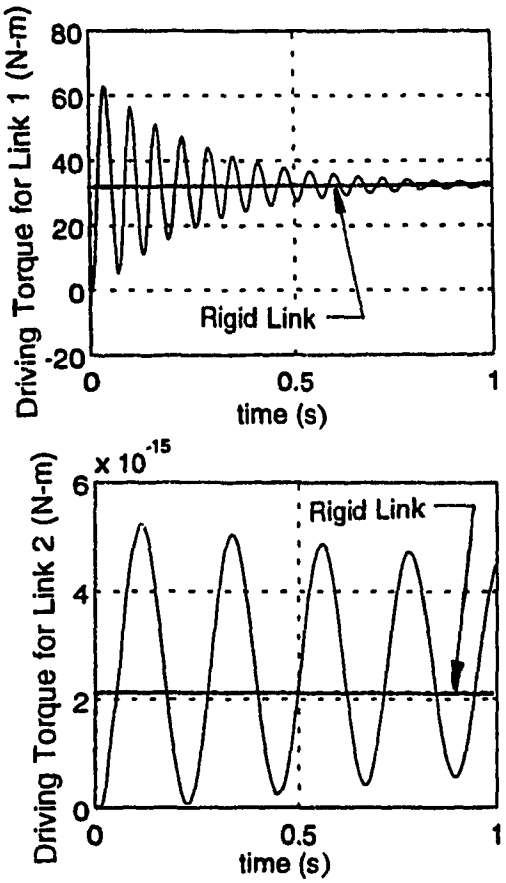

Figure 4.15. Driving torques for step response, $b = h = 0.02$ m, $r_p = 0$.

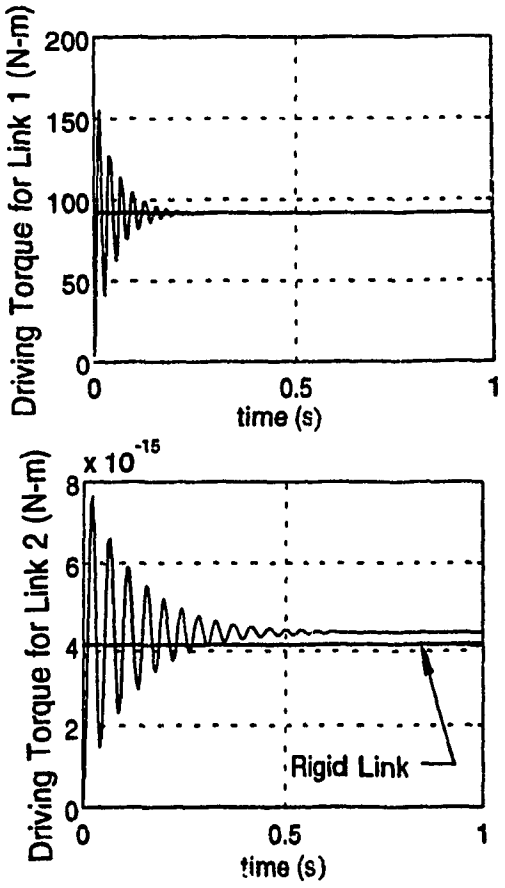

Figure 4.16. Driving torques for step response, $b = h = 0.05$m, $r_p = 0$.

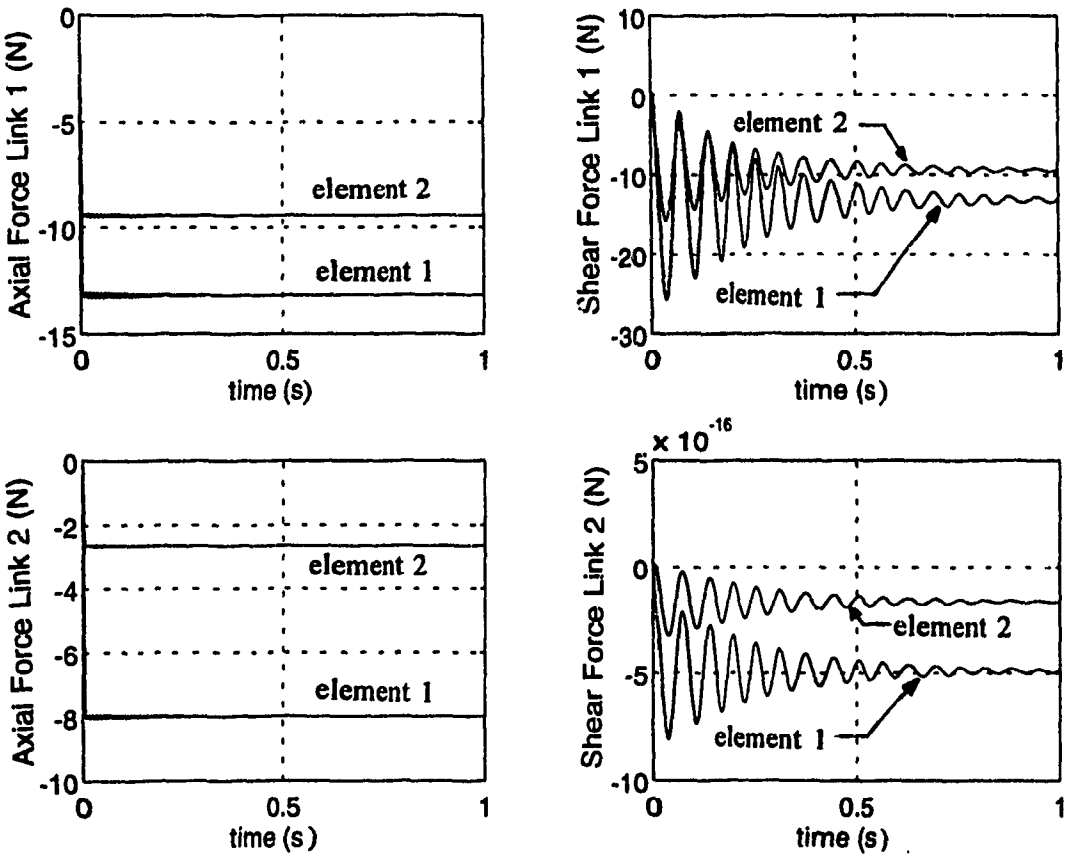

Figure 4.17. Axial and shear forces, step response, $b = h = 0.02$m, no payload.

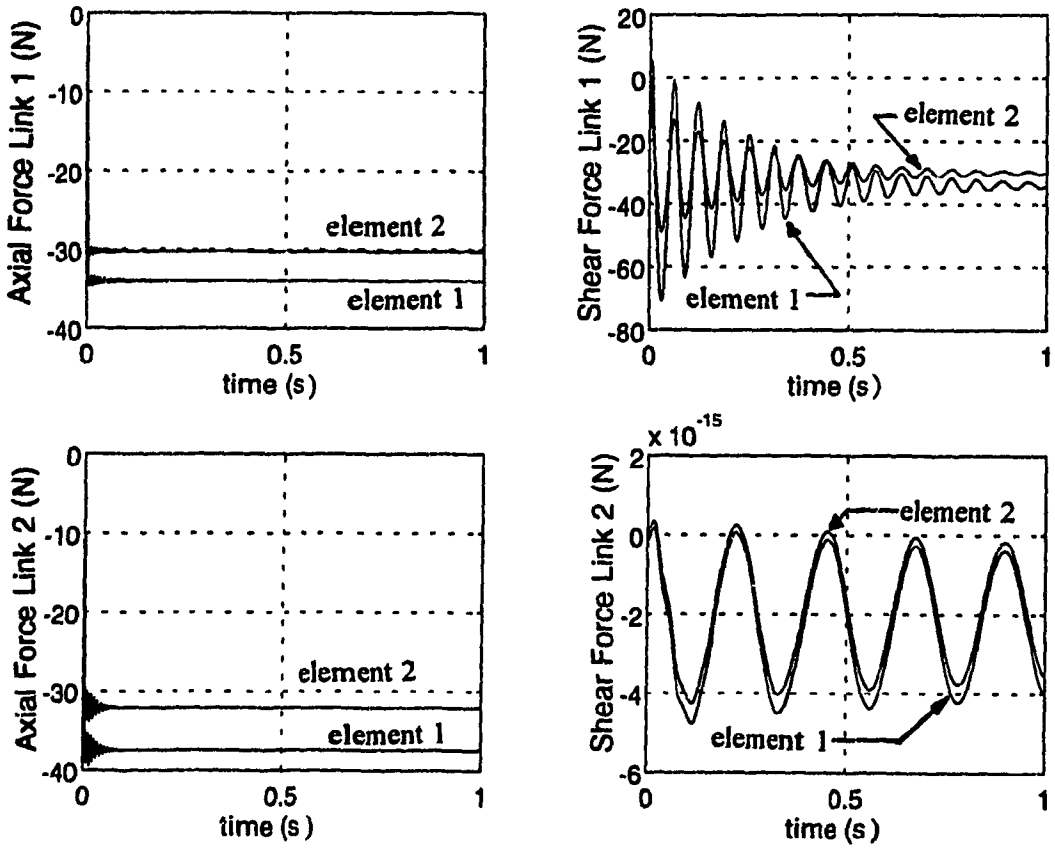

Figure 4.18. Axial and shear forces, step response, $b = h = 0.02$m, $m_p = 3$ kg.

the same results for a payload mass of 3 kg. The contribution of payload becomes significant to the force system as the ratio of payload mass to manipulator mass increases. With reference to Figure 4.19 for a larger cross section, axial and transverse forces are dependent on the weight of the links as depicted by the larger difference between element forces. Here, the payload mass to manipulator mass ratio is 0.22 compared to the previous case where it is 1.4. Large ratios indicate the importance of the payload as part of the manipulator. From these results, heavier payloads as well as larger cross sections lead to larger internal forces. For design considerations, manipulators with slender links should be able to withstand axial forces while manipulators with less slender links (which are more susceptible to shear failure [35]) should be able to withstand the higher shear forces.

Finally, Figures 4.20 and 4.21 indicate that smaller cross section links undergo larger deflections. For the square cross section of 2 cm, the maximum end-point deflection approaches 2.0 cm while the thicker cross section of 5×5 cm exhibit a maximum end-point deflection of 1.2 mm. This is in accordance with an increased rigidity of the links.

Further, aspects of using a hollow cross section or a solid cross section are

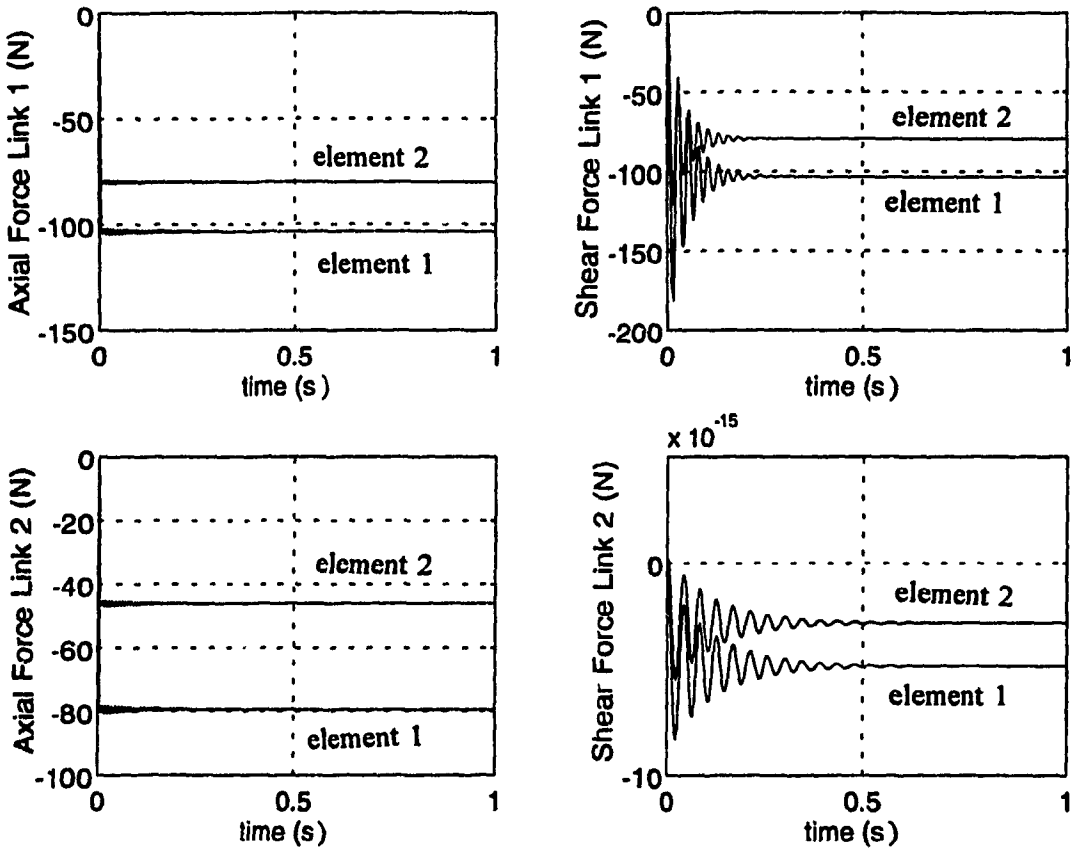

Figure 4.19. Axial and shear rorces, step response, $b = h = 0.05$m, $m_p = 3$kg.

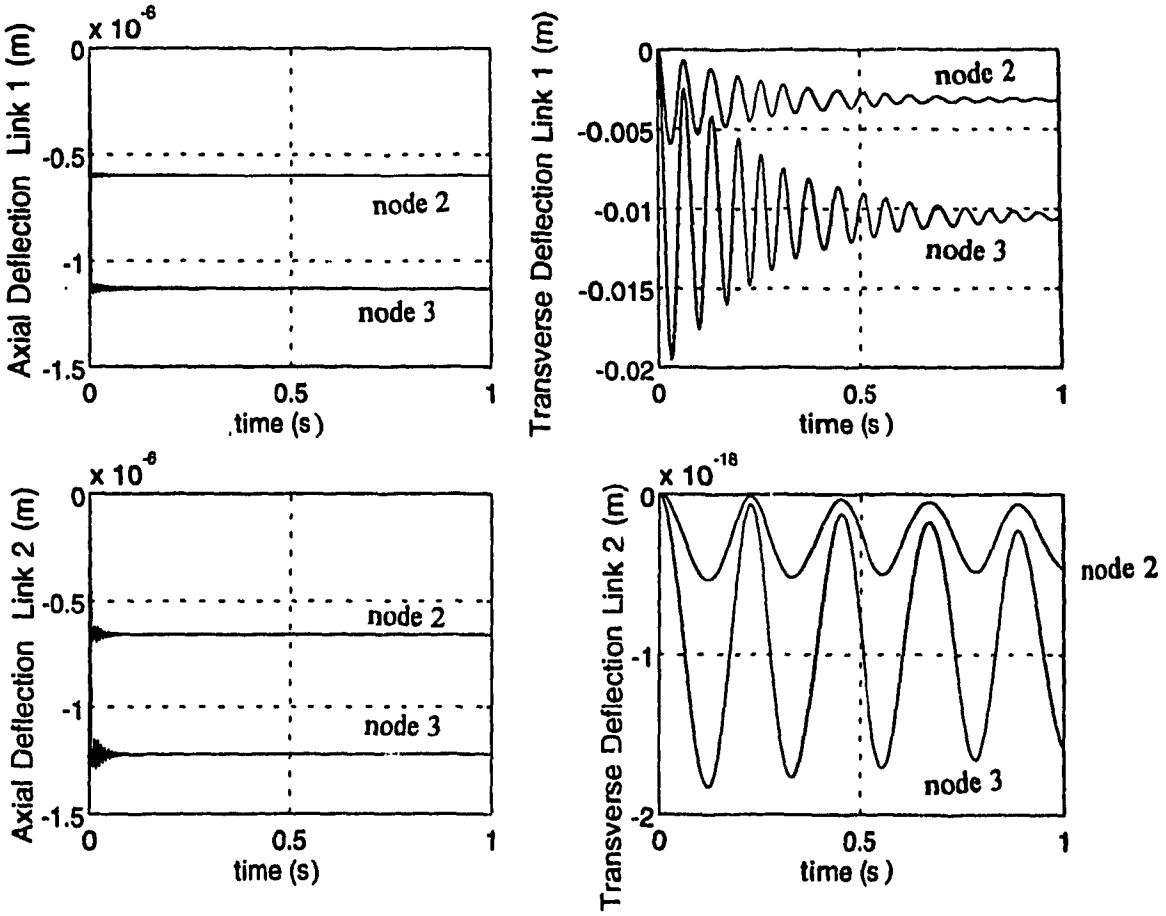

Figure 4.20. Axial and transverse deflections, step response, $b = h = 0.02$m, $m_p = 3$kg.

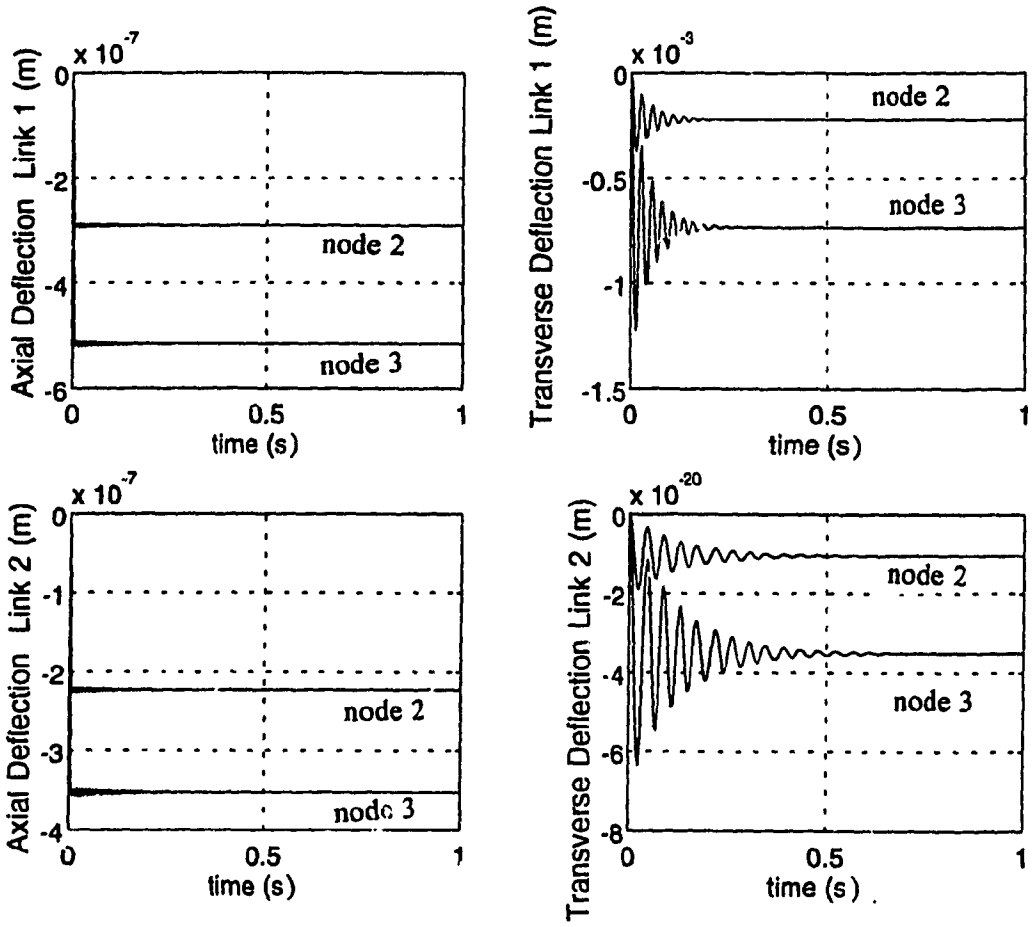

Figure 4.21. Axial and transverse deflections, step response, $b = h = 0.05$m, $m_p = 3$kg.

investigated. The cross section is a hollow square with outer size of 5 cm and an inner size of 4.8 cm. The thickness of the hollow section is 1 mm. In the Timoshenko shear relationship (equation 3.6), the shear coefficient, k depends on the shape of the link cross section [35]. This coefficient may be evaluated for a hollow rectangle with inner width and height, b_1 and h_1, and outer width and height, b_2 and h_2 as,

$$k=\frac{2(b_2h_2^3-b_1h_1^3)}{3h_1(b_2h_2^2-b_1h_1^2)}$$

The manipulator is loaded with a mass of 3 kg located at the end-effector. Subjecting this manipulator to the step trajectory, the corresponding driving torques, deflections and internal forces are shown in Figures 4.22, 4.23 and 4.24, respectively. Comparison to the manipulator with solid cross section of 5×5 cm is made referring to Figures 4.16, 4.19 and 4.21, respectively. Looking at the torques, some features may be observed. As the mass of the links is reduced significantly compared to the solid section, 0.53 kg as opposed to 6.8 kg, a lower frequency variation is prominent in the driving torque of link 2. It is reduced from 24 Hz for the solid cross section to 11 Hz for the hollow cross section indicating a much more flexible system.

Comparison of the hollow link deflections (Figure 4.23) to solid section link deflections (Figure 4.21) reveals that the hollow link manipulator undergoes slightly

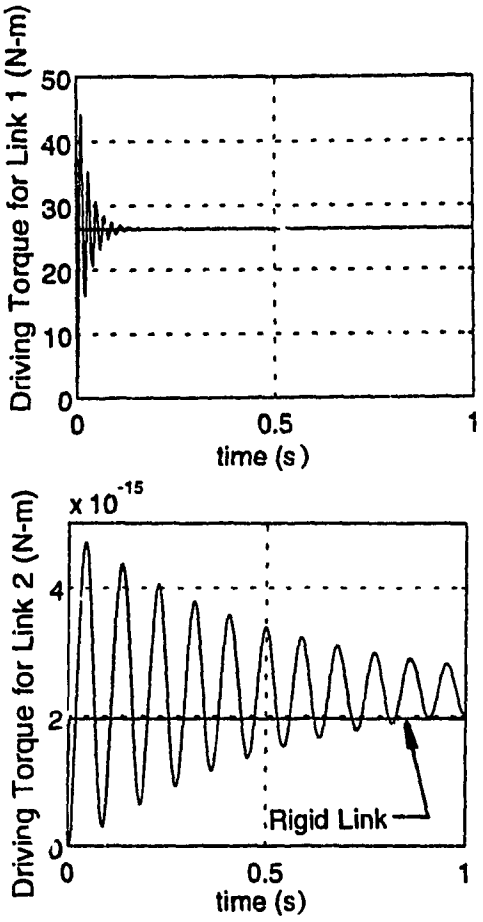

Figure 4.22. Driving torques for step response, hollow links.

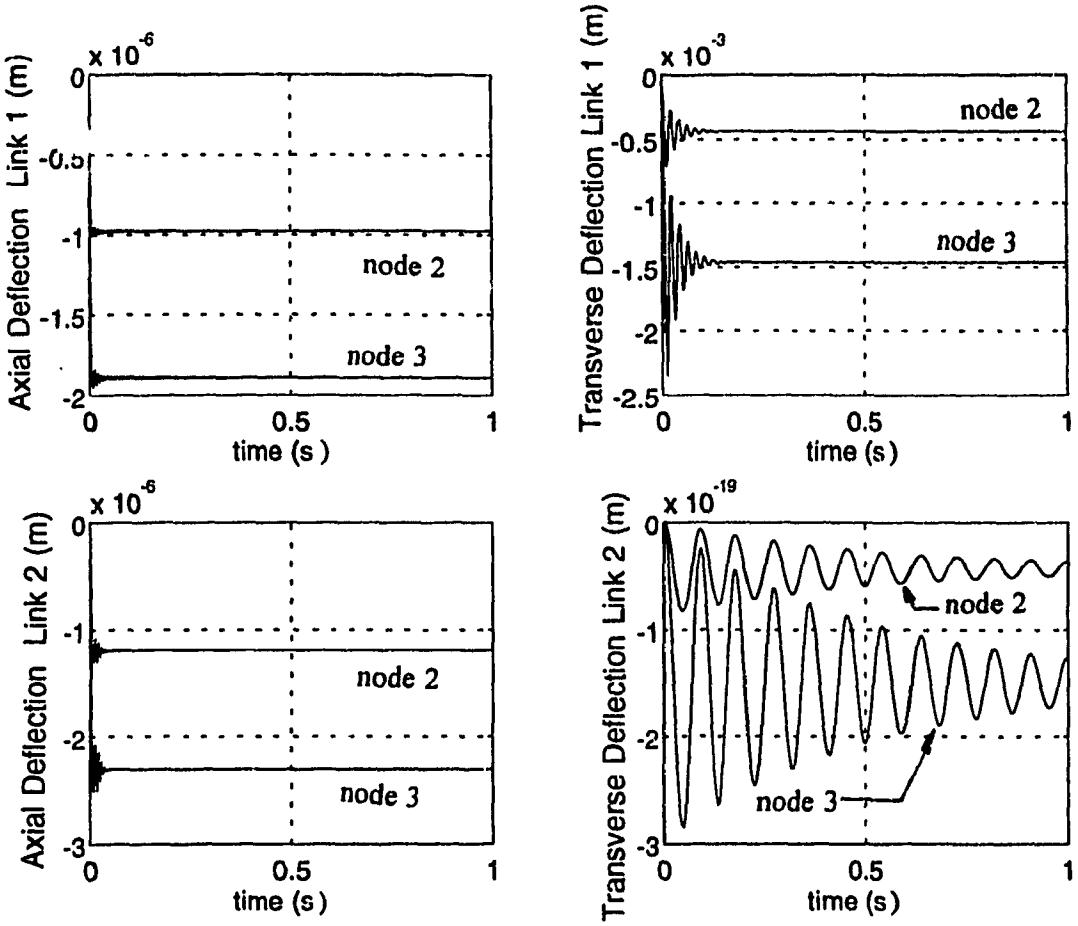

Figure 4.23. Axial and transverse deflections, step response, hollow links.

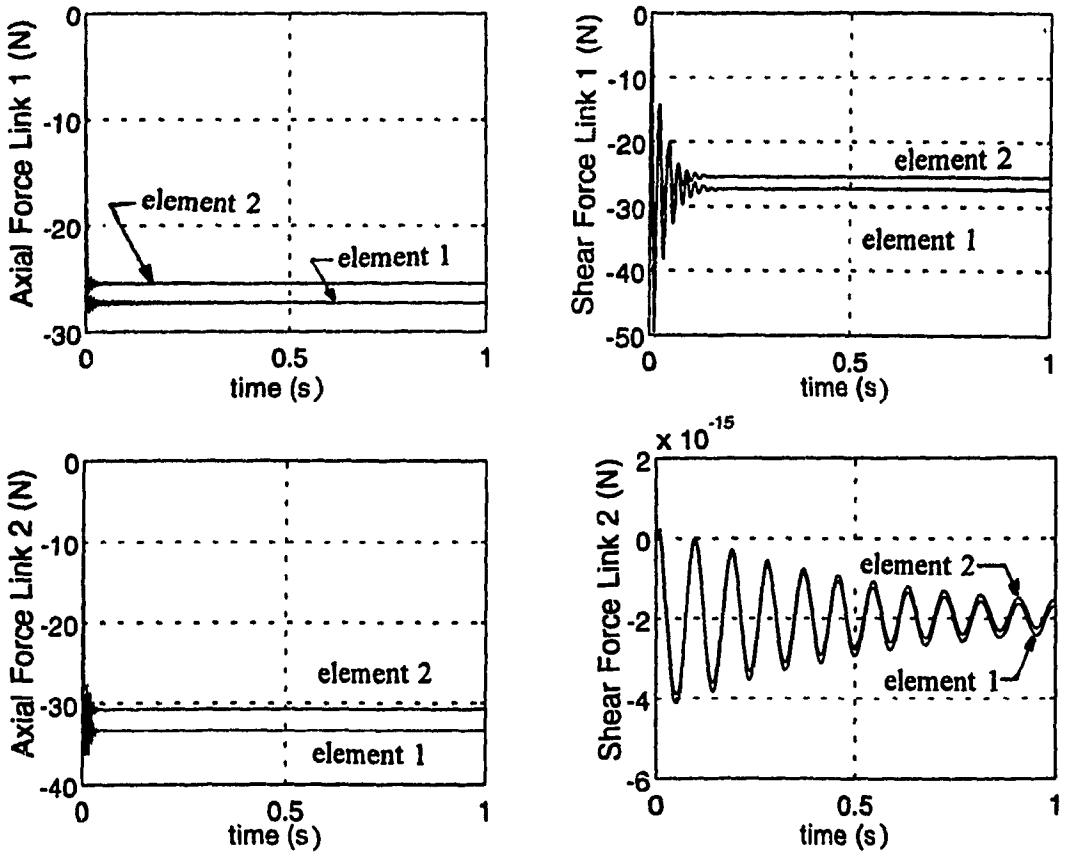

Figure 4.24. Axial and shear forces, step response, hollow links.

larger transverse deflections. The maximum deflection for the hollow link is 2.3 mm whereas the maximum deflection for the solid section approaches 1.2 mm. Also, an increased compression of both links 1 and 2 is evident as the links are hollow and therefore of reduced axial stiffness. As a consequence of the reduction in mass of the system, a significant change in internal forces for hollow links occurs. Comparison of Figure 4.24 to Figure 4.19 reveals this change. The effect of link mass on internal forces is minimal as compared to the contribution of the payload mass. In fact, the ratio of payload mass to manipulator mass has increased from 0.22 for the solid section to 2.8 for the hollow section. The effect of the hollow link is quite good considering the high ratio of payload mass to manipulator mass. It is hoped that the effects of deflections and oscillations on the manipulator performance may be compensated for through control techniques.

Nevertheless, attention should be payed to a shorter solid cross section links manipulator. Keeping the payload at 3 kg and reducing the links' length to 0.5 m may be beneficial. Figures 4.25 to 4.27 depict the joint driving torques, nodal deflections and internal forces of the manipulator as it is subjected to the step trajectory. The results have a trend similar to that of the results for hollow links (Figures 4.22 to 4.24). The difference is that the payload to manipulator mass ratio is 0.88, still smaller than 2.8 for the hollow section. The results indicate, as before, that payload effects are more pronounced for manipulators of reduced mass.

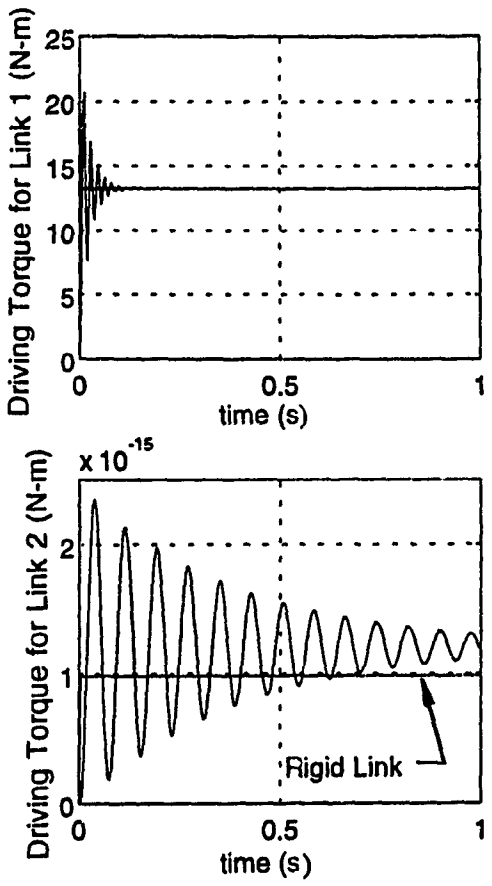

Figure 4.25. Driving torques for step response, $L_1 = L_2 = 0.5$m.

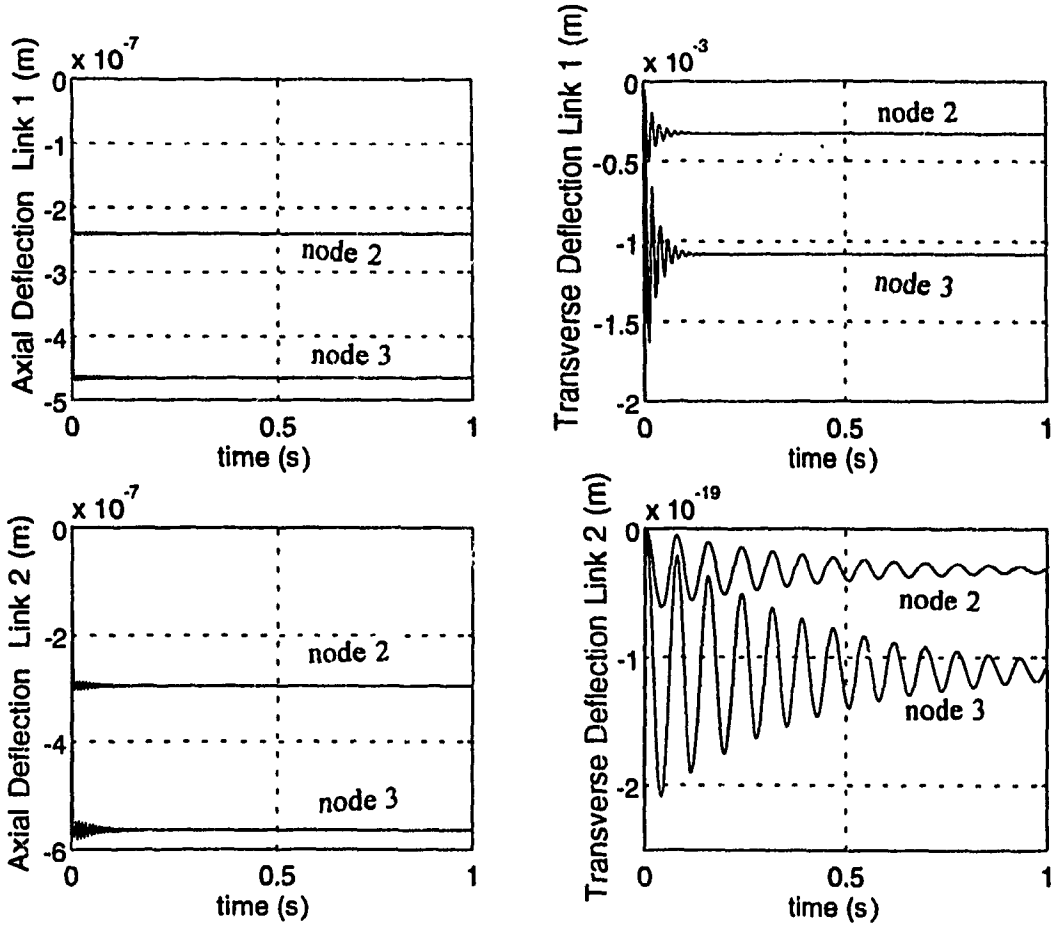

Figure 4.26. Axial and transverse deflections, step response, $L_1 = L_2 = 0.5$m.

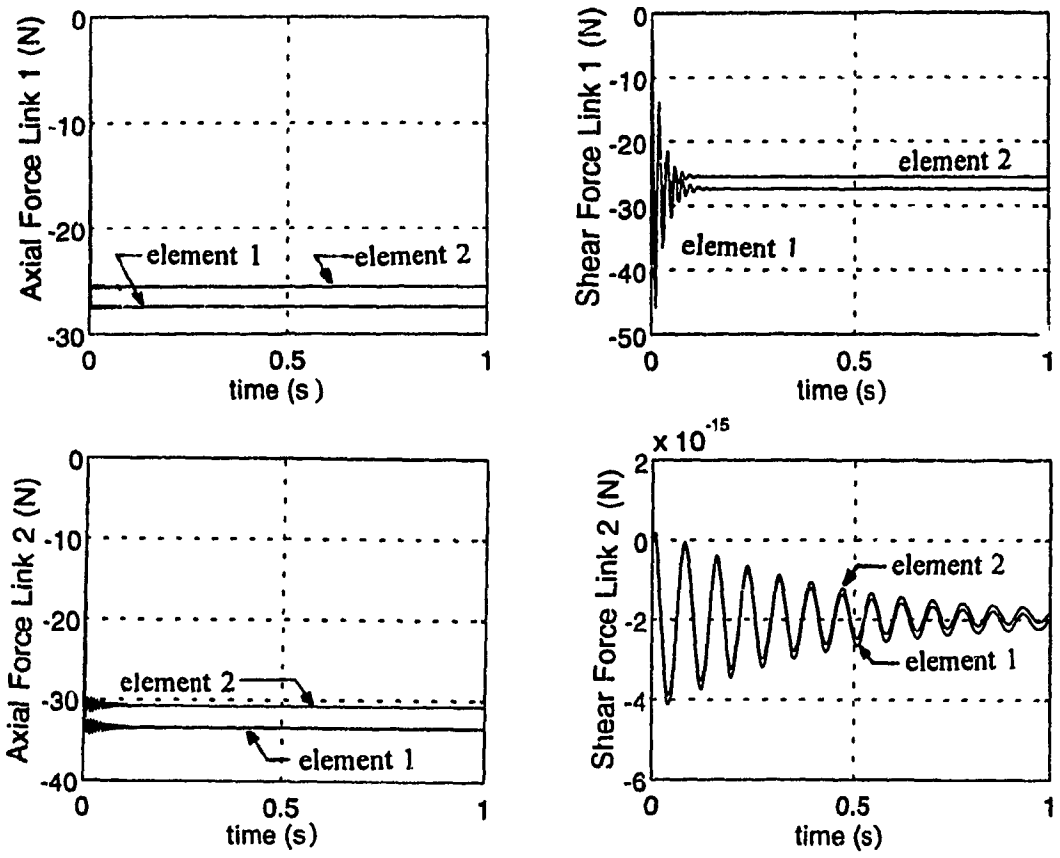

Figure 4.27. Axial and shear forces, step response, $L_1 = L_2 = 0.5$m.

4.2.3. Effect of Numerical Integration Parameters

To verify the effects on results caused by changes in the numerical integration parameters, Θ_1 and Θ_2, some results with changed values to these parameters are produced and compared to results obtained by using the original values of the parameters ($\Theta_1 = \Theta_2 = 0.7$). Two extremes are compared; minimum and maximum algorithmic damping have been used, that is, the "Newmark-like" parameters $\Theta_1 = \Theta_2 = 0.5$ and $\Theta_1 = \Theta_2 = 1.0$, respectively are tried. The results are obtained for a solid square cross section of dimension 0.02 m and length 0.5 m with a payload of 3 kg. The driving torques and the deflections in Figures 4.28 and 4.29 for the minimum damping are compared to those shown in Figures 4.30 and 4.31 for the maximum damping. Obtained for the undamped case the deflections exhibit high frequency oscillations and its amplitudes exhibit periodicity (Figure 4.29). This may be due to the fact that the numerical solution converges to a final solution as in Figure 4.26. Without damping, the solution is bounded by the extremes of these perturbations. The high frequency oscillations of the driving torque closely resemble those reported by Usoro et al [14].

4.3 Response to Cycloidal Trajectory

In this section, the manipulator arm follows a more practical type of motion, that is, a simple pick and place trajectory described by a cycloidal motion for convenience. Effects of a payload and its location relative to the end-effector of

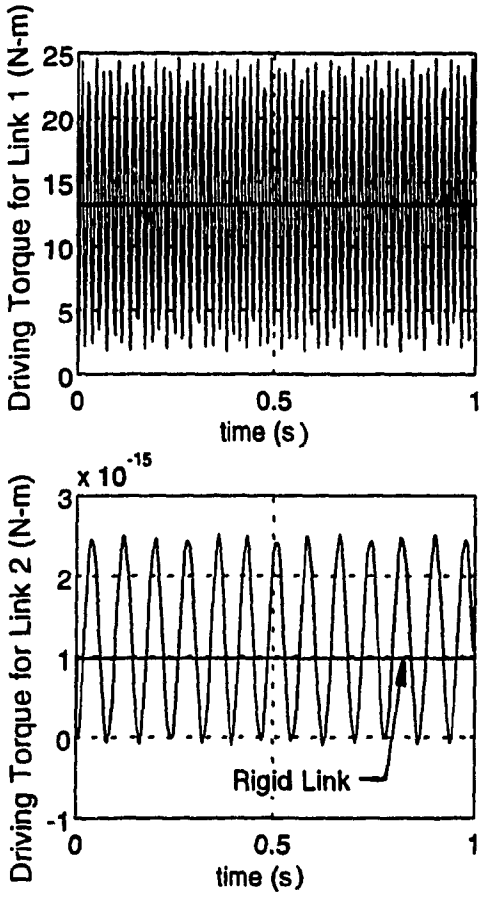

Figure 4.28. Driving torques for step response, minimum damping.

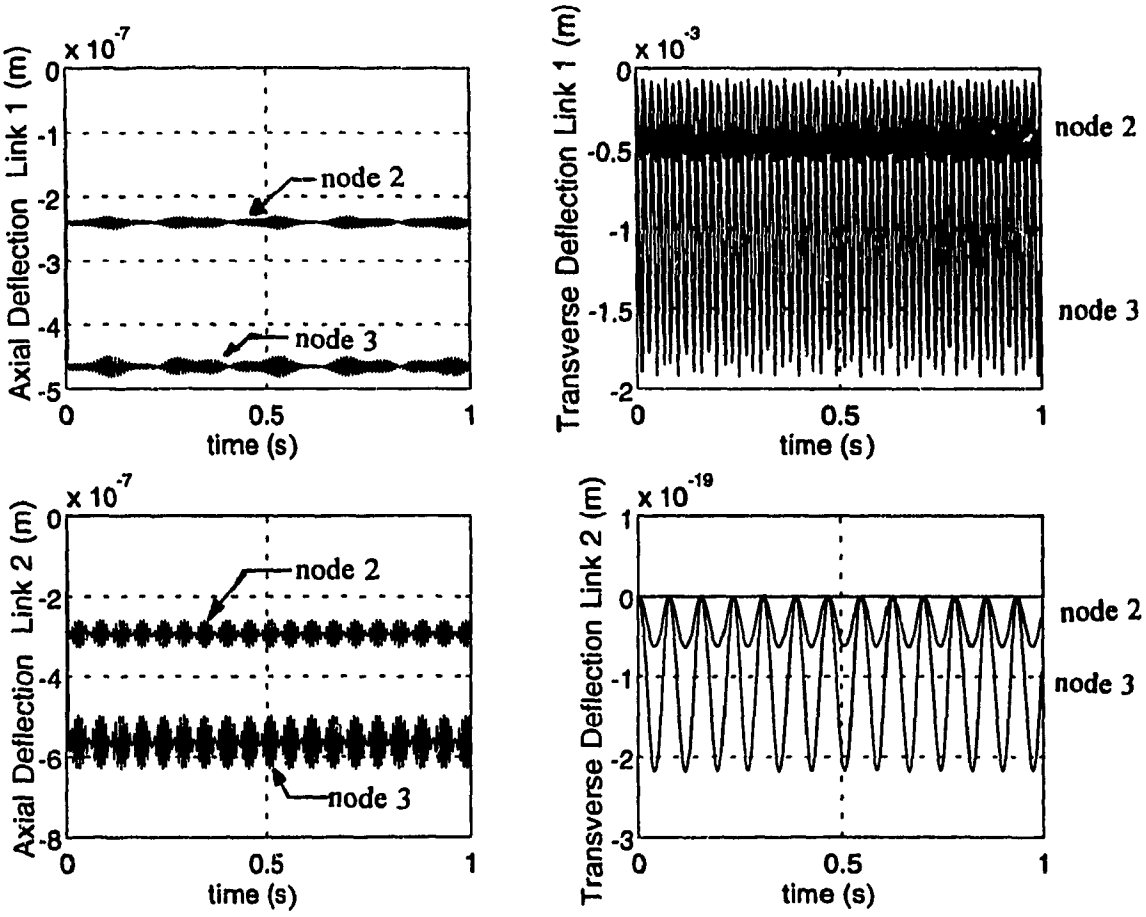

Figure 4.29. Axial and transverse deflections due to step response, minimum damping.

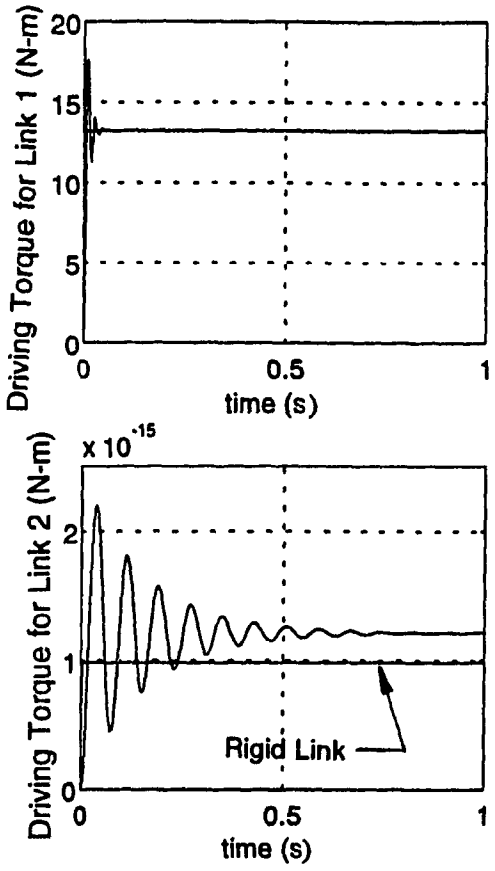

Figure 4.30. Driving torques for step response, maximum damping.

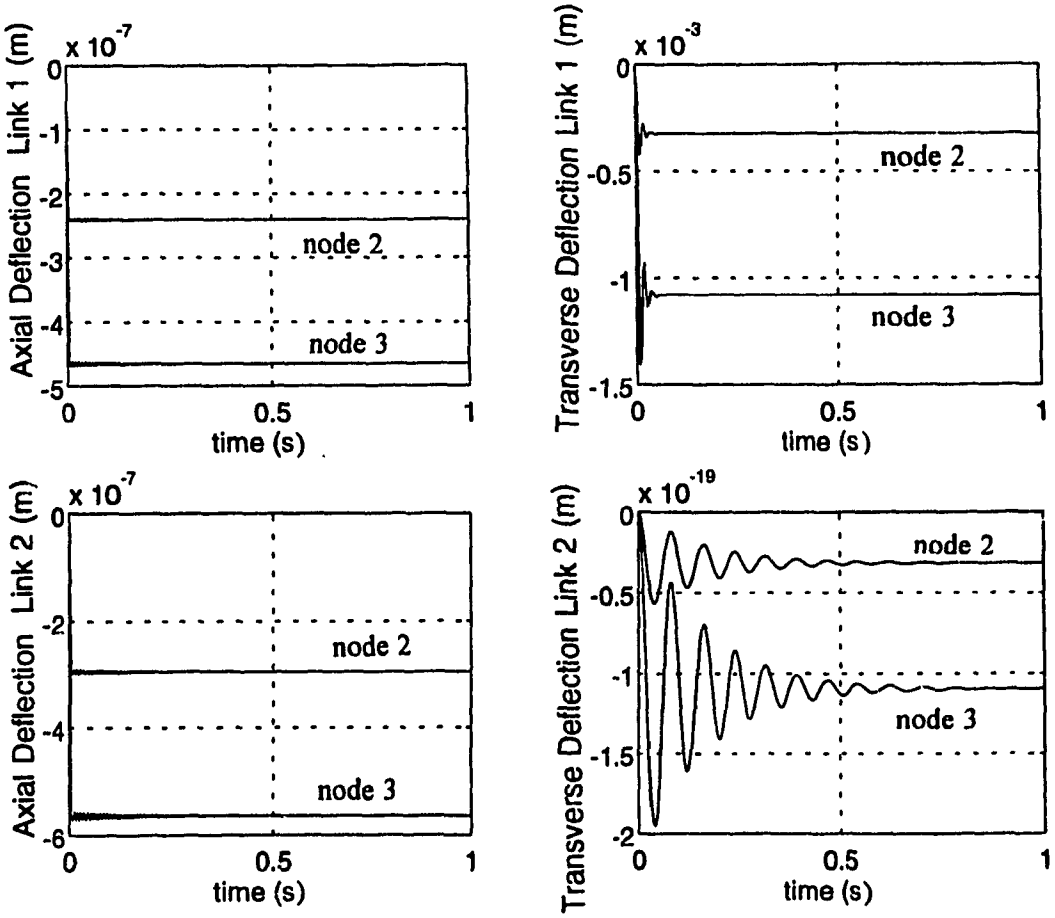

Figure 4.31. Axial and transverse deflections, step response, maximum damping.

the manipulator are investigated. As for the step response case, the effects of changing the "Newmark-like" parameters are observed too. In this section, more than in the previous, the focus is on payload capacity as determined by failure and stability criteria such as yielding and buckling.

4.3.1. Effect of Payload and Payload Arm

As stated in the previous section, a payload and its arm affect the manipulator in terms of frequency of response, decay time and internal forces in the links. Now, with a more adequate trajectory, the effect of the inertia of the payload can better be appreciated. Also, some limitations as the maximum load are observed. Again, a two-link manipulator with a uniform square cross section of 3 cm size and links' length of 1 m is selected for convenience. The initial, transitional and final positions of the manipulator are shown at steps of 0.02 s in Figure 4.32. The asterisk indicates position of the payload. The resulting driving torques, internal forces and nodal deflections for no payload are shown in Figures 4.33 to 4.36. Figure 4.33 illustrates the oscillations of the torques about the value for the rigid with a frequency of approximately 23 Hz. The numerical damping reduces the oscillations. As a consequence of the initial position of the manipulator, the gravity load acts as a step force input. Since initially the first link supports its own weight and that of the second link, its oscillations are more pronounced than those of the second link. The step moment due to gravity with respect to the second joint is

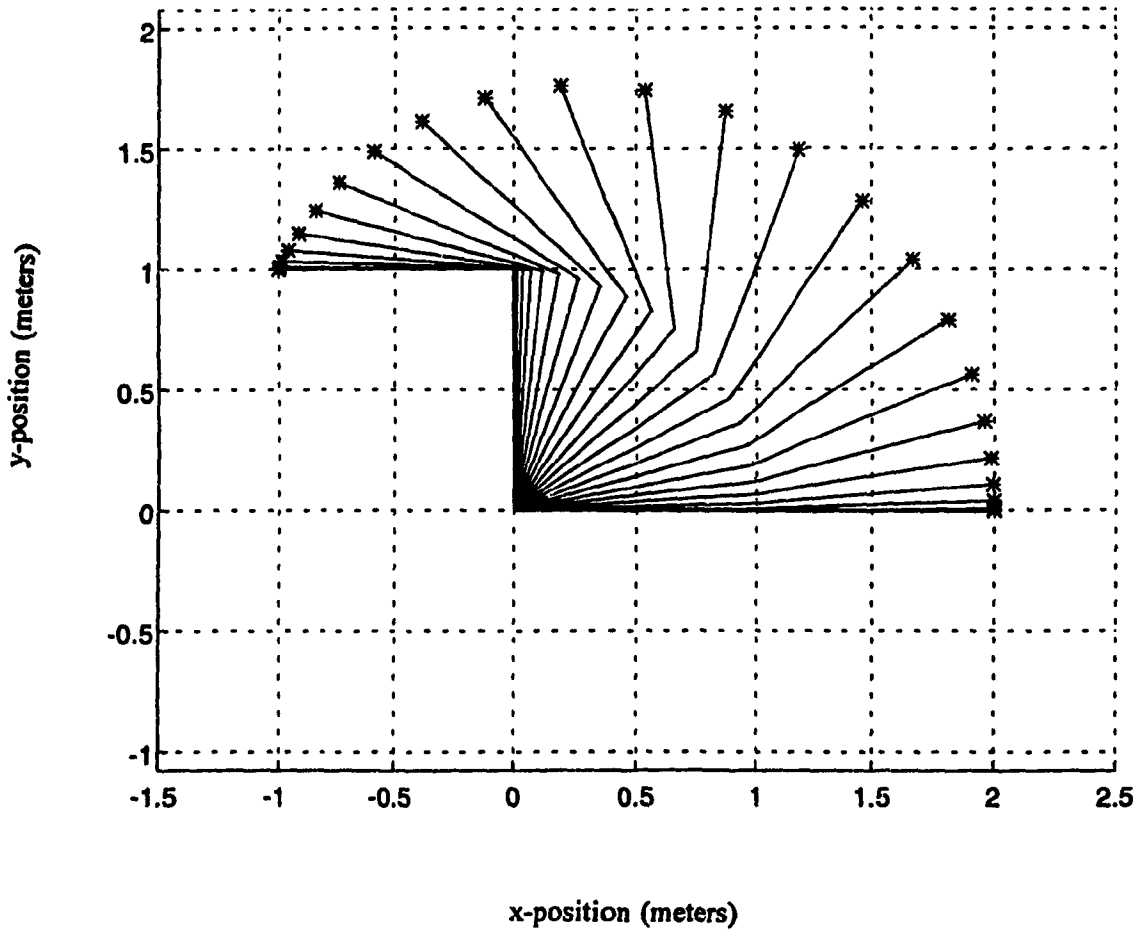

Figure 4.32. Initial, transitional, and final positions, cycloidal motion at 0.02 s steps.

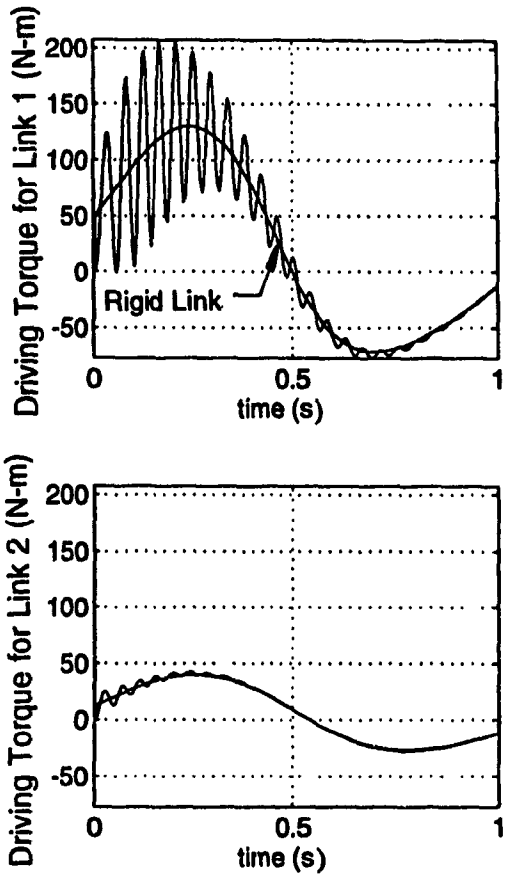

Figure 4.33. Driving torques for cycloidal motion, $b = h = 0.03$m.

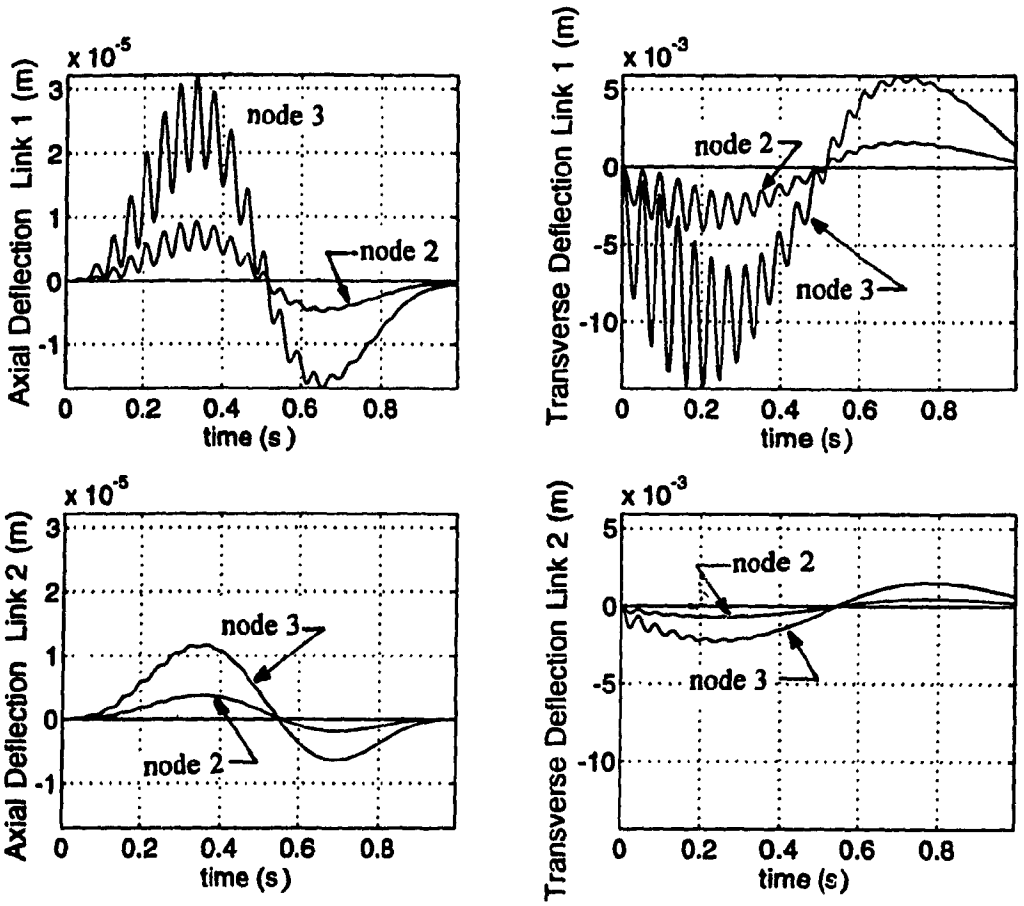

Figure 4.34. Axial and transverse deflections, cycloidal motion, $b = h = 0.03$m.

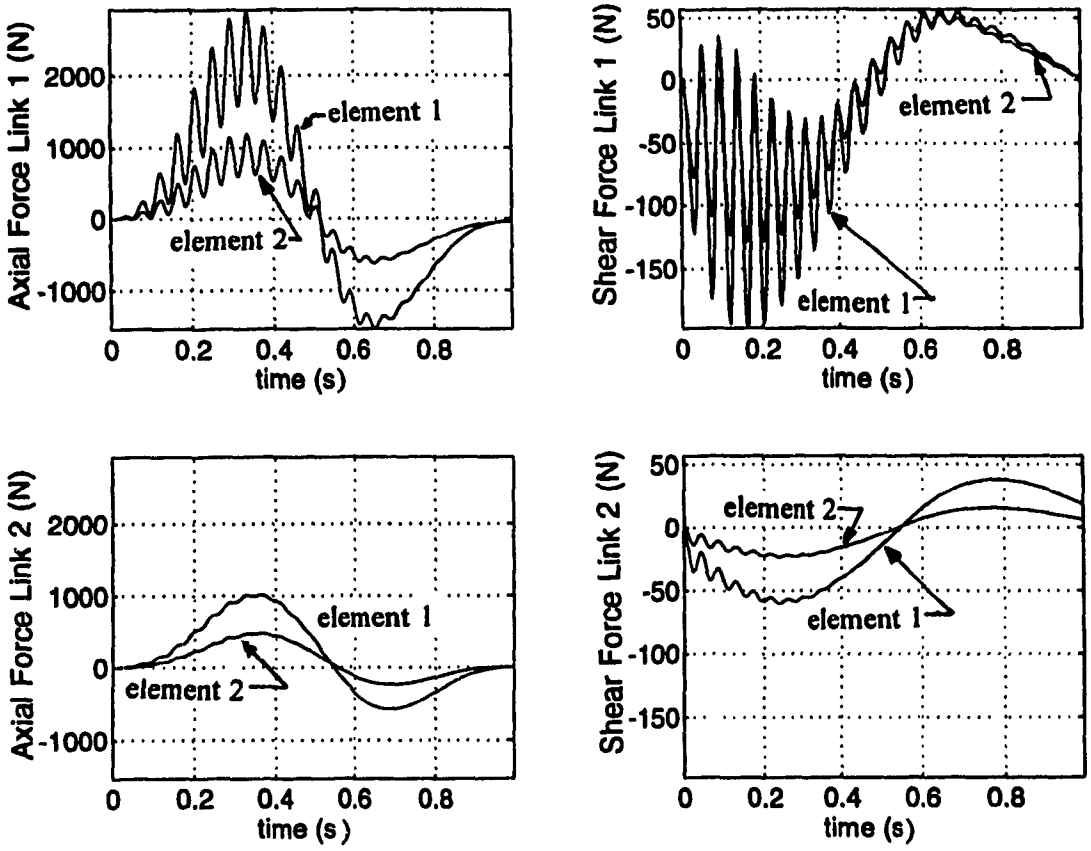

Figure 4.35. Axial and shear forces, cycloidal motion, $b = h = 0.03$m.

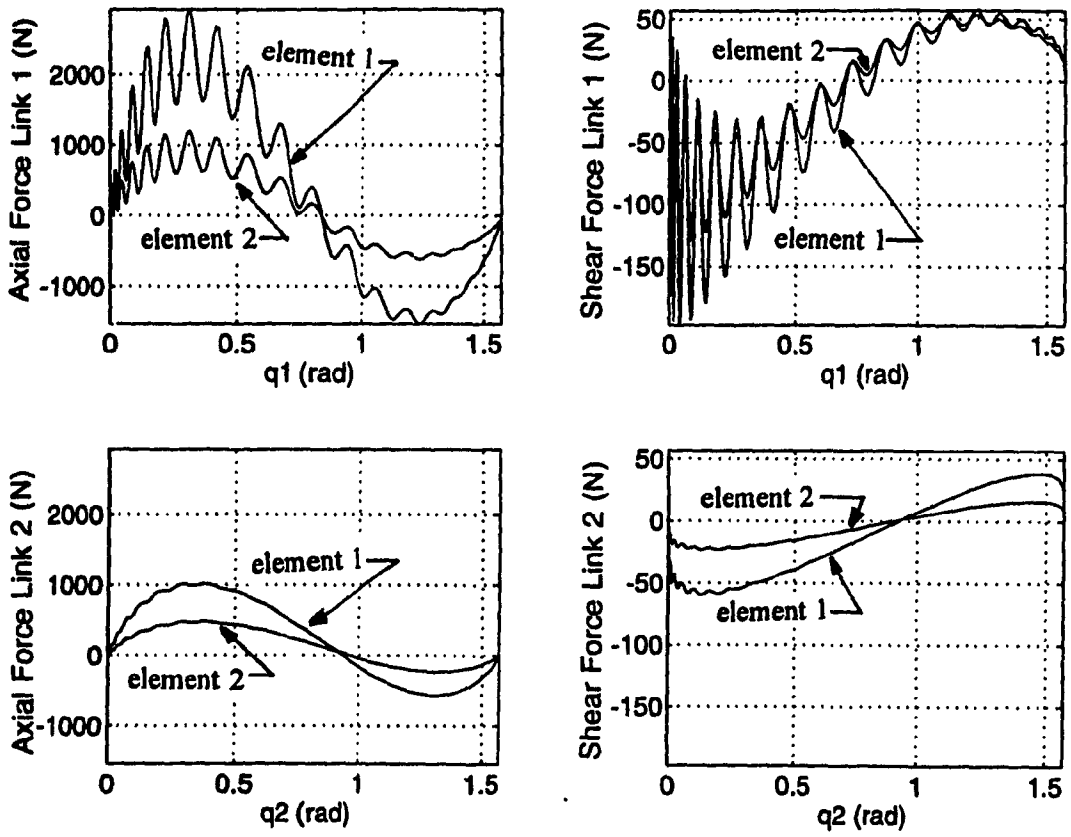

Figure 4.36. Axial and shear forces, cycloidal motion (versus position), $b = h =$ 0.03m

12.0 N-m while the initial moment with respect to the first joint is 47.9 N-m. With the rigid body kinematic constraints imposed on the end-points of each link, the trajectory is followed with low deflections as shown in Figure 4.34. Here, the maximum deflection is 15 mm for the first link and approximately 2.5 mm for the second link. Figure 4.35 reveals that the first element of each link supports the greater loads and in turn exhibits the higher amplitude oscillations. Furthermore, the shear distribution along the first link is relatively constant demonstrating that the element inertia in the transverse direction is negligible compared to that of the second link. The base of the link supports almost double the axial and shear loads as compared to the second link. The base link must be designed accordingly to support these transmitted loads. In brief, Figure 4.36 illustrates the internal forces with respect to the angular positions of the links. The location of the maximum magnitude of forces within the trajectory is shown. These maxima occur at the beginning of the trajectory as the initial gravity loads and inertia loads are overcome, and towards the end of the trajectory where the large loads are due to deceleration.

Figures 4.37 and 4.38 show the criteria due to which failure may occur. Figure 4.37 compares the critical load for buckling for the links of 3 cm square cross section to the axial forces within the first link. By an eigenvalue analysis, the critical load for this beam-column is found to be 1.2×10^4 N [32]. As illustrated, the axial forces are well within the limits of the compressive critical

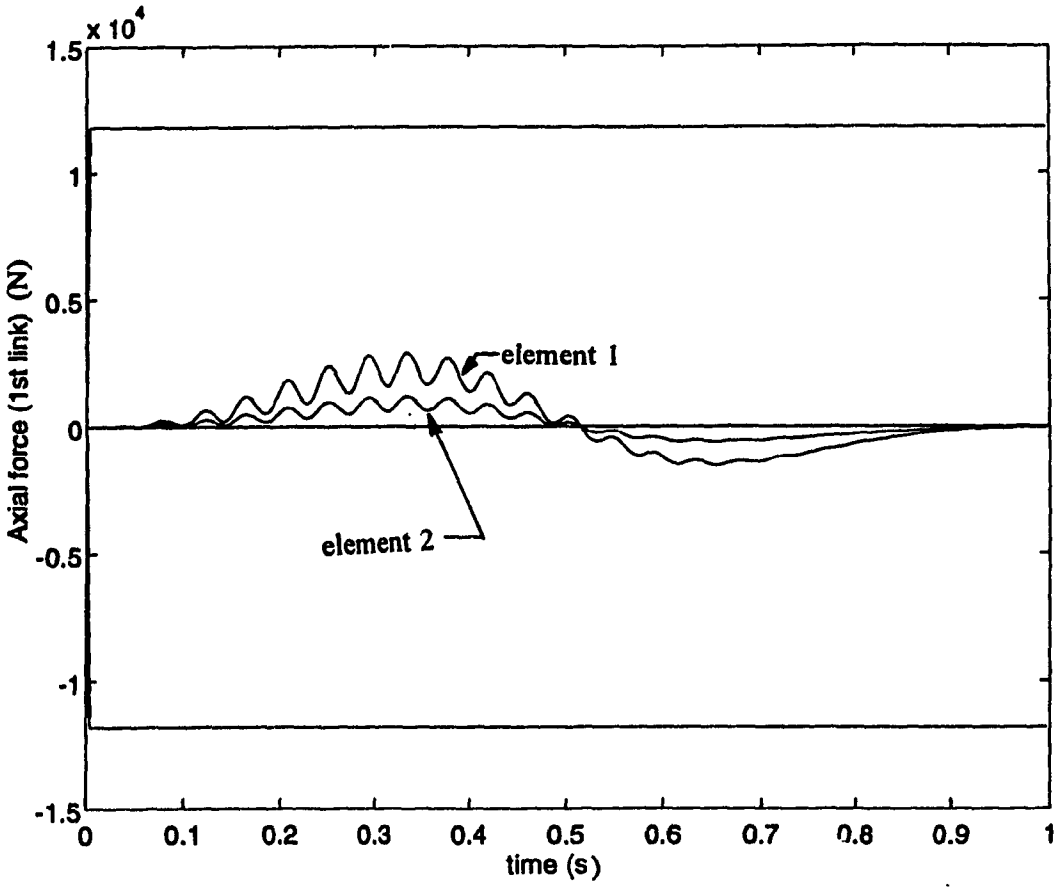

Figure 4.37. Comparison of axial force and critical load, $b = h = 0.03$m.

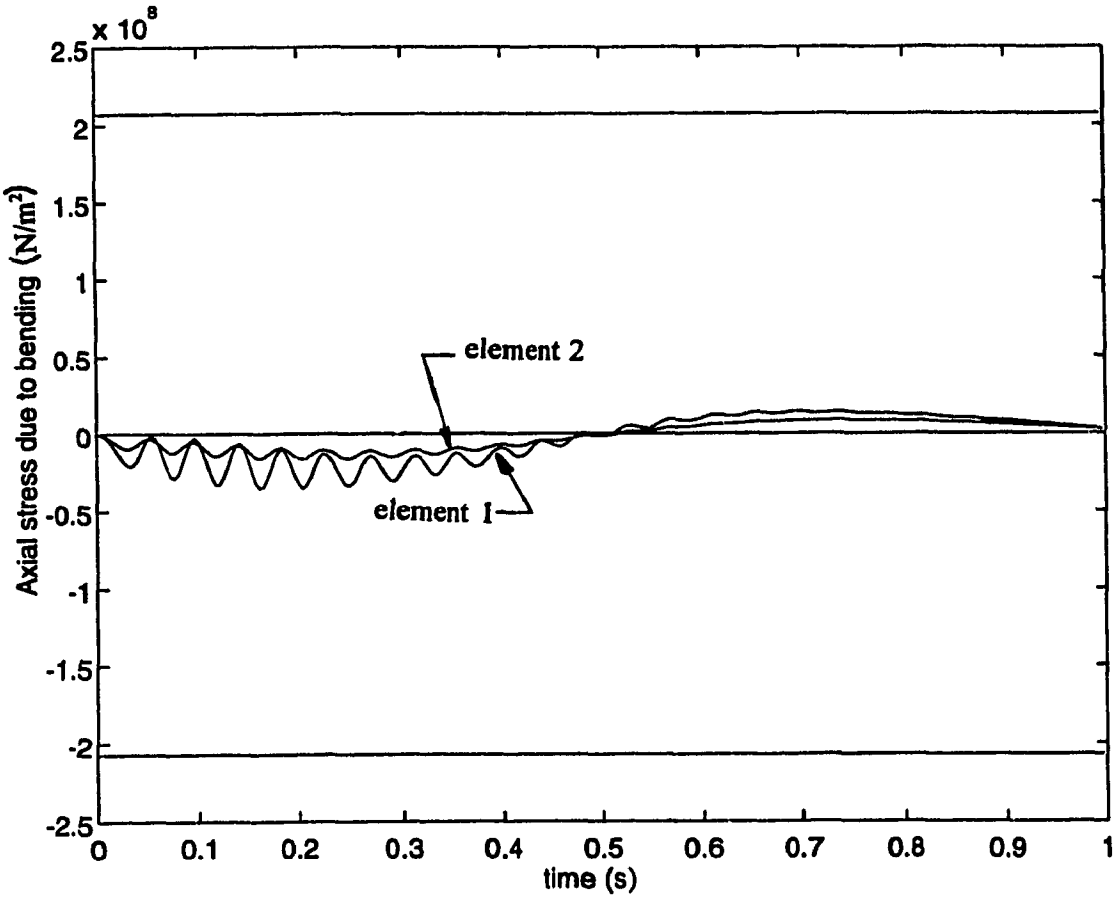

Figure 4.38. Comparison of yield strength and axial stress in bending, $b = h = 0.03$m.

load (the negative constant line). The positive horizontal line is plotted for convenience so that the graph appears visually symmetric. Figure 4.38 compares the axial stress to the yield strength, 2.1×10^8 N/m^2 for Aluminum [34]. Again, the stresses are well within the imposed limits. Both limits are plotted since axial stress due to bending is symmetric about the axis of the link. These plots will prove useful to determine the maximum payload for the given trajectory.

After several executions of the program and verifications of the critical buckling and yield loads, the maximum payload the present manipulator can carry through the given trajectory is found to be approximately 6.7 kg. The critical buckling load was the limiting criteria in this case. The driving torques, internal forces, and deflections are plotted in Figures 4.39, 4.40 and 4.41. Comparisons are made to the corresponding plots in Figures 4.33 to 4.35 for the case of no payload. In general, nominal values of torques, deflections, and internal forces have increased in magnitude. For example, the torque at the base joint increased from close to 130 N-m to 600 N-m, the maximum deflection is just over 7.5 cm compared to 1.5 cm in Figure 4.34, and the maximum magnitudes of the axial and shear forces are near 1.5×10^4 N and 400 N respectively. Hence, the payload effectively increased the inertia of the system. Turning to the oscillations of Figure 4.39, the high frequency disturbance in the curve of the first link's torque is due to the initial gravitational loads. This perturbation is of small magnitude compared to the lower frequency oscillations which are prominent. In Figure 4.39, the

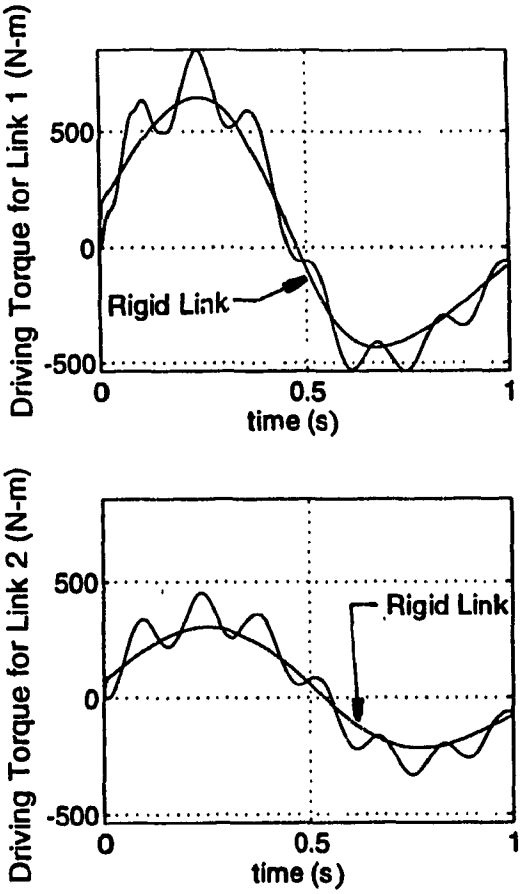

Figure 4.39. Driving torques for cycloidal motion, m_p = 6.7 kg.

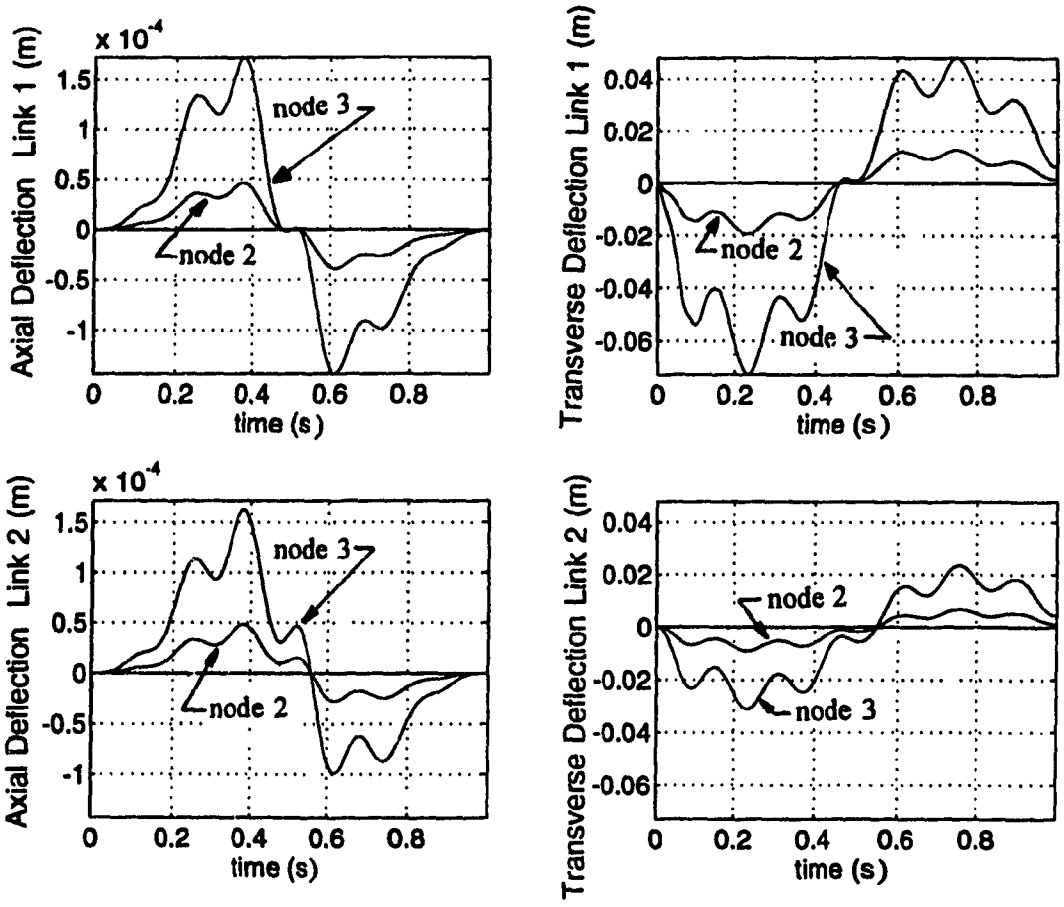

Figure 4.40. Axial and transverse deflections, cycloidal motion, m_p = 6.7 kg.

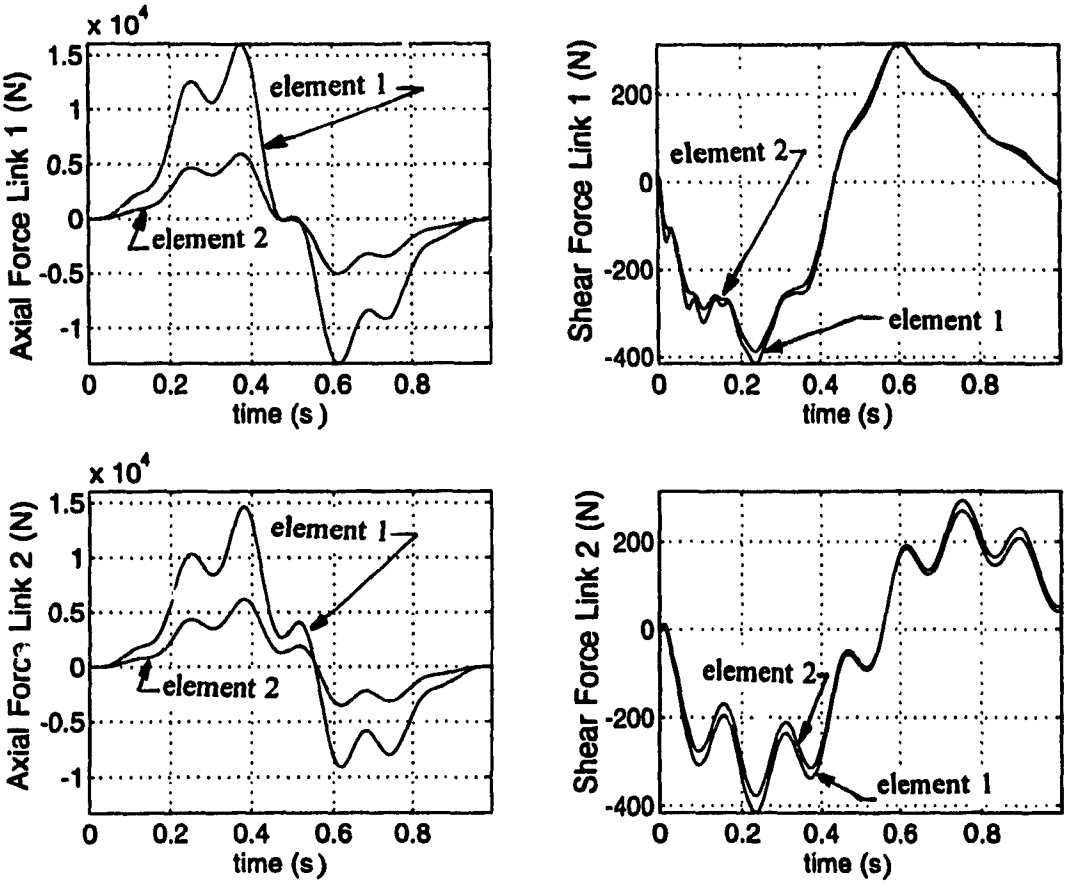

Figure 4.41. Axial and shear forces, cycloidal motion, m_p = 6.7 kg.

payload's inertia dominates in the oscillatory magnitude of the results. The frequency of oscillations have decreased from 24 Hz to 6.5 Hz. The decreased frequency of oscillations is a result of the decrease in stiffness of the system relative to the payload.

Consider the same manipulator, but with the payload displaced with respect to the end effector. Two cases are studied. First, the payload remains horizontally displaced from the end-effector throughout the trajectory, and second, the payload is displaced at a constant distance in the direction of the outermost link (link 2). The offsetting of the payload or arm, r_p is 0.4 m. Again, by repeated computations, the maximum payload capacity, with respect to the critical buckling load, for the first case is approximately 6.5 kg and for the second case, it is approximately 5.5 kg. The payload arm introduces an increase in inertia. Driving torques, internal forces and deflections are shown from Figure 4.42 to Figure 4.47 for both cases. The initial response for both cases is identical due to the initial conditions in which the horizontal orientation of the payload from the end effector is identical for both cases. The similarity between the two cases is significant the first 0.4 s to 0.5 s of the trajectory. The magnitudes of the nominal values and frequency of oscillations closely correspond. The frequency is approximately 5.0 Hz to 5.5 Hz, which is 1 Hz lower than it was observed for the payload with no offset in Figure 4.39. With a payload offset, the links are more susceptible to deflections as the overall stiffness of the system decreases as reflected in the reduction of frequency

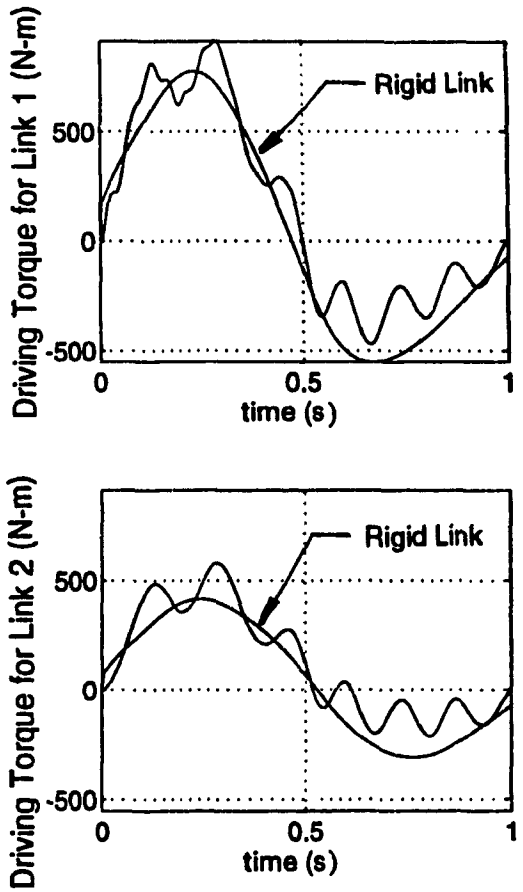

Figure 4.42. Driving torques for cycloidal motion, horizontal payload, m_p=6.5 kg.

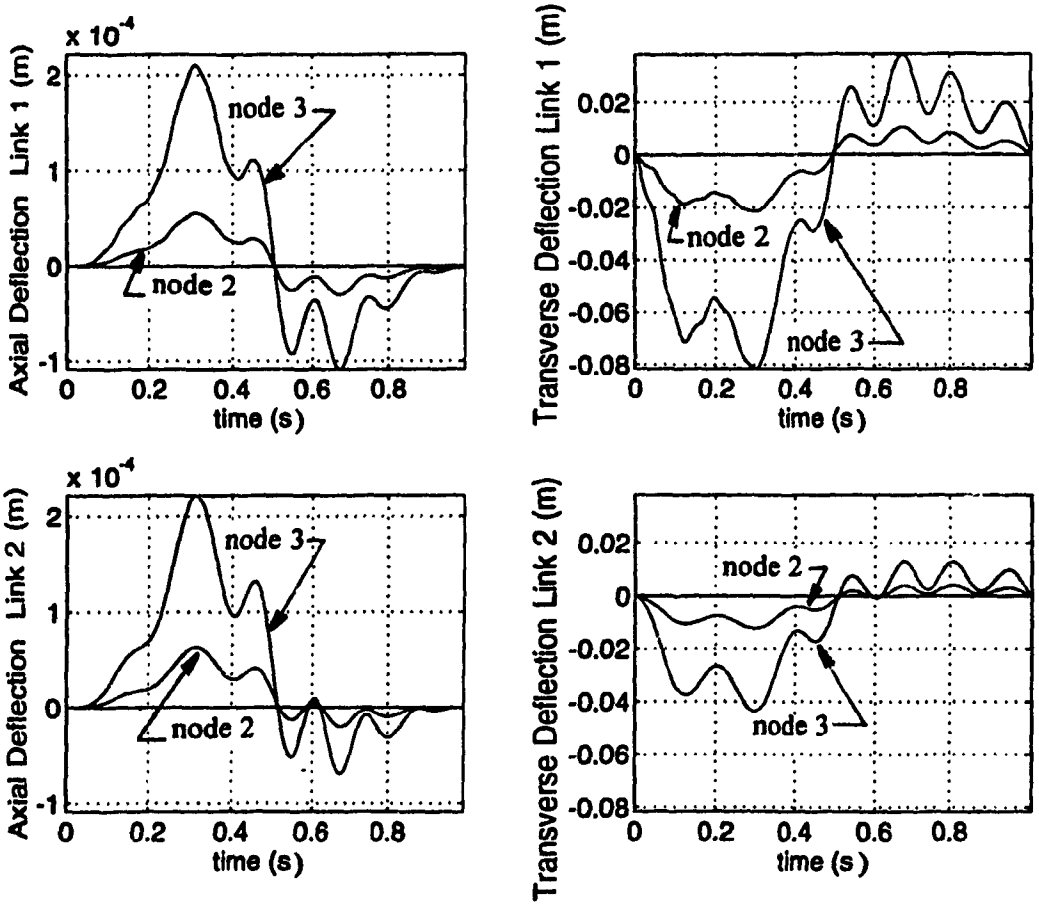

Figure 4.43. Axial and Transverse Deflections, Cycloidal Motion, horizontal payload, b=h=0.03m.

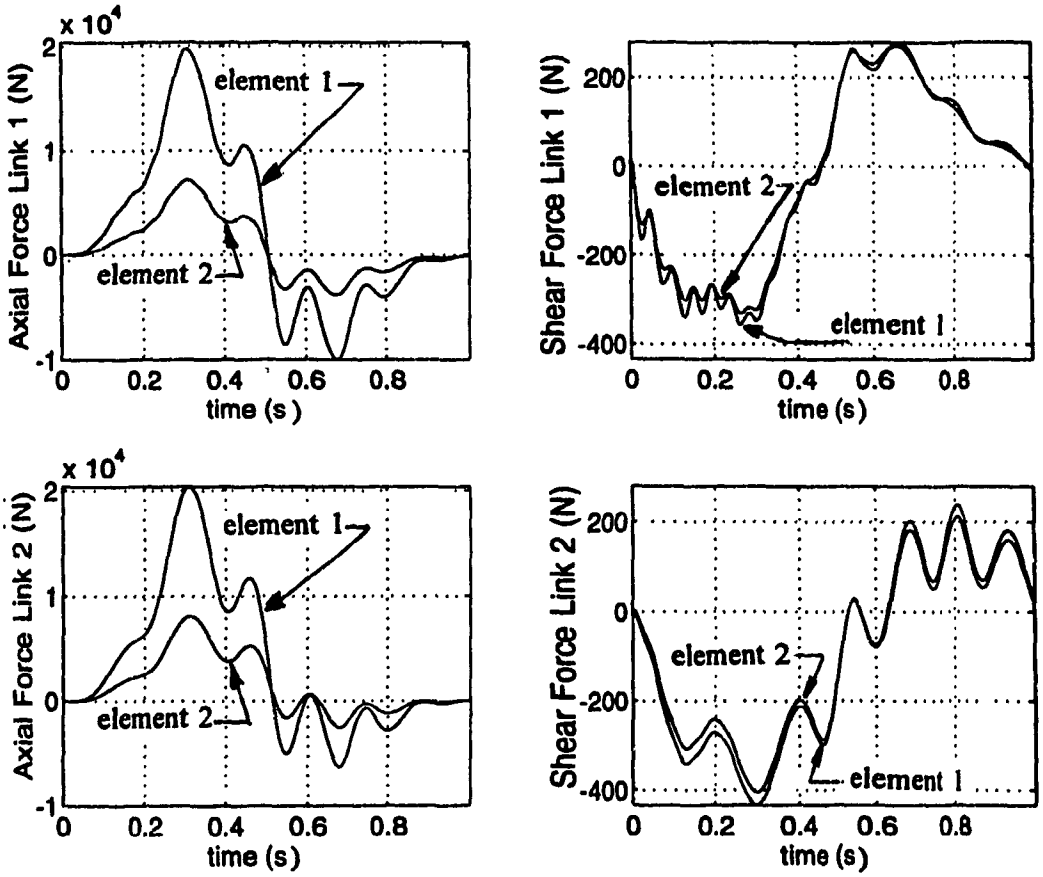

Figure 4.44. Axial and Shear Forces, Cycloidal Motion, horizontal payload, b=h=0.03m.

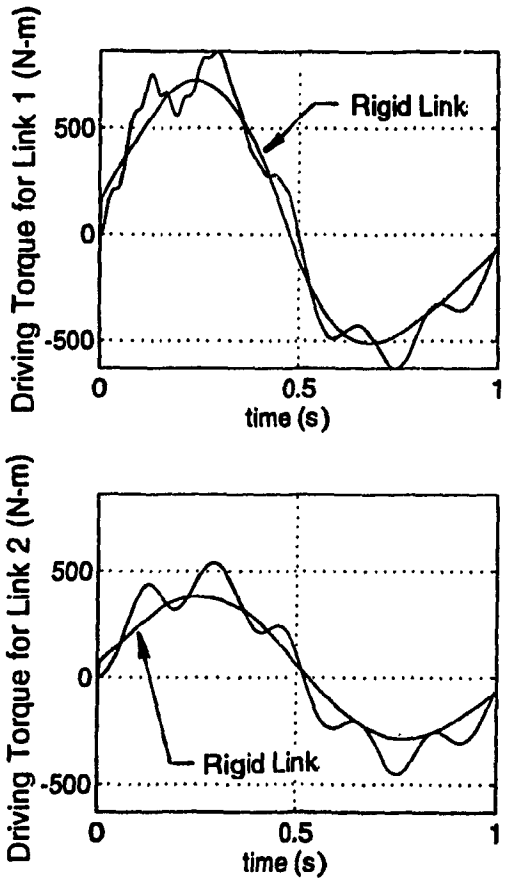

Figure 4.45. Driving torques for cycloidal motion, extended payload, b=h=0.03m.

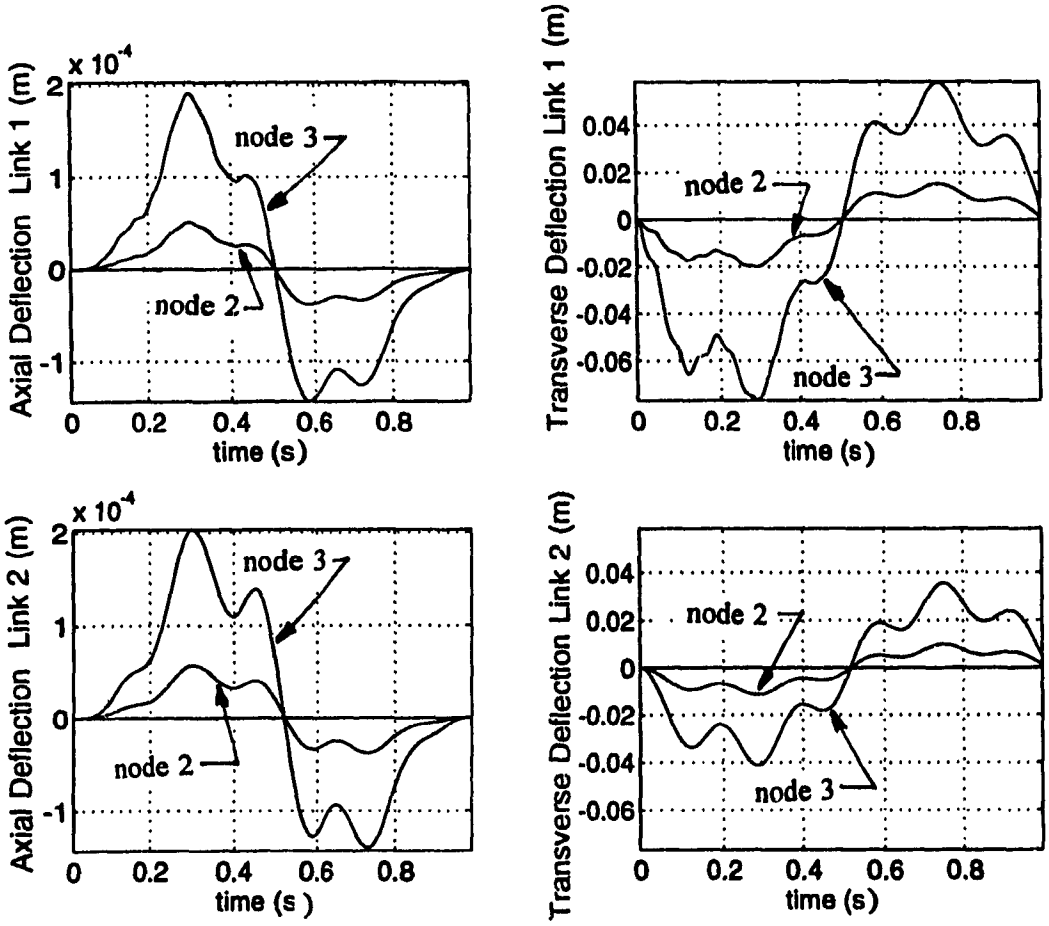

Figure 4.46. Axial and transverse deflections, cycloidal motion, extended payload b=h=0.03m.

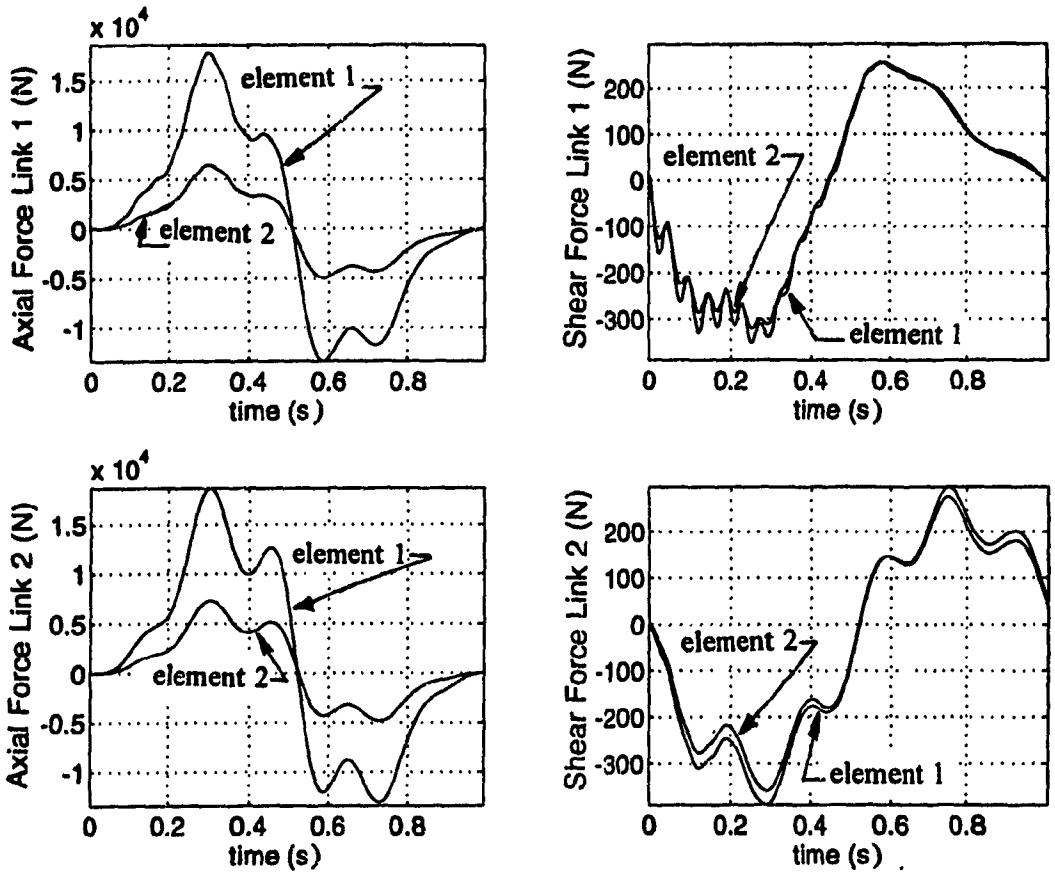

Figure 4.47. Axial and shear forces, cycloidal motion, extended payload, b=h=0.03m.

of the response.

Figures 4.48 and 4.49 indicate the trajectory of the payloads for the two cases. Both depict similar features at the beginning of the trajectory. A so called sling-shot effect can be observed. As the driving torques are applied, a bending action in the links occurs due to an action-reaction phenomenon before the links commence their trajectory. The payload for the first case approaches the base joint as the manipulator moves through its trajectory. The frequency of oscillations increases gradually from 5 Hz to 8 Hz within the motion. This occurs as the payload folds in toward the second link (Figure 4.48). On the other hand, the dynamics for the second case increase since the payload is further from the base (Figure 4.49) compared to the first case.

4.3.2. Effect of Manipulator Links' Dimensions

When the manipulator dimensions vary, the payload carrying capacity is affected. An increase in the cross section size of the manipulator links from 3 cm to 5 cm is investigated. The maximum payload for this manipulator is found to be about 50 kg according to the yield criteria of failure. This is about ten times that of the manipulator with cross section of 3 cm square. Graphically, the driving torques, internal forces and deflections shown in Figures 4.50, 4.51, and 4.52 depict, generally, an increased rigidity. The most prominent characteristic is that the order of the shear forces (Figure 4.52) is closer to that of the axial forces, indicating a

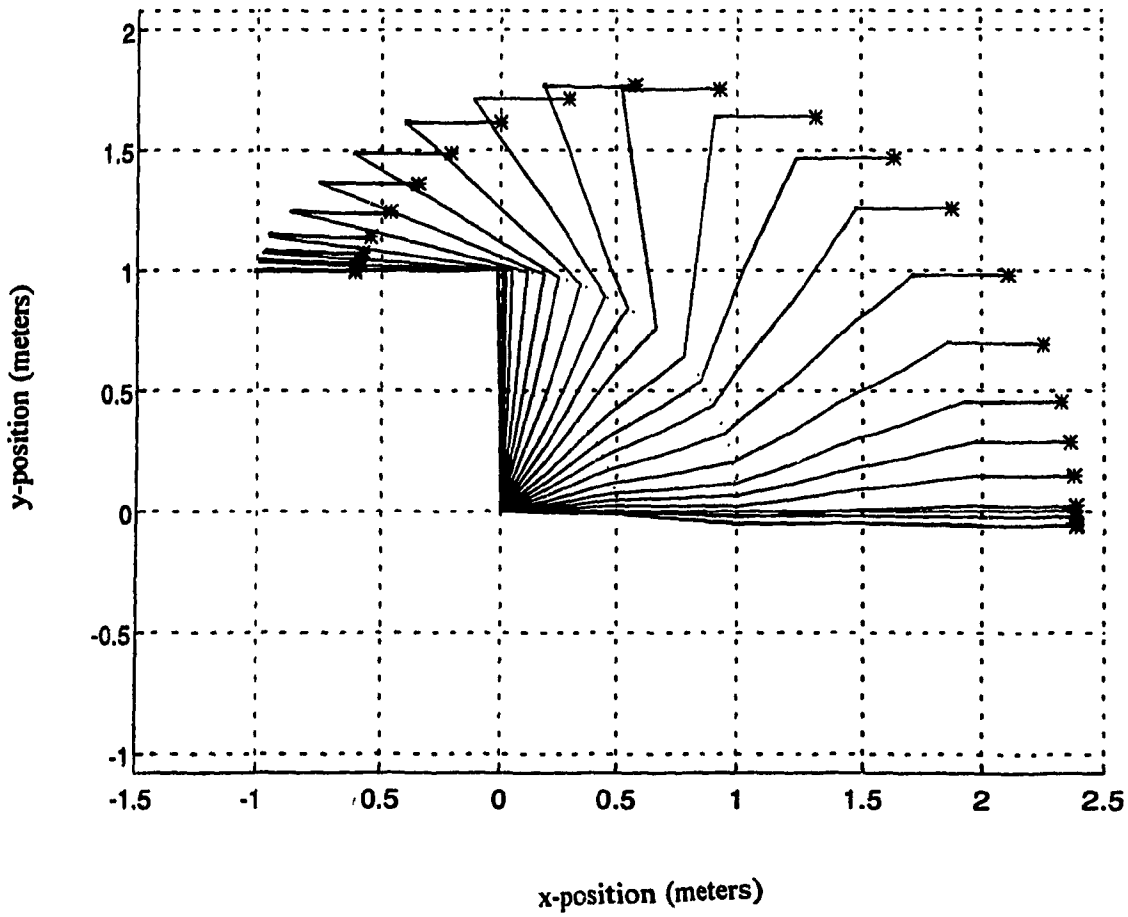

Figure 4.48. Motion for horizontal payload case.

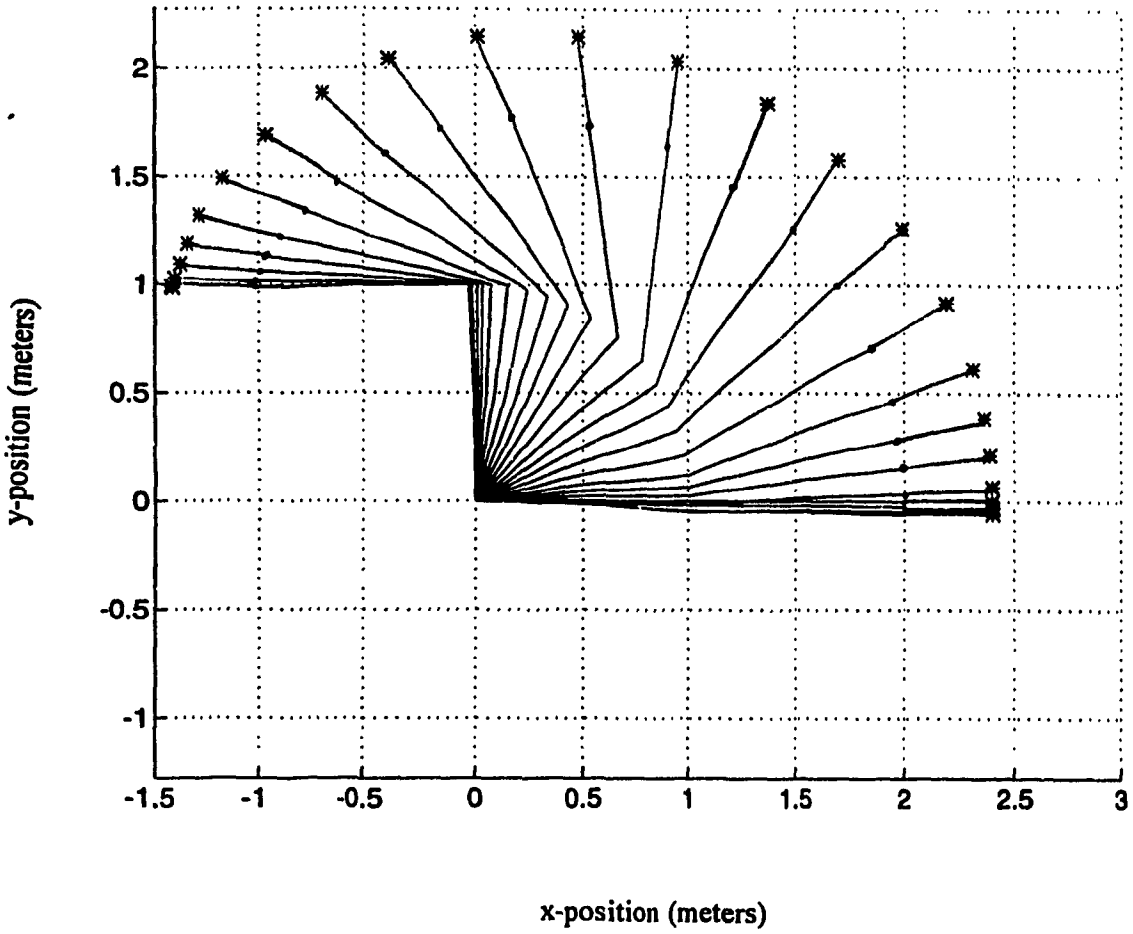

Figure 4.49. Motion for extended payload case.

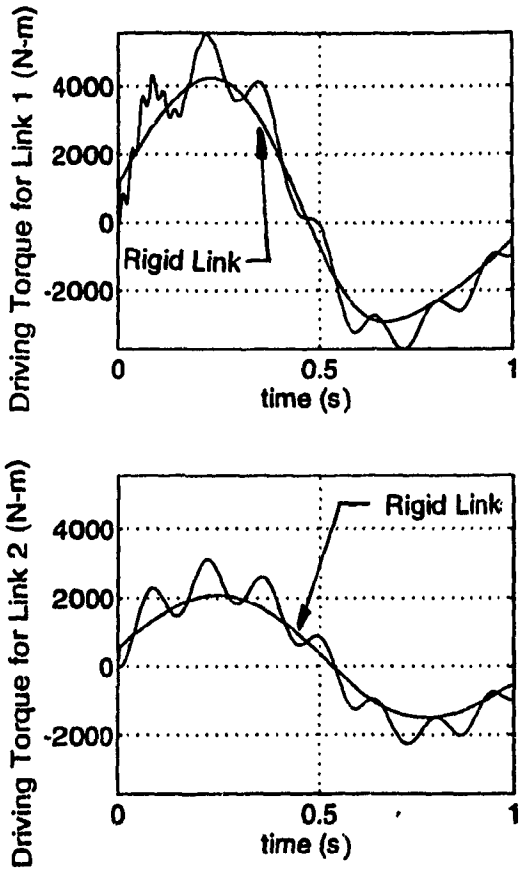

Figure 4.50. Driving torques for cycloidal response, $b = h = 0.05$ m, $m_p = 50$ kg.

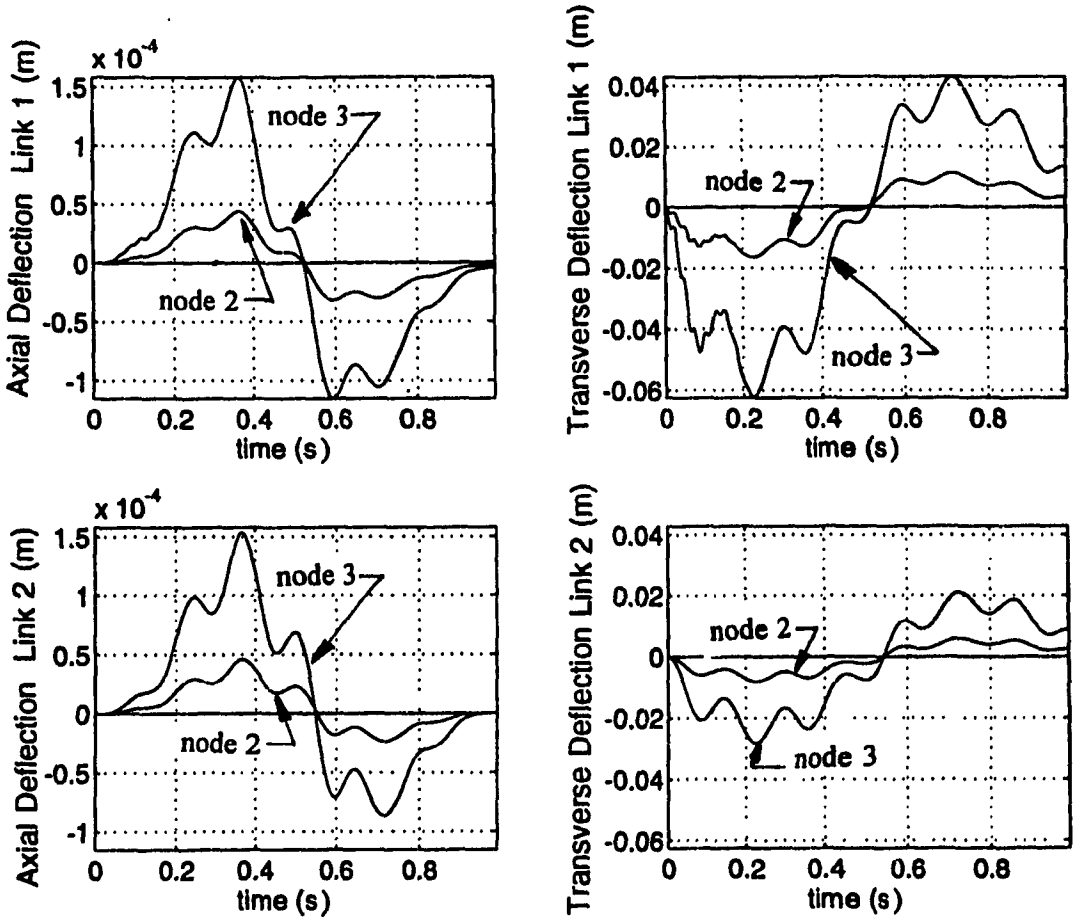

Figure 4.51. Axial and transverse deflections, cycloidal motion, $b = h = 0.05$ m, $m_p = 50$ kg.

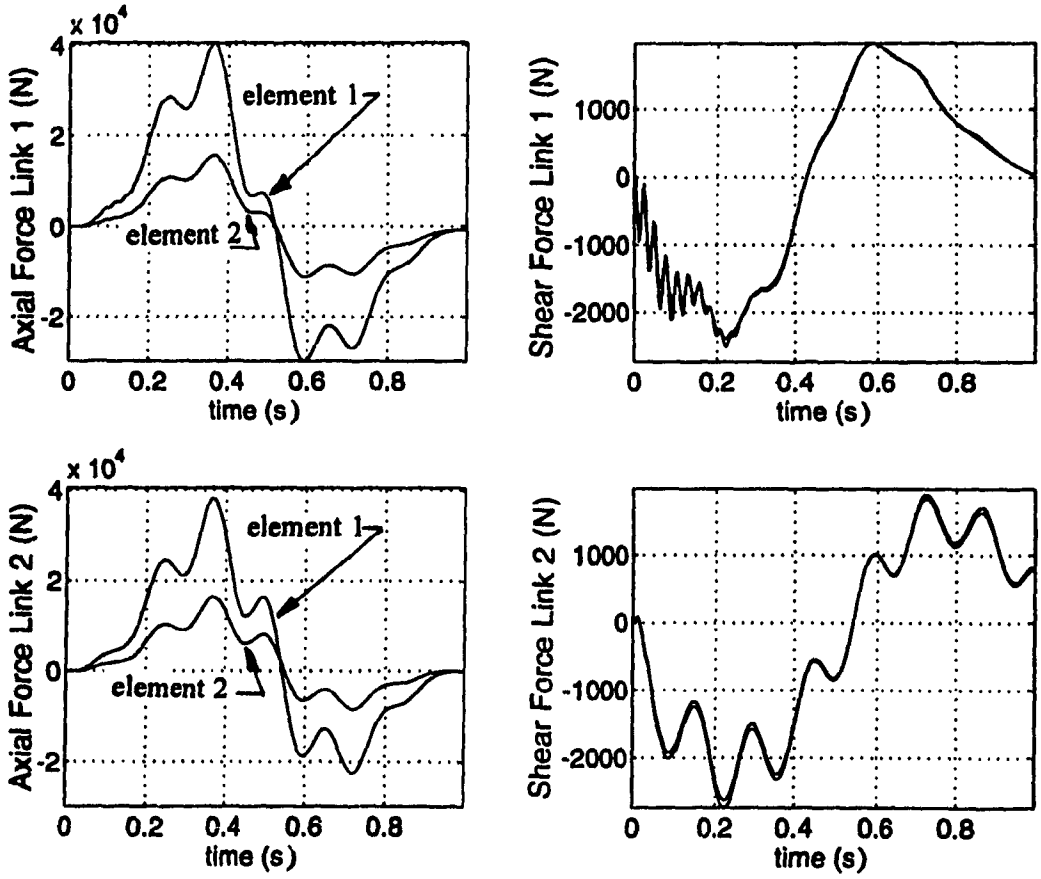

Figure 4.52. Axial and shear forces, cycloidal motion, $b = h = 0.05$m, $m_p = 50$ kg.

significant contribution to the force system. As it is known, shear forces are more significant for large cross-sections as compared to smaller cross-sections. In other words, failure by shear is more probable with larger cross sections [35]. Also, for the first and second link, the shear force has a close to uniform distribution along the links much like the shear forces in the case of the 3×3 cm cross-section in Figure 4.41. The payload's inertia contributes more significantly to the transverse forces than the element's inertia.

From Figure 4.53 and Figure 4.54, the criteria for failure by buckling and yielding are verified respectively. In Figure 4.54, the criteria for yield has been violated, signifying failure by yield as opposed to buckling. This corresponds to a payload of 50 kg determined earlier. Due to Figure 4.53, buckling is unlikely as the axial force is completely within the boundaries of the critical load (0.91×10^5 N).

Finally, the effect of the load's arm is investigated with the same manipulator, that is, $b = h = 5$ cm, and links' length of 1 m. Comparisons to the results obtained earlier with the 3 cm square cross section links (Figures 4.42 to 4.47 for both the first and second payload location case). Here, the offset of the payload is once again $r_p = 0.4$ m. The results for the first case and for the second case are shown in Figures 4.55 to 4.60. They include applied torques, axial/transverse deflections and internal forces. These are for a payload of 40 kg in both cases, which is the maximum that can be manipulated according to the yield limit. The payload limit turns out to be identical in both cases since stresses

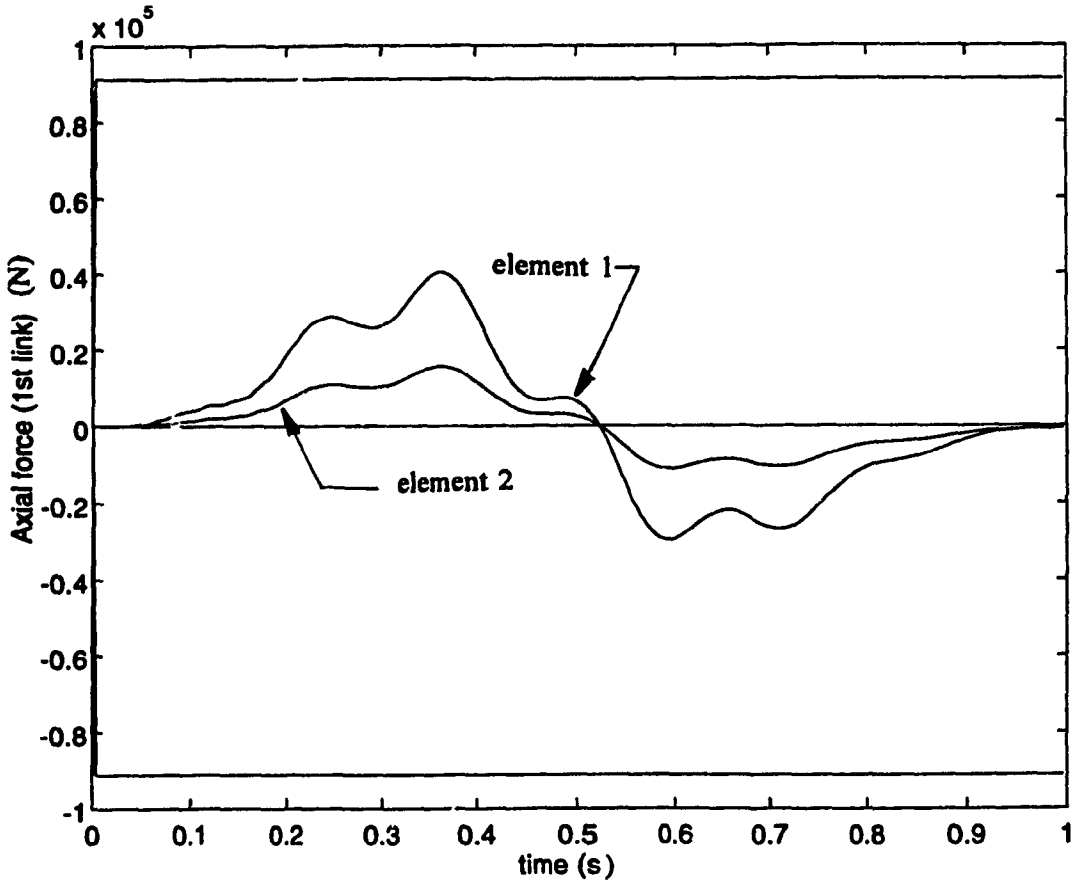

Figure 4.53. Comparison of axial force and critical load, $b = h = 0.05$m, $m_p = 50$ kg.

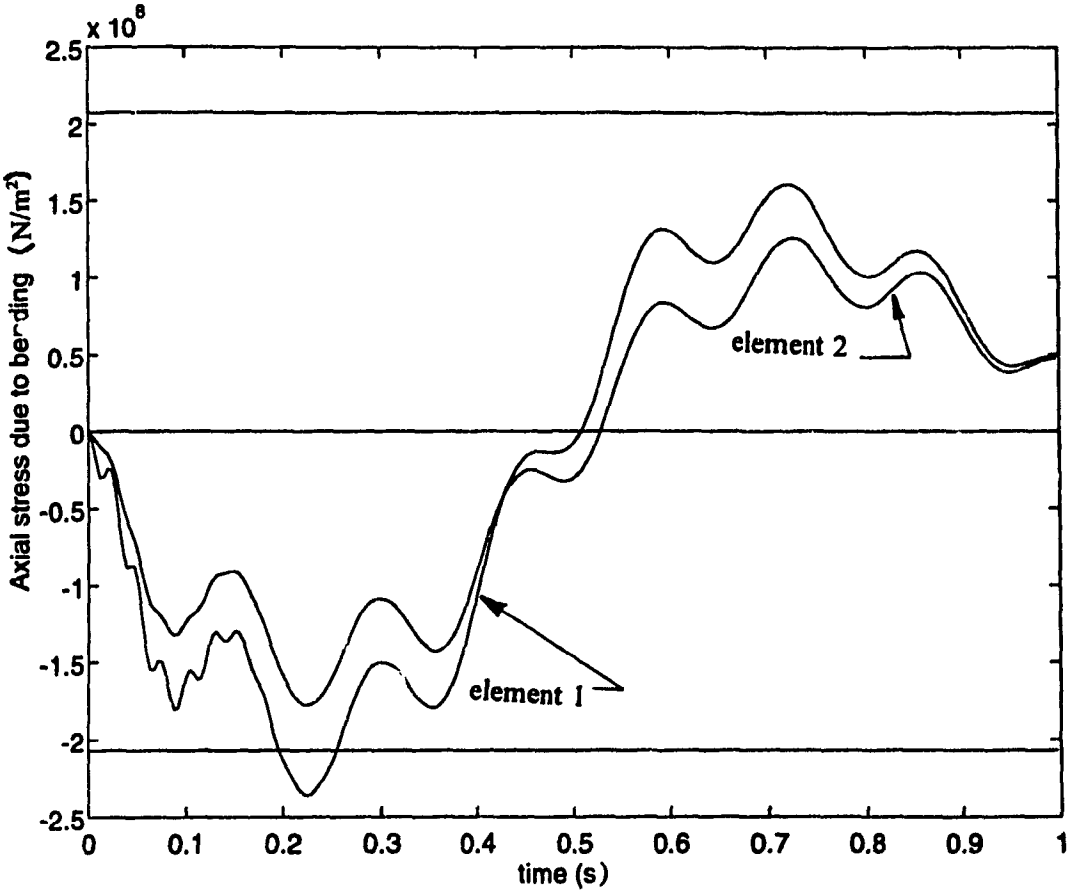

Figure 4.54. Comparison of yield strength and axial stress bending, $b = h = 0.05$m, $m_p = 50$kg.

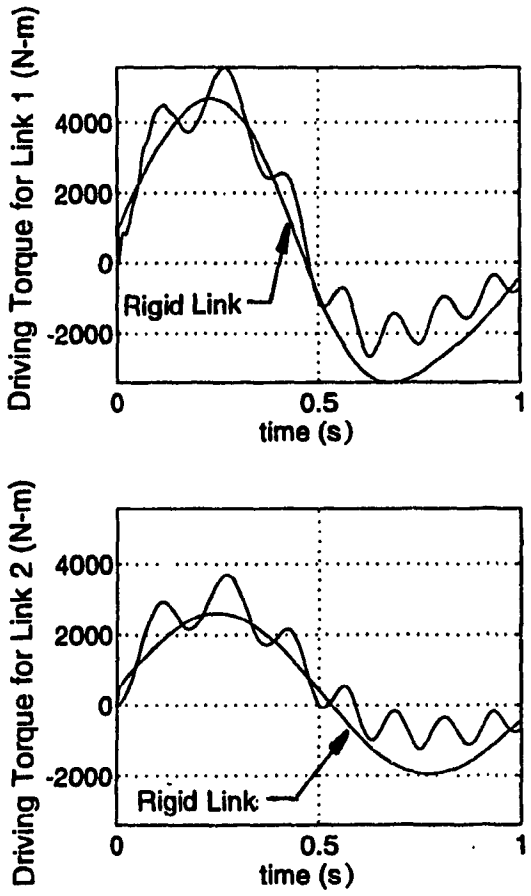

Figure 4.55. Driving torques for cycloidal motion, horizontal payload, b=h=0.05m.

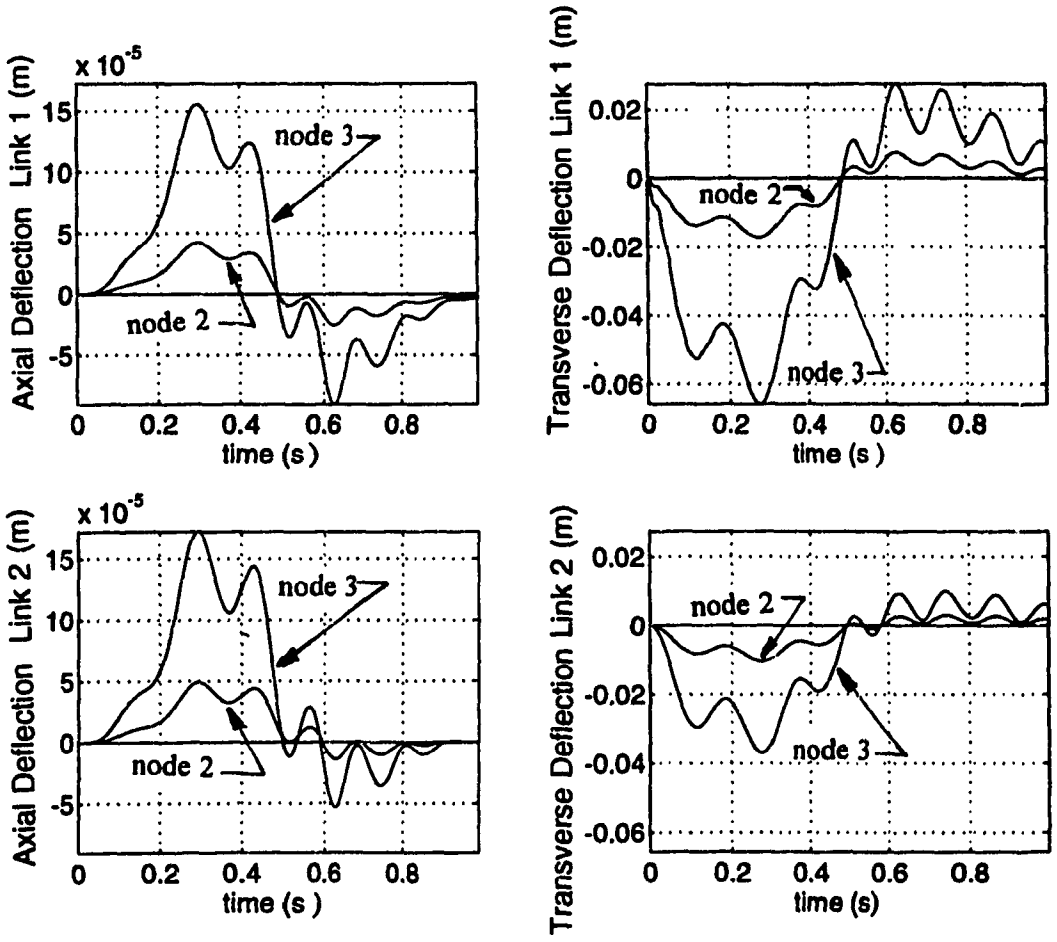

Figure 4.56. Axial and transverse deflections, cycloidal motion, horizontal payload, b=h=0.05m.

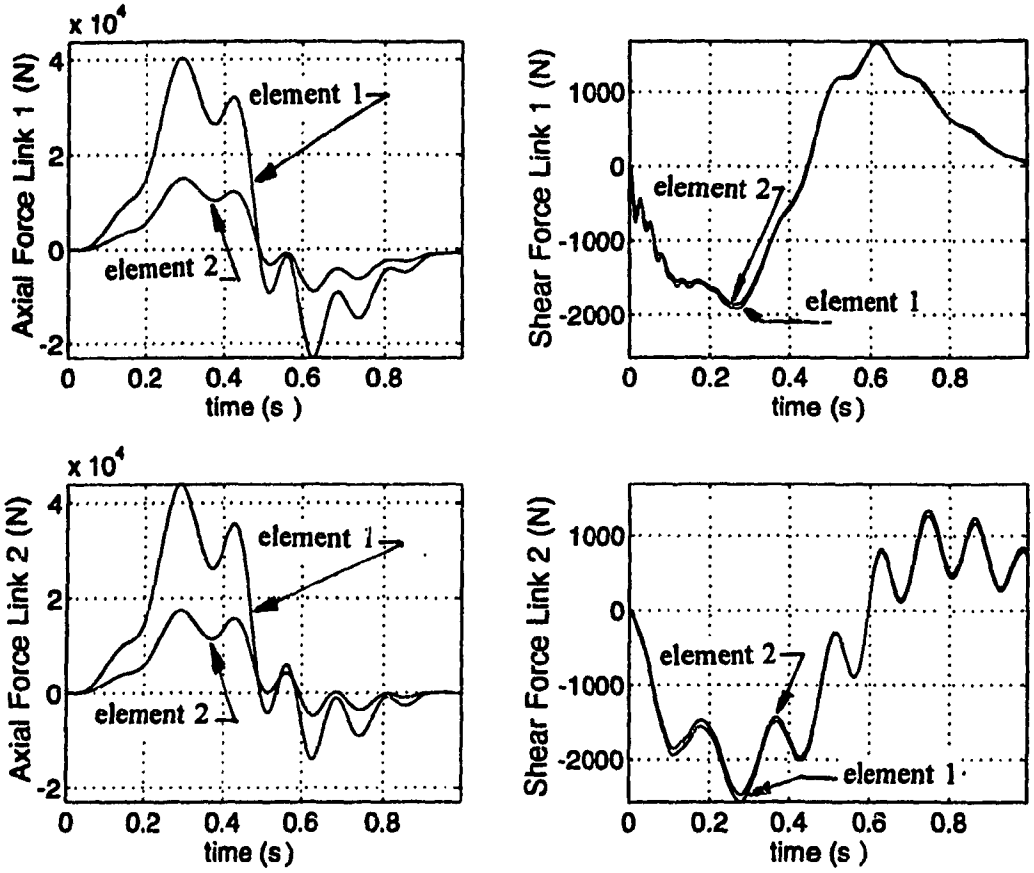

Figure 4.57. Axial and shear forces, cycloidal motion, horizontal payload, b=h=0.05m.

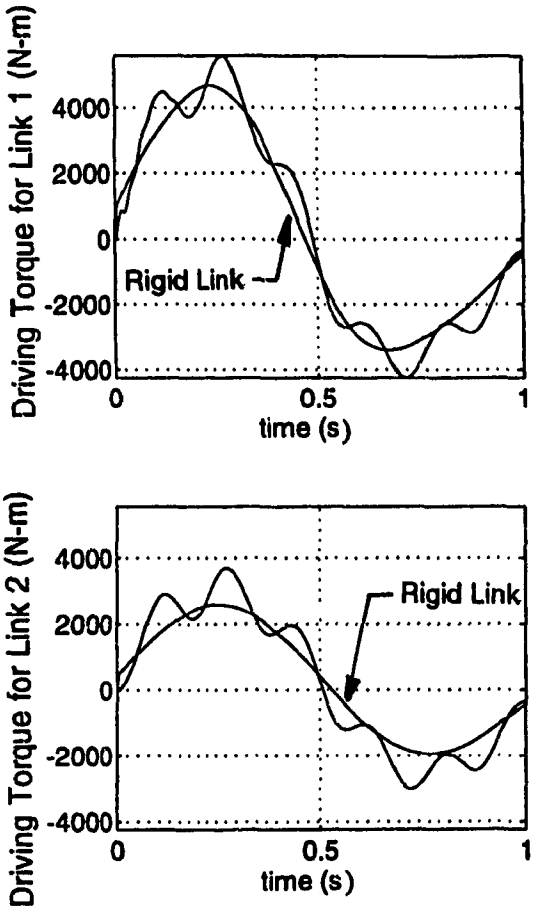

Figure 4.58. Driving torques for cycloidal motion, extended payload, b=h=0.05m.

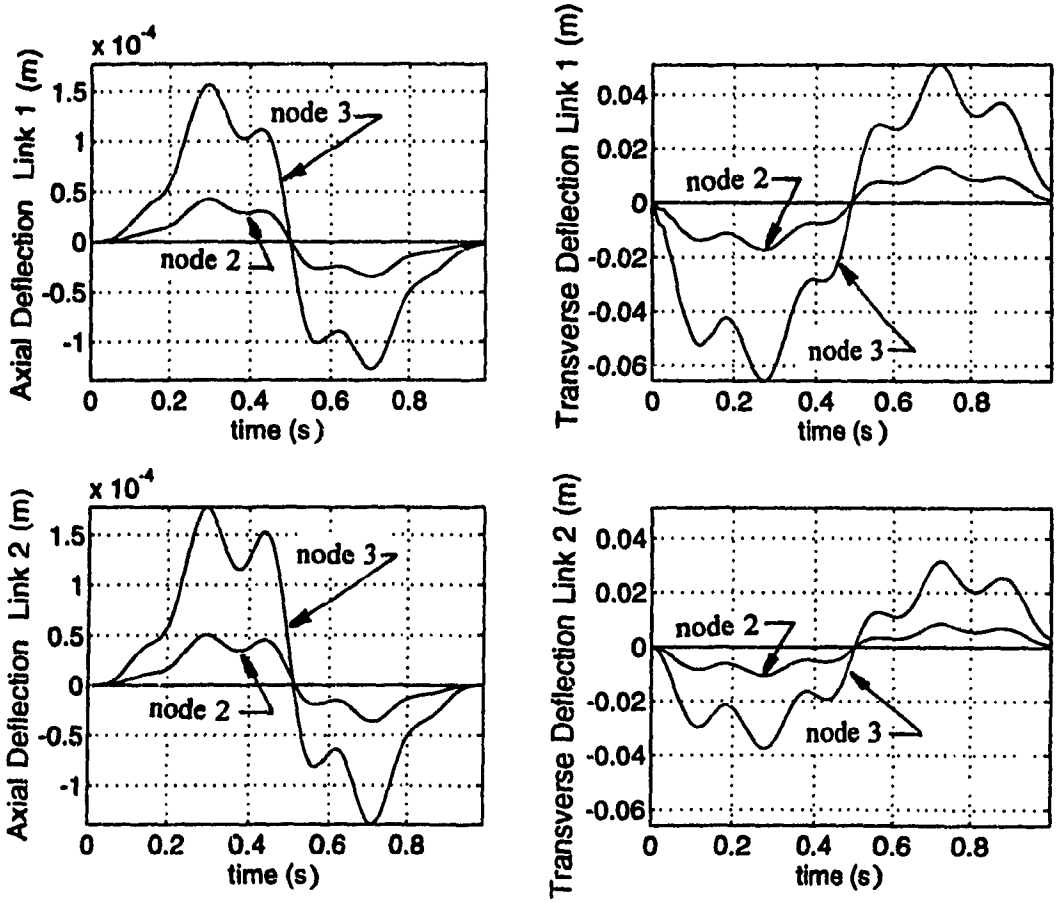

Figure 4.59. Axial and transverse deflections, cycloidal motion, extended payload, b=h=0.05m.

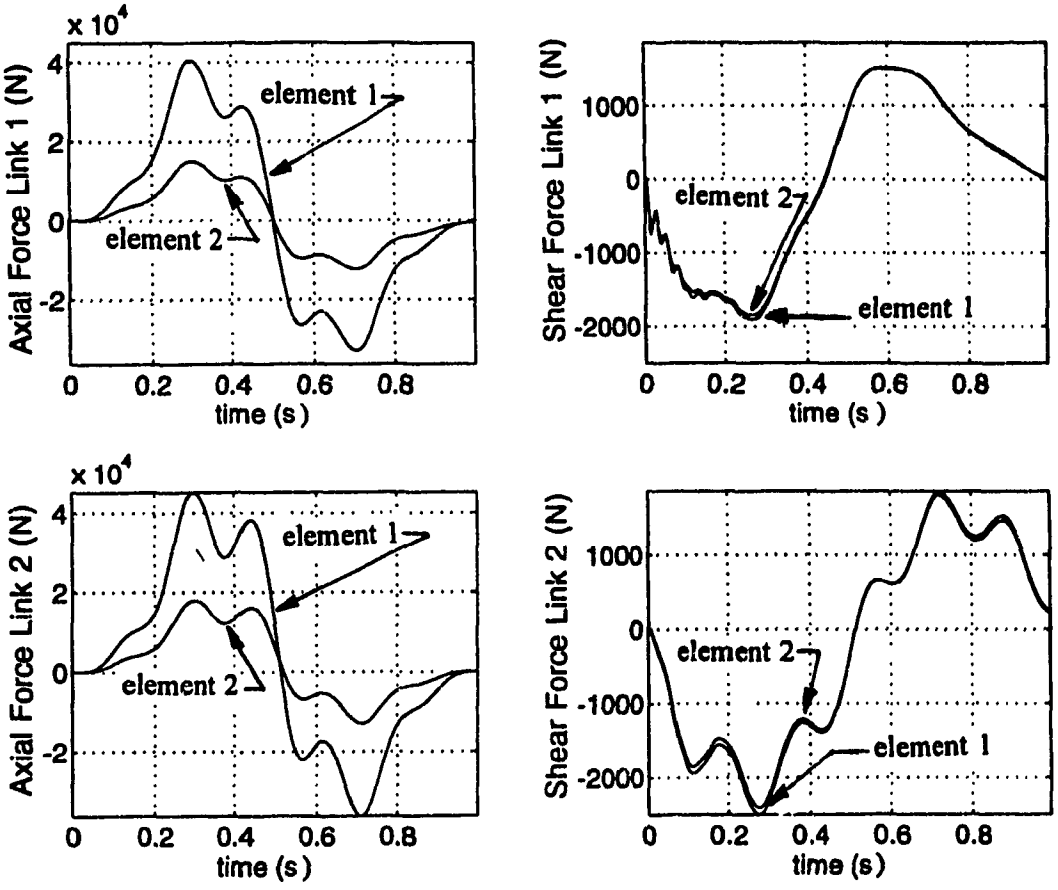

Figure 4.60. Axial and Shear Forces, Cycloidal Motion, extended payload, b=h=0.05m.

due to bending are symmetric. Thus, the critical load according to the yield limit occurs at the beginning of the trajectory where, as stated earlier, the two cases of payload offsetting give almost identical response.. For more flexible manipulators, buckling criteria is used toward the end of the trajectory as the axial forces begin to compress the two links. The axial stress relative to the yield limit is shown in Figures 4.61 and 4.62 for the first and the second case of payload offset respectively.

4.3.3. Effect of Numerical Integration Parameters

The effects of the numerical integration parameters are discussed briefly. Results for $\Theta_1 = \Theta_2 = 0.5$ and $\Theta_1 = \Theta_2 = 1.0$ representing no damping and maximum numerical damping, respectively, are shown in Figures 4.63 to 4.68. Driving torques, axial and transverse deflections, and axial and transverse forces are illustrated. In the case of minimum damping, persistent oscillations are evident as shown for first link's torque, transverse deflections and shear forces. They may be due to an incrementing error induced by discretization which is effectively damped out in Figures 4.66 to 4.68 for the case of maximum damping. Looking at the axial deflections and axial forces for the second link in this case, a compression is expected at the end of the trajectory. It is observed for the case of minimum damping, and should exist for this case too since the links undergo a compression. This discrepancy indicates the order of magnitude of the deflection is very small

and as such is affected by the numerical damping which overdamps the results. In other cases, no effect is noticed since the order of magnitude is high enough, or at least beyond that of the numerical damping. Care must be taken to choose reasonable values for the integration parameters, even though limits are suggested ($0.5 \leq \Theta_1, \Theta_2 \leq 1$) [41]. In this thesis they were chosen to be 0.7 to emphasize payload effects while suppressing the higher frequency oscillations.

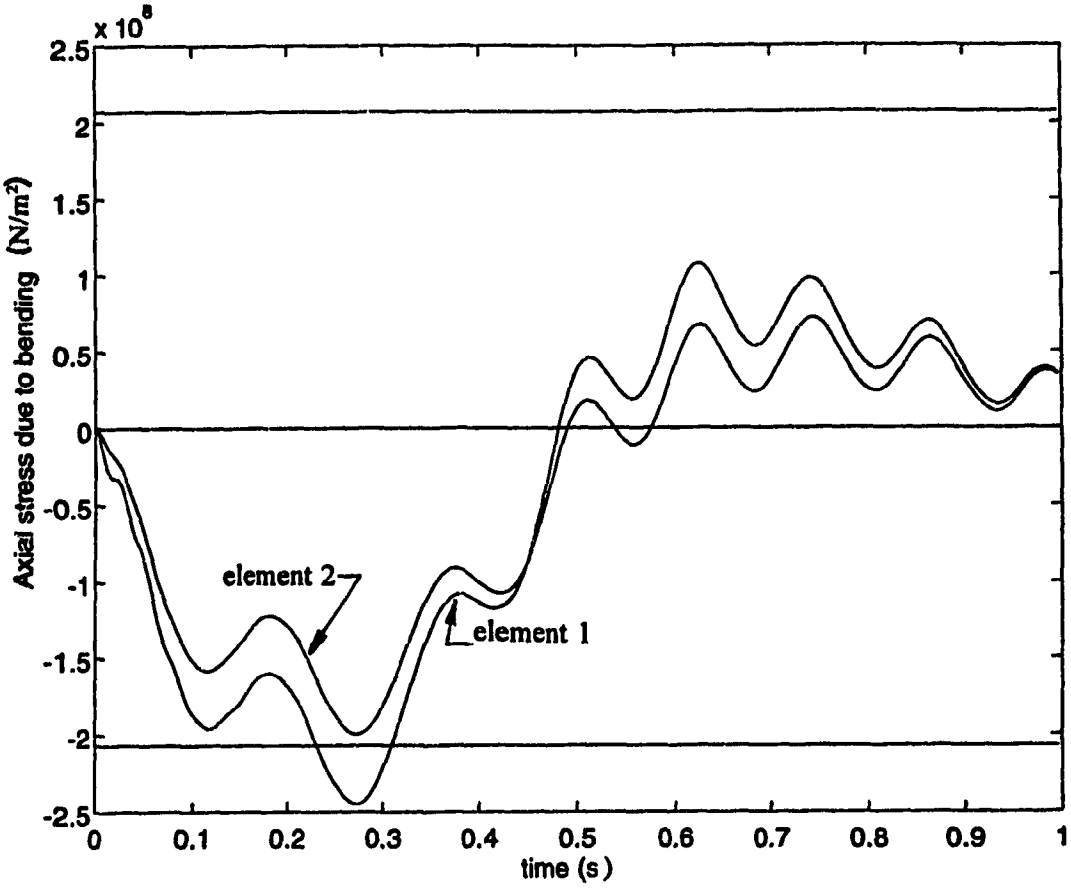

Figure 4.61. Comparison between yield strength and axial stress in bending, horizontal payload.

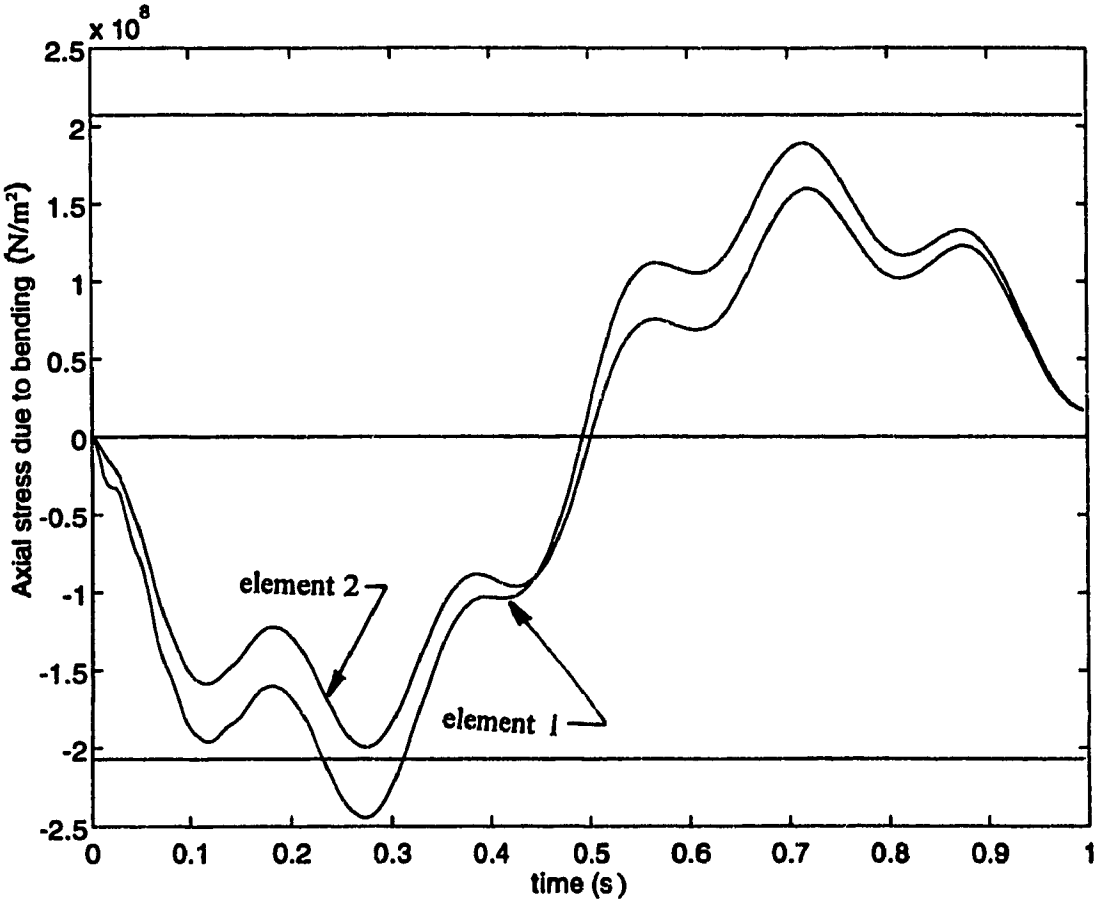

Figure 4.62. Comparison of yield strength and axial stress in bending, extended payload.

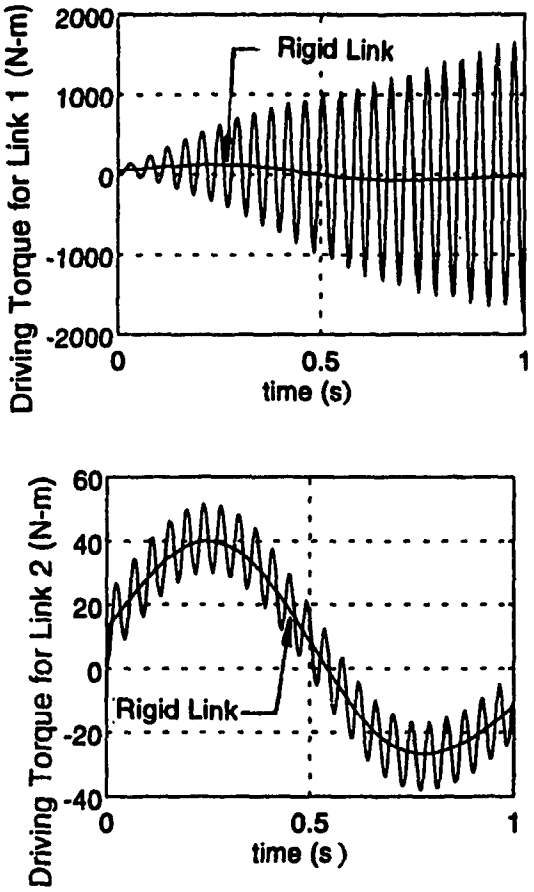

Figure 4.63. Driving torques for cycloidal response, minimum damping.

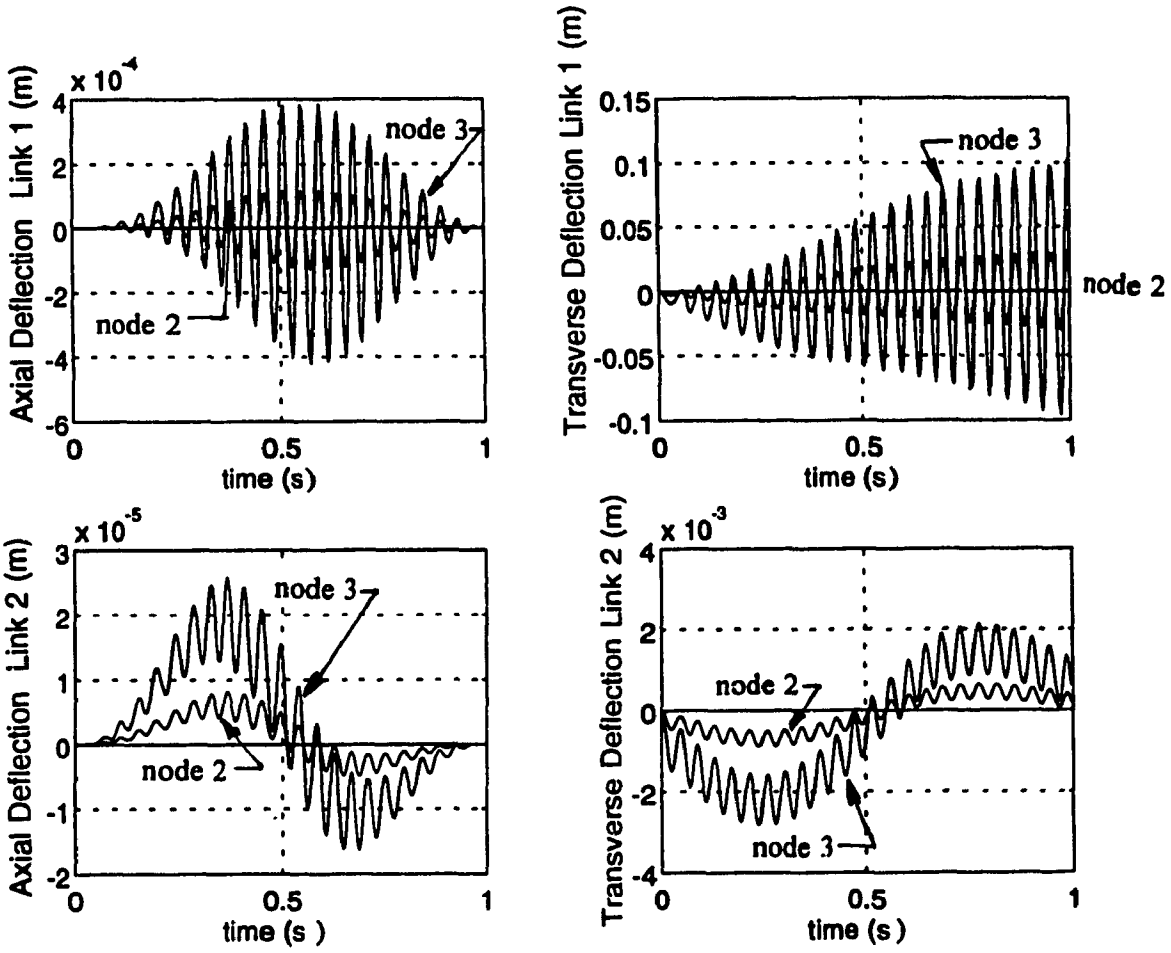

Figure 4.64. Axial and transverse deflections, cycloidal motion, minimum damping.

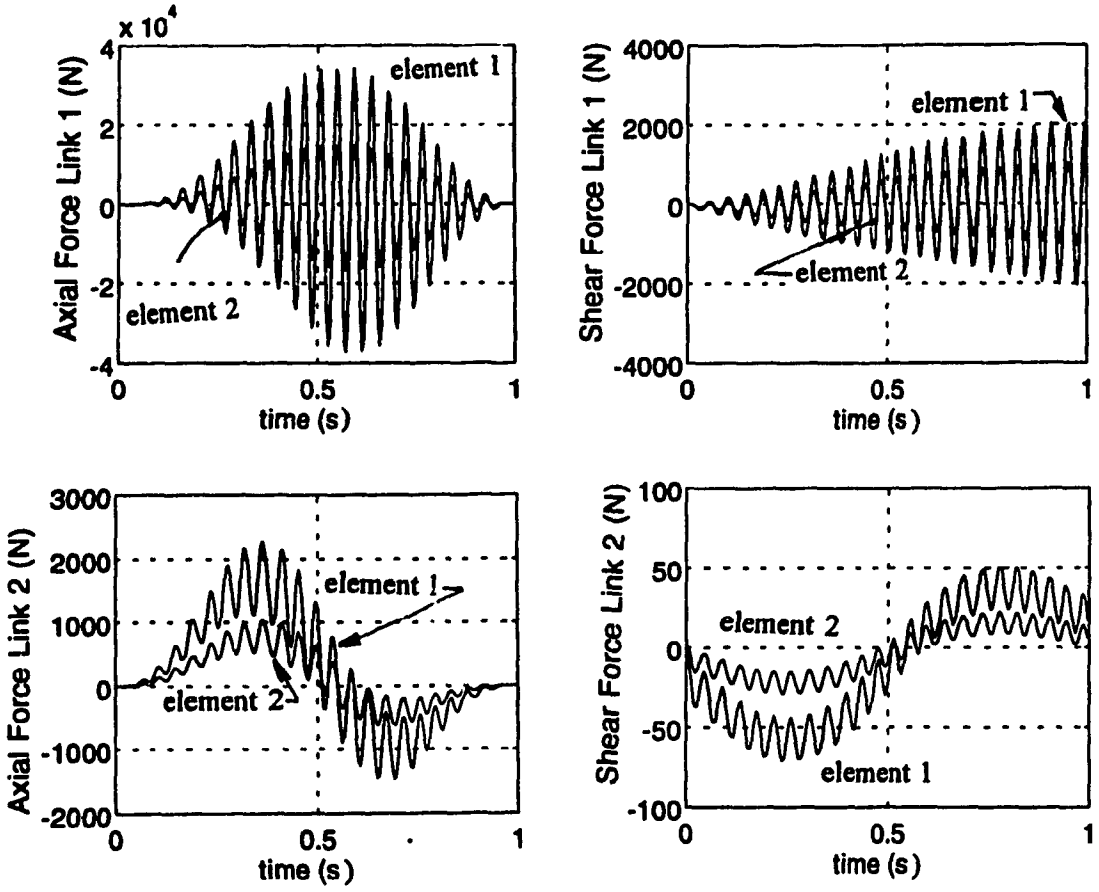

Figure 4.65. Axial and shear forces, cycloidal Motion, minimum damping.

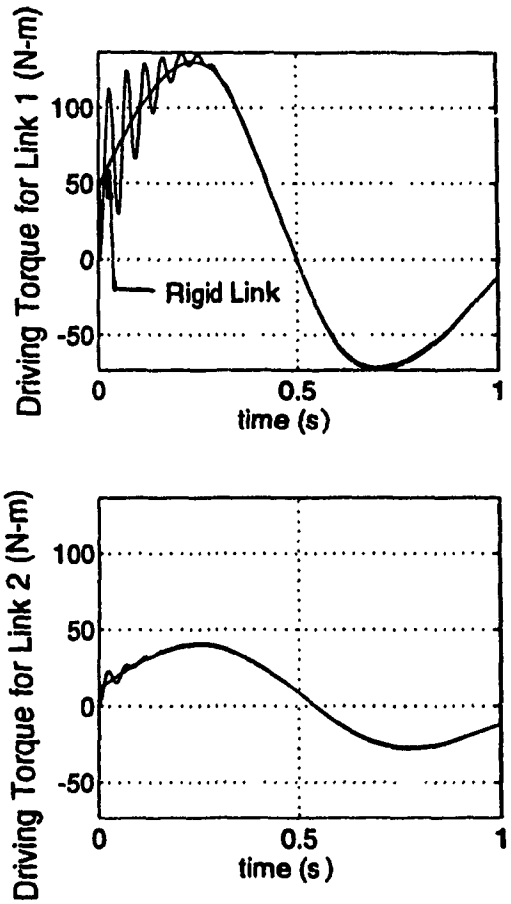

Figure 4.66. Driving torques for cycloidal motion, maximum damping.

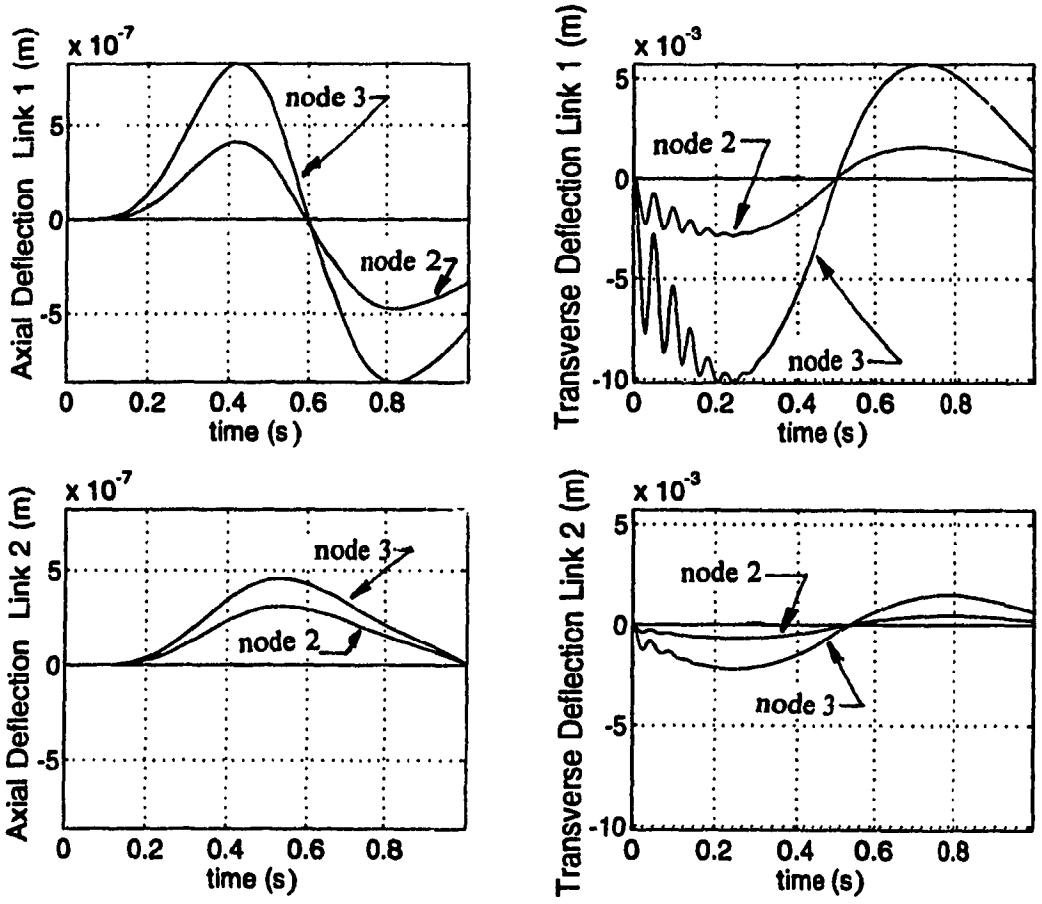

Figure 4.67. Axial and transverse deflections, cylcoidal motion, maximum damping.

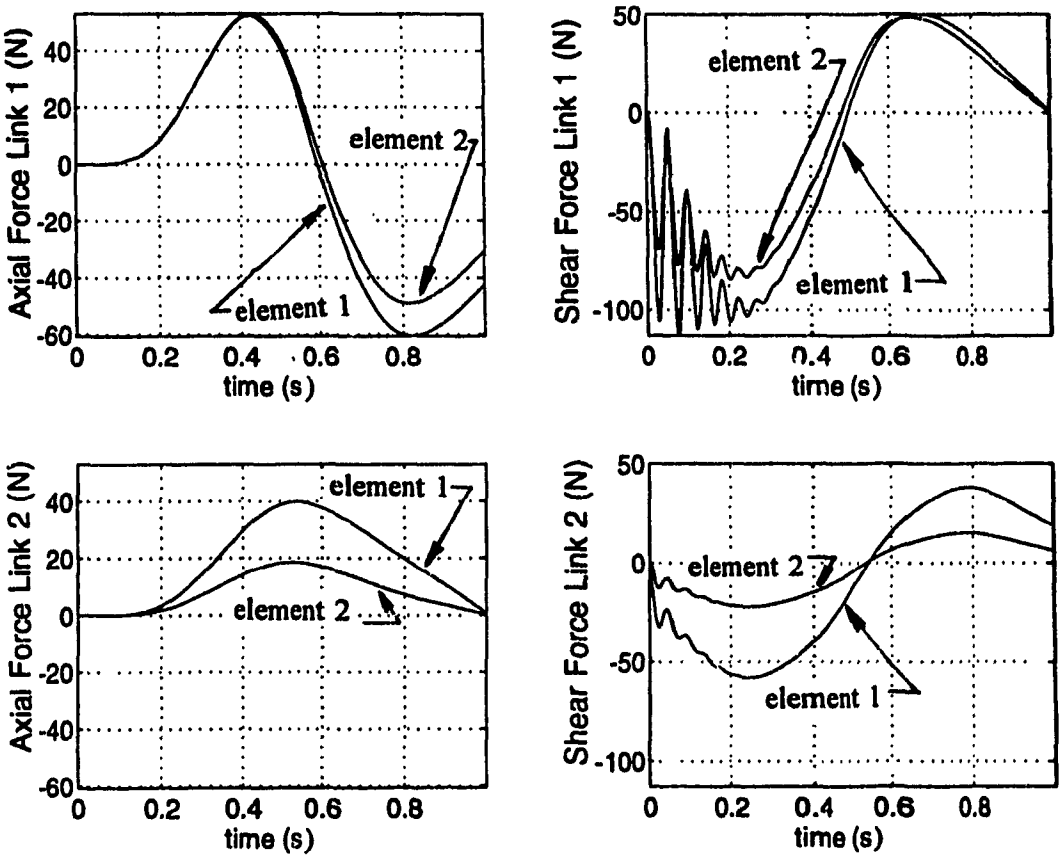

Figure 4.68. Axial and shear forces, cycloidal motion, maximum damping.

Chapter 5

CONCLUSION AND RECOMMENDATIONS

The study of the effects of a payload on a flexible manipulator which is undertaken with the knowledge that manipulators are non-rigid reveals that flexibility must be considered in the modelling of robot arms. Some conclusions are drawn from the present work. Furthermore, some recommendations for future work are proposed.

5.1 Conclusions

The effects of a payload on a two-link flexible manipulator was studied. Two trajectories were employed, a step trajectory and a cycloidal trajectory. The first allowed the verification of the model and provided some information on the effects of the payload. The second provided a more realistic trajectory and revealed the performance of the manipulator under the various assumptions about payload position. The following conclusions may be drawn from the results:

1. The addition of a payload to the end effector of the manipulator effectively decreases the stiffness of the system. This is justified by

the reduction in the frequency of the responses. A similar statement may be made about the payload arm since, for the same payload, a further reduction of the frequency was observed.

2. For the hollow links (outer square of 5 cm and thickness 1 mm) and short links (length of 0.5 m), the payload dominates the dynamics of the links due to the almost negligible mass of the links as compared to the mass of the payload and its inertia. The effects of payload are more pronounced in the lightweight manipulators.

3. The hollow links provide a high payload mass to manipulator mass ratio as compared to their solid counterparts. This indicates a greater effectiveness in manipulation since most of the driving torque is used to move the mass rather than the manipulator links. A control technique is needed to compensate for the increased deflections associated with the lower rigidity.

4. Payload capacity of a manipulator increases with increasing rigidity (as the links become shorter and thicker) and failure is determined by the yield limit. The yield criteria allows much larger payloads than the buckling criteria.

5. Increased flexibility leads to a change in failure criteria from yielding to buckling. For the cycloidal trajectory studied, the increase in payload induced low frequency response while increased inertia induced large internal forces in the links.

6. For the cycloidal trajectory, with the horizontal displacement of the payload relative to the end-effector, the frequency of oscillations increased throughout the motion. The lowest frequency, indicating the most flexible configuration, occurs at the initial position when the payload is simply at an extension of the robot links.

Generally, the present study provides useful information for control and design purposes: driving torques, transverse and axial deflections, and shear and axial forces. Nevertheless, some recommendations for future investigation are in order.

5.2 Recommendations for Future Work

Some effects of payload on a flexible manipulator have been observed, yet room for some further investigation is left. Although the present model adequately formulates the effects of payload on the manipulator under specified conditions, some limitations of the model are foreseen.

For the manipulator model, the elastic effects on rigid body motion will need

to be taken into account for lightweight robot arms. The overall motion of the system is affected not only by the nominal motion but also by the elastic motion. As illustrated, the payload contributes to this elastic motion. In this work, the manipulator model considered the superposition of elastic motion on rigid body motion and included the effect of rigid body motion on the elastic motion but not the reverse.

In order to better model the payload/manipulator system several additions would lead to a more complete and complex model. The mass and inertia of the actuators can be added to the model as lumped masses at the joints of the links. Furthermore, joint flexibilities can be considered in cases with high speed operation.

The payload mass, in this investigation, consisted simply of a lumped mass at the end effector or offset from it. The whole manipulator-mass system remained in the plane. If the payload is displaced away from the plane of the manipulator, a twisting of the links about their axes would occur. In this case, the model should incorporate an extra degree of freedom at the nodes for torsional deformation. Such a formulation would lead to a different set of design and control information. In addition, a more general model for payload effects would emerge.

Further research may focus on trajectory optimization. Some questions that would be asked include: In what configuration should a certain manipulator carry a payload? Should the payload be close to the base or far from the base?

Optimization techniques could be used to obtain a trajectory which limits the end points deflections and constrains the internal forces to some maximum values.

Finally, several studies may be made to consider unisotropic materials, varying cross-section size, different types of finite elements, and non-linearities which were not taken into account in this study. Most importantly, experimental validation of the theoretical findings should prove useful in order to continue progress.

REFERENCES

1. Vukobratović, M., *Applied Dynamics of Manipulation Robots*, Springer-Verlag: New York, 1989.

2. Taylor, R.H., et al., "An Image-Directed Robotic System for Precise Orthopaedic Surgery," *IEEE Transactions on Robotics and Automation*, Vol. 10, No. 3, 1994.

3. DeGarmo, E.P., Black, J.T., and Kohser, R.A., *Materials and Processes in Manufacturing*, 7th edition, Macmillan Publishing Company: New York, 1988.

4. Parks, T.R., and Pak, H.A., "Effect of Payload on the Dynamics of a Flexible Manipulator - Modeling for Control," *ASME Journal of Dynamic Systems, Measurement, and Control*, Vol. 113, 1991, pp. 409-418.

5. Asada, H., Ma, Z-D., and Tokumaru, H., "Inverse Dynamics of Flexible Robot Arms: Modelling and Computation for Trajectory Control," *ASME Journal of Dynamic Systems, Measurement, and Control*, Vol. 112, 1990, pp. 177-185.

6. Mabie, H.H., and Reinholtz, C.F., *Mechanisms and Dynamics of Machinery*, 4th edition, John Wiley and Sons: New York, 1987.

7. Benedict, C.E., and Tesar, D., "Dynamic Response Analysis of Quasi-Rigid Mechanical Systems Using Kinematic Influence Coefficients," *Journal of Mechanisms*, Vol. 6, 1971, pp. 383-403.

8. Dubowsky, S., and Gardner, T.N., "Design and Analysis of Multi-Link Flexible Mechanism with Clearance Connections," *Journal of Engineering for Industry*, Vol. 99, 1977, pp. 88-96.

9. Book,W.J, "Analysis of Massless Elastic Chains with Servo Controlled Joints," *Journal of Dynamic Systems Measurement and Control*, Vol. 101, 1979, pp. 187-192.

10. Huston, R.L., "Flexibility Effects in Multibody System Dynamics," *Mechanism Research Communications*, Vol. 7, 1980, pp. 261-268.

11. Kelly, F.A., and Huston, R.L., "Modelling of Flexibility Effects in Robot Arms," *Proceedings of the 1981 American Control Conference*, 1981, WP-2C.

12. Book, W.J., "Recursive Lagrangian Dynamics of Flexible Manipulator Arms," *The International Journal of Robotics Research*, Vol. 3, No. 3, 1984, pp. 87-101.

13. Sunada, W.H., and Dubowsky, S., "On the Dynamic Analysis and Behavior of Industrial Robotic Manipulators With Elastic Members," *ASME Journal of Mechanisms, Transmissions, and Automation in Design*, Vol. 105, 1983, pp. 42-51.

14. Usoro, P.B., Nadira, R., and Mahil, S.S., "A Finite Element/Lagrange Approach to Modeling Lightweight Flexible Manipulators," *ASME Journal of Dynamic Systems, Measurement, and Control*, Vol. 108, 1986, pp. 198-205.

15. Naganathan, G., and Soni, A.H., "Coupling Effects of Kinematics and Flexibility in Manipulators," *The International Journal of Robotics Research*, Vol. 6, No. 1, 1987, pp. 75-84.

16. Bayo, E., "A Finite-Element Approach to Control the End-Point Motion of a Single-Link Flexible Robot," *Journal of Robotic Systems*, Vol. 4, No. 1, 1987, pp. 63-75.

17. Bayo, E., Movaghar, R., and Medus, M., "Inverse Dynamics of a Single-Link Flexible Robot - Analytical and Experimental Results," *International Journal of Robotics and Automation*, Vol. 3, No. 3, 1988, pp. 150-157.

18. Bayo, E., Papadopoulos, P., Stubbe, J., and Serna, M.A., "Inverse Dynamics and Kinematics of Multi-Link Elastic Robots: An Iterative Frequency Domain Approach," *The International Journal of Robotics Research*, Vol. 8, No. 6, 1989, pp. 49-62.

19. Bricout, J.N., Debus, J.C., and Micheau, P., "A Finite Element Model for the Dynamics of Flexible Manipulators," *Mechanism and Machine Theory*, Vol. 25, No. 1, 1990, pp. 119-128.

20. Kalra, P., and Sharan, A.M., "On the Automated Generation of Dynamic Equations for Flexible Robotic Manipulators," *International Journal of Robotics and Automation*, Vol. 5, No. 2, 1990, pp. 92-97.

21. Beres, W., Sasiadek, J.Z, and Vukovich, G., "Control and Dynamic Analysis of Multilink Flexible Manipulator," *IEEE International Conference on Robotics and Automation*, Vol. 3, 1993, pp. 478-483.

22. Cetinkunt, S., and Book, W.J., "Performance Limitations of Joint Variable-Feedback Controllers Due to Manipulator Structural Flexibility," *IEEE Transactions on Robotics and Automation*, Vol. 6, No. 2, 1990, pp. 219-231.

23. Siciliano, B., and Book, W.J., "A Singular Perturbation Approach to Control of Lightweight Flexible Manipulators," *The International Journal of Robotics Research*, Vol. 7, No. 4, 1988, pp. 79-90.

24. Hastings, G.G., and Book, W.J., "A Linear Dynamic Model for Flexible Robotic Manipulators," *IEEE Control Systems Magazine*, Vol. 7, No. 1, 1987, pp. 61-64.

25. Cannon, R.H., and Schmitz, E., "Initial Experiments on the End-Point Control of a Flexible One-Link Robot," *The International Journal of Robotics Research*, Vol. 3, No. 3, 1984, pp. 62-75.

26. Matsuno, F., Asano, T., and Sakawa, Y., "Modeling and Quasi-Static Hybrid Position/Force Control of Constrained Planar Two-Link Flexible Manipulators," *IEEE Transactions on Robotics and Automation*, Vol. 10, No. 3, 1994, pp. 287-297.

27. Sakawa, Y., Matsuno, F., and Fukushima, S., "Modeling and Feedback Control of a Flexible Arm," *Journal of Robotic Systems*, Vol. 2, No. 4, 1985, pp. 453-472.

28. Whitney, D.E., Book, W.J., and Lynch, P.M., "Design and Control Considerations for Industrial and Space Manipulators," *Proceedings of the 1974 American Control Conference*, 1974, pp. 591-598.

29. Jen, C.W. and Johnson D.A., "Modal Sensitivity Analysis of Planar Robots, Based on a Simplified CMS Approach," *Journal of Robotic Systems*, Vol. 8, No. 4, 1991, pp. 443-463.

30. Wang, P.K.C., and Wei, J-D, "Vibrations in a Moving Flexible Robot Arm," *Journal of Sound and Vibration*, Vol. 116, No. 1, 1987, pp. 149-160.

31. Korayem, M.H., and Basu, A., "Formulation and numerical solution of elastic robot dynamic motion with maximum load carrying capacities," *Robotica*, Vol. 12, 1994, pp. 253-261.

32. Shames, I.H., and Dym, C.L., *Energy and Finite Element Methods in Structural Mechanics*, McGraw-Hill Book Company: New York, 1985.

33. Timoshenko, S.P., "On the Correction for Shear of the Differential Equation for Transverse Vibrations of Prismatic Bars," *Philosophical Magazine and Journal of Science*, Series 6, Vol. 41, 1921, pp. 744-746.

34. Schiff, D., *Dynamic Analysis and Failure Modes of Simple Structures*, John Wiley & Sons: New York, 1990.

35. Lee, T-S., and Lin, Y-J., "Shear deformation effect in design consideration of flexible manipulators," *Robotica*, Vol. 11, 1993, pp. 83-92.

36. Thomson, W.T., *Theory of Vibration with Applications*, 4th edition, Prentice-Hall: New Jersey, 1993.

37. Petyt, M., *Introduction to Finite Element Vibration Analysis*, Cambridge University Press: New York, 1990.

38. Weaver Jr., W., and Johnston, P.R., *Structural Dynamics by Finite Elements*, Prentice-Hall, Inc.: New Jersey, 1987.

39. Zienkiewicz, O.C., Wood, W.L., and Hines, N.W., "A Unified Set of Single Set Algorithms (Part 1: General Formulation and Applications)," *International Journal for Numerical Methods in Engineering*, Vol. 20, 1984, pp. 1529-1552.

40. Meirovitch, L., *Analytical Methods in Vibration*, Macmillan: New York, 1967.

41. Wood, W.L., "A Unified Set of Single Step Algorithms (Part 2: Theory)," *International Journal for Numerical Methods in Engineering*, Vol. 20, 1984, pp. 2303-2309.

Appendix I

Element Matrices

Element Mass Matrix

$$[M]_{ne}=\begin{bmatrix} \rho Al/3 & 0 & 0 & \rho Al/6 & 0 & 0 \\ 0 & \rho Al/3 & 0 & 0 & \rho Al/6 & 0 \\ 0 & 0 & \rho I_G l/3 & 0 & 0 & \rho I_G l/6 \\ \rho Al/6 & 0 & 0 & \rho Al/3 & 0 & 0 \\ 0 & \rho Al/6 & 0 & 0 & \rho Al/3 & 0 \\ 0 & 0 & \rho I_G l/6 & 0 & 0 & \rho I_G l/3 \end{bmatrix}_n$$

Element Damping Matrix (due to motion of rigid link)

$$[C]_{ne}=\begin{bmatrix} 0 & -2\rho A\omega_b l/3 & 0 & 0 & -\rho A\omega_b l/3 & 0 \\ 2\rho A\omega_b l/3 & 0 & 0 & \rho A\omega_b l/3 & 0 & \\ 0 & 0 & 0 & 0 & 0 & 0 \\ 0 & -\rho A\omega_b l/3 & 0 & 0 & -2\rho A\omega_b l/3 & 0 \\ \rho A\omega_b l/3 & 0 & 0 & 2\rho A\omega_b l/3 & 0 & \\ 0 & 0 & 0 & 0 & 0 & 0 \end{bmatrix}_n$$

Element Stiffness Matrix (Exact)

$$[K_s]_{ne}=\begin{bmatrix} AE/l & 0 & 0 & -AE/l & 0 & 0 \\ 0 & kA\gamma/l & kA\gamma/2 & 0 & -kA\gamma/l & kA\gamma/2 \\ 0 & kA\gamma/2 & EI_z/l+kA\gamma l/3 & 0 & -kA\gamma/2 & -EI_z+kA\gamma l/6 \\ -AE/l & 0 & 0 & AE/l & 0 & 0 \\ 0 & -kA\gamma/l & -kA\gamma/2 & 0 & kA\gamma/l & -kA\gamma/2 \\ 0 & kA\gamma/2 & -EI_z/l+kA\gamma l/6 & 0 & -kA\gamma/2 & EI_z+kA\gamma l/3 \end{bmatrix}_n$$

Element Stiffness Matrix (Reduced Order Integration)

$$[K_s]_{ne}=\begin{bmatrix} AE/l & 0 & 0 & -AE/l & 0 & 0 \\ 0 & kA\gamma/l & kA\gamma/2 & 0 & -kA\gamma/l & kA\gamma/2 \\ 0 & kA\gamma/2 & EI_z/l+kA\gamma l/4 & 0 & -kA\gamma/2 & -EI_z+kA\gamma l/4 \\ -AE/l & 0 & 0 & AE/l & 0 & 0 \\ 0 & -kA\gamma/l & -kA\gamma/2 & 0 & kA\gamma/l & -kA\gamma/2 \\ 0 & kA\gamma/2 & -EI_z/l+kA\gamma l/4 & 0 & -kA\gamma/2 & EI_z+kA\gamma l/4 \end{bmatrix}_n$$

Element Stiffnes Matrix (due to motion of rigid link)

$$[K_m]_{ne}=\begin{bmatrix} -\rho A\omega_b^2 l/3 & -\rho A\alpha_b l/3 & 0 & -\rho A\omega_b^2 l/6 & -\rho A\alpha_b l/6 & 0 \\ \rho A\alpha_b l/3 & -\rho A\omega_b^2 l/3 & 0 & \rho A\alpha_b l/6 & -\rho A\omega_b^2 l/6 & 0 \\ 0 & 0 & 0 & 0 & 0 & 0 \\ -\rho A\omega_b^2 l/6 & -\rho A\alpha_b l/6 & 0 & -\rho A\omega_b^2 l/3 & -\rho A\alpha_b l/3 & 0 \\ \rho A\alpha_b l/6 & -\rho A\omega_b^2 l/6 & 0 & \rho A\alpha_b l/3 & -\rho A\omega_b^2 l/3 & 0 \\ 0 & 0 & 0 & 0 & 0 & 0 \end{bmatrix}_n$$

Element Force Vector

$$[F]_{ne}=\begin{bmatrix} \rho Al(\omega_b^2(2x_1+x_2)/6-a_{bx}/2)+f_x l/2 \\ -\rho Al(\alpha_b(2x_1+x_2)/6+a_{by}/2)+f_y l/2 \\ -\rho I_G \alpha_b l/2 \\ \rho Al(\omega_b^2(x_1+2x_2)/6-a_{bx}/2)+f_x l/2 \\ -\rho Al(\alpha_b(x_1+2x_2)/6+a_{by}/2)+f_y l/2 \\ -\rho I_G \alpha_b l/2 \end{bmatrix}_n$$

Appendix II

Element Matrices due to Payload Mass

The following element matrices are added to the last element matrices of the most outer link of the manipulator (upon assembling).

Mass matrix due to payload

$$[M]_{pay}=\begin{bmatrix} 0 & 0 & 0 & 0 & 0 & 0 \\ 0 & 0 & 0 & 0 & 0 & 0 \\ 0 & 0 & 0 & 0 & 0 & 0 \\ 0 & 0 & 0 & m_p & 0 & 0 \\ 0 & 0 & 0 & 0 & m_p & 0 \\ 0 & 0 & 0 & 0 & 0 & m_p(l/2+r_p)^2 \end{bmatrix}$$

Damping matrix due to motion coming from payload

$$[C]_{pay}=\begin{bmatrix} 0 & 0 & 0 & 0 & 0 & 0 \\ 0 & 0 & 0 & 0 & 0 & 0 \\ 0 & 0 & 0 & 0 & 0 & 0 \\ 0 & 0 & 0 & 0 & -2m_p\omega_b & 0 \\ 0 & 0 & 0 & 2m_p\omega_b & 0 & 0 \\ 0 & 0 & 0 & 0 & 0 & 0 \end{bmatrix}$$

Stiffness matrix due to motion coming from payload

$$[K]_{pay}=\begin{bmatrix} 0 & 0 & 0 & 0 & 0 & 0 \\ 0 & 0 & 0 & 0 & 0 & 0 \\ 0 & 0 & 0 & 0 & 0 & 0 \\ 0 & 0 & 0 & -m_p\omega_b^2 & -m_p\alpha_b & 0 \\ 0 & 0 & 0 & m_p\alpha_b & -m_p\omega_b^2 & 0 \\ 0 & 0 & 0 & 0 & 0 & 0 \end{bmatrix}$$

Force vector due to payload

$$[F]_{pay}=\begin{bmatrix} 0 \\ 0 \\ 0 \\ \omega_b^2 l_w \cos\beta - \alpha_b l_w \sin\beta - m_p a_{bx} - m_p g \sin(q_1+q_2) \\ -\omega_b^2 l_w \sin\beta - \alpha_b l_w \cos\beta - m_p a_{by} - m_p g \sin(q_1+q_2) \\ -(\omega_b^2 l_w \cos\beta + \alpha_b l_w \sin\beta) r \sin q_w - (\omega_b^2 l_w \sin\beta + \alpha_b l_w \sin\beta)(\frac{l}{2} + r_p \cos q_w) - m_p g \cos(q_1+q_2-q_w)(\frac{l}{2}\cos q_w + r_p) \end{bmatrix}$$

Here, the angles β and q_w and the rest of the geometry are shown in Figure A2.1.

We have, by the cosine and sine laws,

$$\cos\beta = \frac{-r_p^2 + L_2^2 + l_w^2}{2 L_2 l_w}$$

$$\sin\beta = \frac{r}{l_w}\sin(\pi - q_w)$$

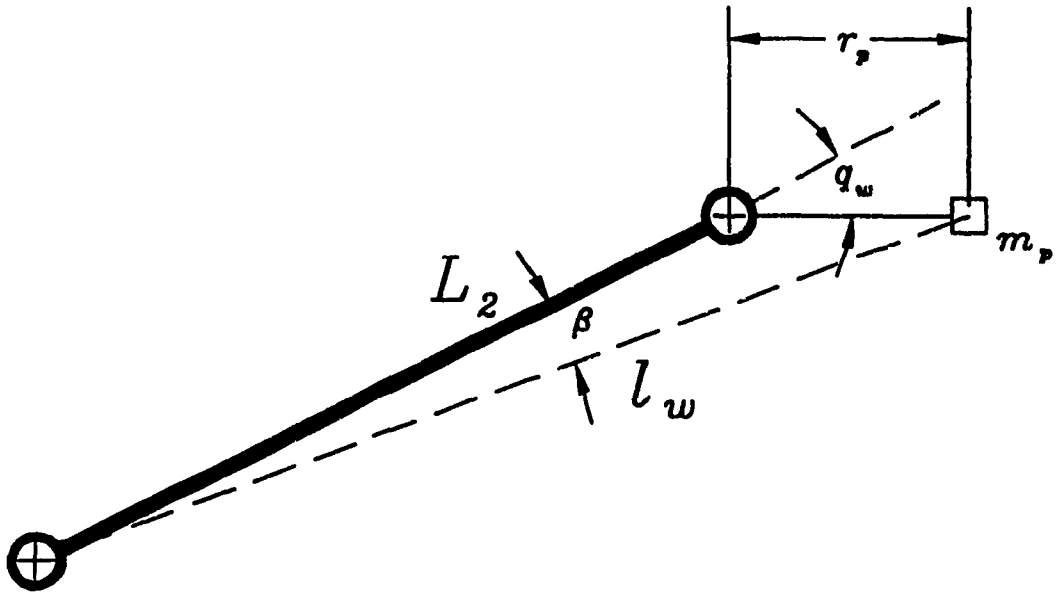

Figure A2.1. Outermost link with payload and payload arm.

Appendix III

Element Matrices due to Axial Force

Stiffness due to constant axial force

$$K_{ce}=P\begin{bmatrix} 0 & 0 & 0 & 0 & 0 & 0 \\ 0 & 0 & -\frac{1}{4} & 0 & 0 & -\frac{1}{4} \\ 0 & -\frac{1}{4} & -\frac{2}{3}l & 0 & \frac{1}{4} & -\frac{1}{3}l \\ 0 & 0 & 0 & 0 & 0 & 0 \\ 0 & 0 & \frac{1}{4} & 0 & 0 & \frac{1}{4} \\ 0 & -\frac{1}{4} & -\frac{1}{3}l & 0 & \frac{1}{4} & -\frac{2}{3}l \end{bmatrix}$$

Here,

$$P=W_{pay}\sin(\theta)+(n-i)\rho Agl\sin(\theta)$$

n = total number of elements

i = i-th element

Stiffness due to linearly varying axial force (self weight within element i)

$$K_w = W_i \begin{bmatrix} 0 & 0 & 0 & 0 & 0 & 0 \\ 0 & 0 & -\frac{1}{6} & 0 & 0 & -\frac{1}{12} \\ 0 & -\frac{1}{6} & -\frac{1}{4}l & 0 & \frac{1}{6} & -\frac{1}{6}l \\ 0 & 0 & 0 & 0 & 0 & 0 \\ 0 & 0 & \frac{1}{6} & 0 & 0 & \frac{1}{12} \\ 0 & -\frac{1}{12} & -\frac{1}{6}l & 0 & \frac{1}{12} & -\frac{1}{12}l \end{bmatrix}$$

Here, W_i is the linearly varying weight within element i,

$$W_i = \rho A g (x_2 - x) \sin(\theta)$$

Appendix IV

Verification of the Model

In order to verify the model of the flexible links manipulator, it is reduced to the rigid links case by increasing Young's Modulus. Here, Young's modulus is increased from 7.11×10^{10} N/m^2 to 7.11×10^{13} N/m^2. The cycloidal trajectory is followed. The parameters of the manipulator include b=h=0.02 m, L_1=L_2=1.0 m without payload. The results for the driving torques and deflections are shown in Figures A4.1 and A4.2 for the first case of Young's modulus. Figures A4.3 and A4.4 show the driving torques and deflections for the second case. The ideal rigid links torques are also plotted in the respective graphs. The slight discrepancy in Figure A4.3 is due to discretization. Thus, as the links become more rigid, the torques reduce to the ideal rigid links case. Obviously, for the ideal rigid links case, the deflections are zero. As the links become more rigid, the transverse deflections reduced from a maximum 0.02m to a maximum of just over 1×10^{-5} m. Obviously, these results serve as a good verification of the model.

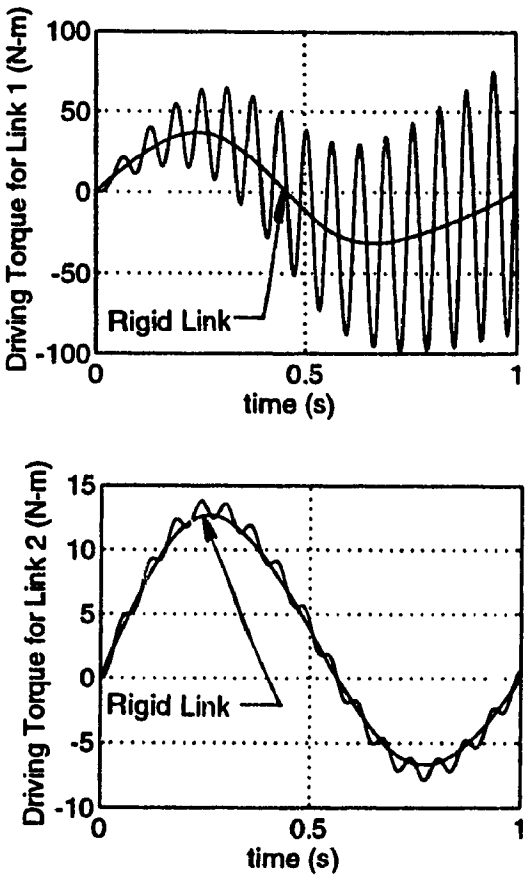

Figure A4.1. Driving Torques for Cycloidal Trajectory, E=7.11×10^{10} N/m^2.

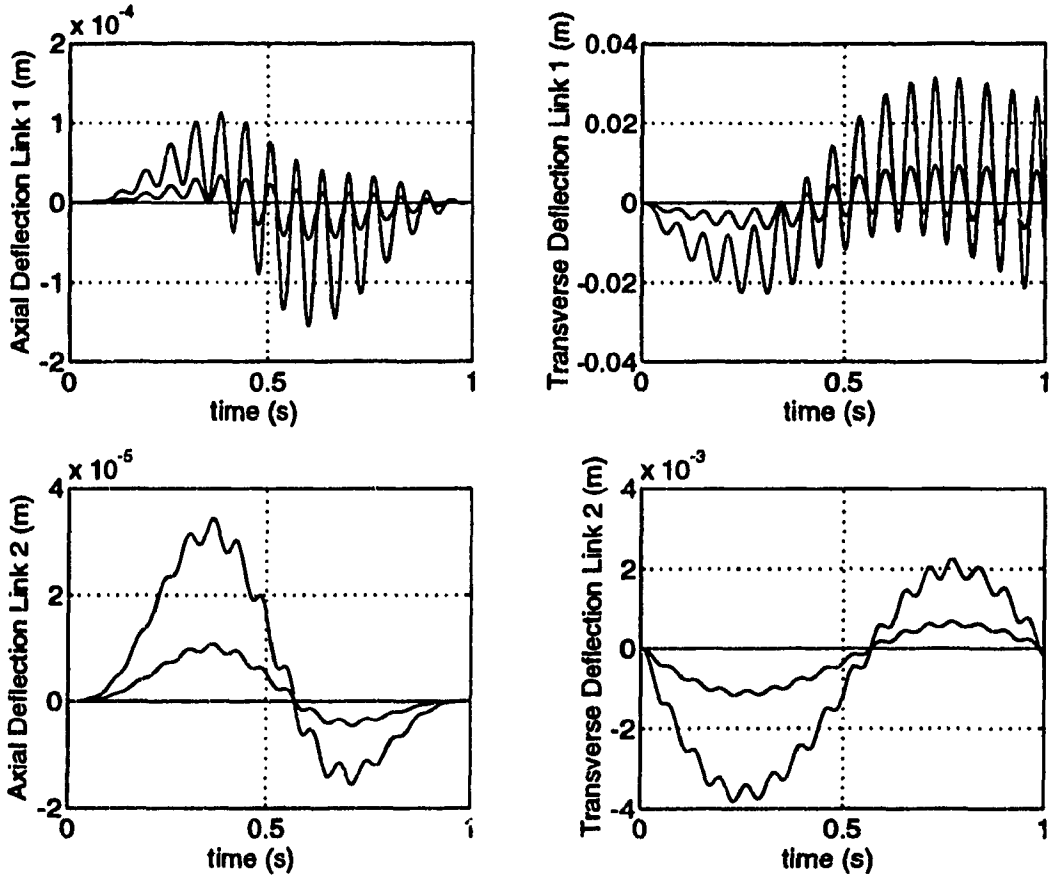

Figure A4.2. Axial and Transverse Deflections for Cycloidal Trajectory with $E = 7.11 \times 10^{10}$ N/m^2.

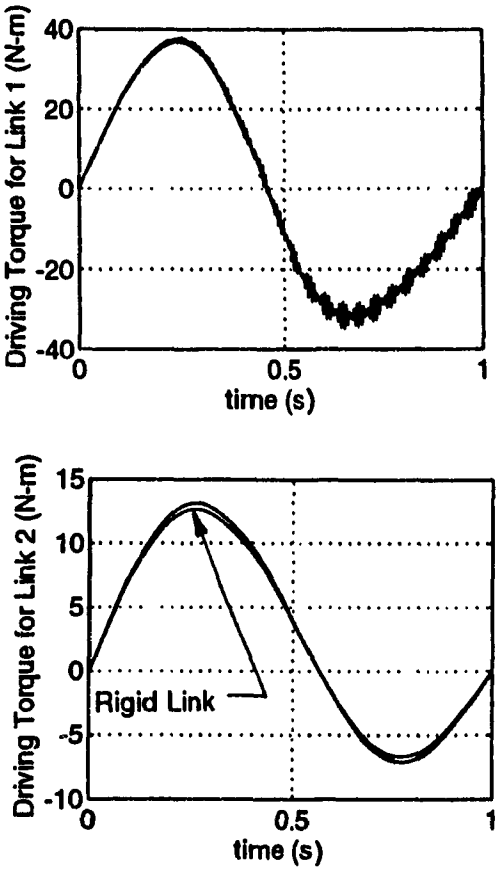

Figure A4.3. Driving Torques for Cycloidal Trajectory, E=7.11×10^{13} N/m^2.

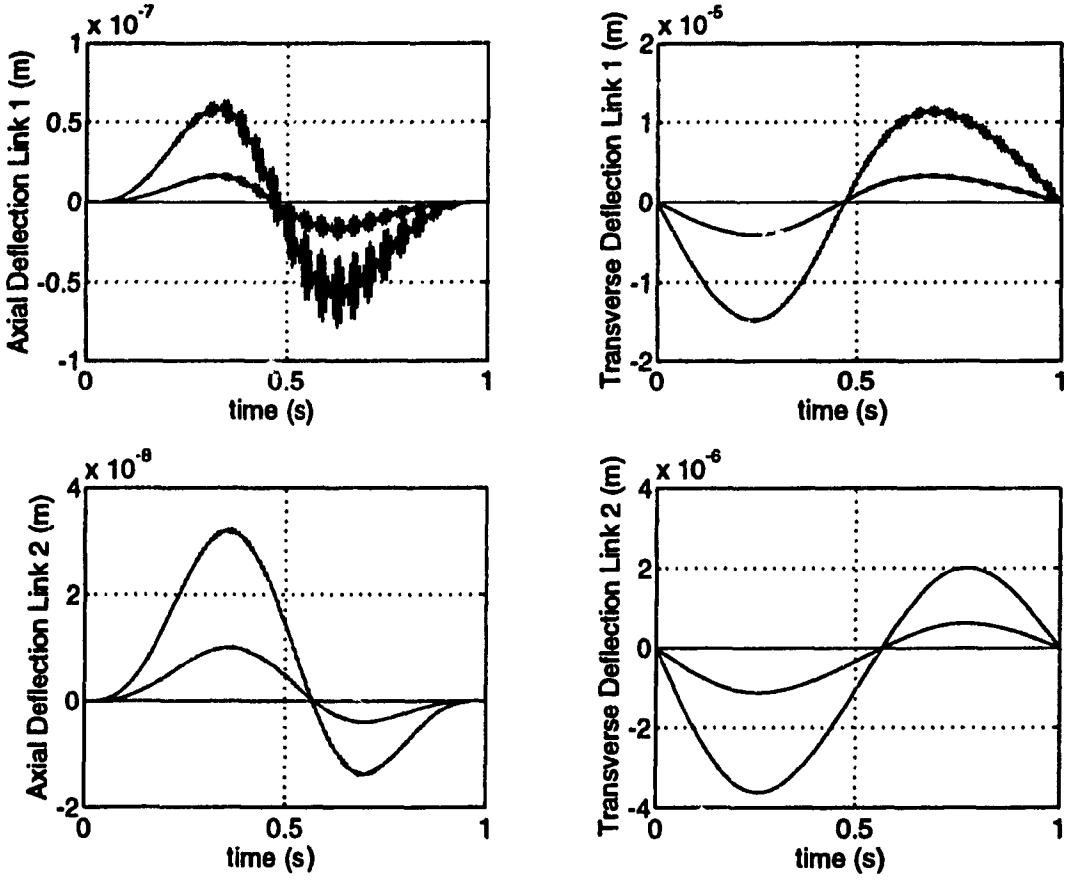

Figure A4.4. Axial and Transverse Deflections for Cycloidal Trajectory with $E = 7.11 \times 10^{13}$ N/m^2.